A Unified Description of the Particle Production in Heavy-ion Collision

Rohit Gupta

A thesis submitted for the partial fulfilment of the degree of Doctor of Philosophy

Department of Physical Sciences

Indian Institute of Science Education and Research Mohali

Sector - 81, SAS Nagar, Mohali 140306, Punjab, India

June 2022

Dedicated to

My Mother

Declaration

The work presented in this thesis has been carried out by me under the guidance of Dr. Satyajit Jena at the Indian Institute of Science Education and Research Mohali. This work has not been submitted in part or in full for a degree, a diploma, or a fellowship to any other university or institute. Whenever contributions of others are involved, every effort is made to indicate this clearly, with due acknowledgement of collaborative research and discussions. This thesis is a bonafide record of original work done by me and all sources listed within have been detailed in the bibliography..

Rohit Gupta

In my capacity as the supervisor of the candidate's thesis work, I certify that the above statements by the candidate are true to the best of my knowledge.

Dr. Satyajit Jena

Acknowledgement

First and foremost, I gratefully acknowledge the continual guidance and support of my adviser, Dr. Satyajit Jena. His dedication to research and pursuit of physics has been an invaluable source of inspiration and encouragement to me. I would also like to thank my PhD monitoring committee members Dr. Kinjalk Lochan and Dr. Anosh Joseph for providing useful guidance and monitoring my PhD work.

I would like to thank my friends who made my half decade of stay at IISER Mohali awesome and memorable. First and foremost a big thanks to my all weather ally Dr. (soon to be) Ranbir Sharma. I would also like to thank my friends Akshi, Nishat, Jasleen, Aman, Soumya, Bharat, Sandeep and EHEP lab members for the wonderful time at IISER Mohali.

Abstract

Search for Quark-Gluon Plasma (QGP), a deconfined state of quarks and gluons, is the primary motivation behind several experimental as well theoretical studies in particle physics. Formation of the QGP state requires extreme condition of temperature and energy density. Such conditions are believed to exist during the birth of our universe. However, those astronomical observable effectively washed out due to the subsequent evolution of the universe, and the only means to study this fundamental state of matter is via the collision of heavy nuclei in the laboratory. Thus, the study of QGP, which enables a detailed and quantitative characterization of the high density, high temperature phase of strongly interacting matter, together with the exploration of new phenomena, are some of the important milestones where we can fully exploit the scientific potential of the front-line experiments at RHIC and LHC.

Some of the questions that are crucial in understanding the nature of QGP includes the study of the nature of phase transition between confined hadronic state and the deconfined QGP state and to determine the location of the critical point in the QCD phase diagram, the point where the first-order phase transition line terminates. In order to quantify the confinement-deconfinement phase transition and to search for the critical point, the QCD phase diagram has been scanned by varying collision energy and studying the thermodynamical properties such as temperature and the baryon chemical potential of the system created during such collision. Extracting the temperature, which is a crucial ingredient of the phase diagram, requires a proper parameterization of transverse momentum (p_{T}) spectra. Although the standard theoretical description of the strong interaction comes from the QCD, however, due to the asymptotic freedom of the QCD coupling constant, it is difficult to apply QCD theory to study the p_{T}-spectra. In this direction, several phenomenological models with varied physics motivation have been developed to study the spectra of final state particles produced in high energy collision.

Although there are several phenomenological models, ranging from statistical thermal models such as Boltzmann-Gibbs statistics $\&$ Tsallis statistics to the hydrodynamical models such as Blast-Wave $\&$ Tsallis blast-wave model, majority of them apply only to the low-$p_{\rm T}$ region. It is important to mention here that particle production in high energy collision can be classified into two separate categories. The low-$p_{\rm T}$ particles are produced by the soft processes, whereas the hard scattering process contributes to the majority of particles in the high-$p_{\rm T}$ region. These models have been used extensively to study the transverse momentum spectra in the low-$p_{\rm T}$ region. For fitting the high-$p_{\rm T}$ region, a well defined, QCD inspired power-law form of the distribution function is used. Since there is no fine line separating these two regions, a unified formalism which can explain both the low- and high-$p_{\rm T}$ region is still an open problem and important to tap into the full potential of the high energy collision experiment measuring the spectra over a broad $p_{\rm T}$ range. In the thesis, we have discussed a unified thermodynamical framework based on the Pearson probability distribution function to study both low- and high-$p_{\rm T}$ region in a consistent manner. Pearson distribution is a generalized probability function, which under limits on its parameters, reduces to other distributions such as Gaussian, Gamma, Beta, Student's t distribution, etc. We have provided the first application of the Pearson formalism in studying the particle production spectra in high energy collision. We have discussed the detailed mathematical formulation of the unified statistical framework. This thesis also discusses the detailed derivation of the thermodynamical consistency and the backward compatibility of this model. The fit results obtained using this formalism on the transverse momentum spectra at different collision energies, centralities and the collision system are provided, along with its application to study other quantities such as the response function etc.

List of Publication

Published:

- Satyajit Jena & **Rohit Gupta**,"A unified formalism to study transverse momentum spectra in heavy-ion collision" Phys.Lett.B 807 (2020) 135551

- **Rohit Gupta**, Aman Singh Katariya & Satyajit Jena, "A unified formalism to study the pseudorapidity spectra in heavy-ion collision" Eur.Phys.J.A 57 (2021) 7, 224, [arXiv:2103.14547 [hep-ph]]

- **Rohit Gupta** and Satyajit Jena, "Model comparison of the transverse momentum spectra of charged hadrons produced in PbPb collision at $\sqrt{s_{NN}} = 5.02$ TeV", Adv. High Energy Phys. 2022 (2022) 5482034, [arXiv:2103.13104 [hep-ph]]

Under Review:

- **Rohit Gupta**, Anjaly Menon and Satyajit Jena, "The theoretical description of the transverse momentum spectra: a unified model", [arXiv:2012.08124 [hep-ph]]

- **Rohit Gupta**, Shubhangi Jain and Satyajit Jena, "A unified statistical approach to explain the transverse momentum spectra in hadron-hadron collision", [arXiv:2103.11185 [hep-ph]]

- Shubhangi Jain, **Rohit Gupta** and Satyajit Jena, "Study of isothermal compressibility and speed of sound in matter formed in heavy-ion collision using unified formalism", [arxiv:2103.15117 [hep-ph]]

Contents

List of Figures

List of Tables

Chapter 1

Introduction

Strong nuclear force, as the name suggests, is the strongest among the four fundamental forces and acts at the small scale ($\sim$ few fm) inside the nucleus. It binds quarks inside a nucleon and the corresponding interaction is carried by the exchange particles called the gluon. A set of quarks bound together by strong interaction makes up a nucleon (*hadrons* in general).

The first theoretical description of partons (particle inside proton or other quark-containing particle), *quark model*, was proposed in 1964 by Murray Gell-Mann [36] and George Zweig [37, 38]. This model classifies quarks into six flavors (up, down, charm, strange, top, bottom). A quantum number called "color" (red, green & blue; these are not to be treated as real colors) was introduced by Oscar Greenberg to explain the coexistence of quarks inside a hadron without violating the Pauli exclusion principle. The quarks of different color combine to make the hadron "colorless". Although there was ample theoretical understanding, but the substructure of nucleons and the identity of quark was first proved experimentally in the deep inelastic scattering (DIS) experiment at Stanford Linear Accelerator (SLAC) [39].

As per the standard model of particle physics, leptons, quarks, gauge and Higgs bosons are the only fundamental particle (particle with no known substructure) that exist in nature. Leptons include electron (e), muon (μ) and tau (τ) and their corresponding neutrinos. Gauge bosons (gluon, photon and W & Z) mediate the fundamental interactions. And quarks mix up to form the composite hadrons that are further divided into two separate categories: baryons and mesons. Baryons are made up of three quarks of different color to make them colorless, whereas mesons are made up of a quark-antiquark pair.

Interaction of quarks are governed by the potential of the form:

$$V(r) = -\frac{4}{3}\frac{\alpha_s}{r} + kr \tag{1.1}$$

Here α_s is the coupling strength, k is the string tension and $4/3$ is the color factor. The first term in the above potential represents coulomb type attraction, whereas the second term corresponds to string tension, which tends to confine quarks. The first term will dominate at a short distance and when we increase the distance, the second term leads to an increase in potential, making it impossible to pull two quarks apart from each other's influence. Hence, the second term is known as the confinement term, making sure quarks are confined and not free to move around.

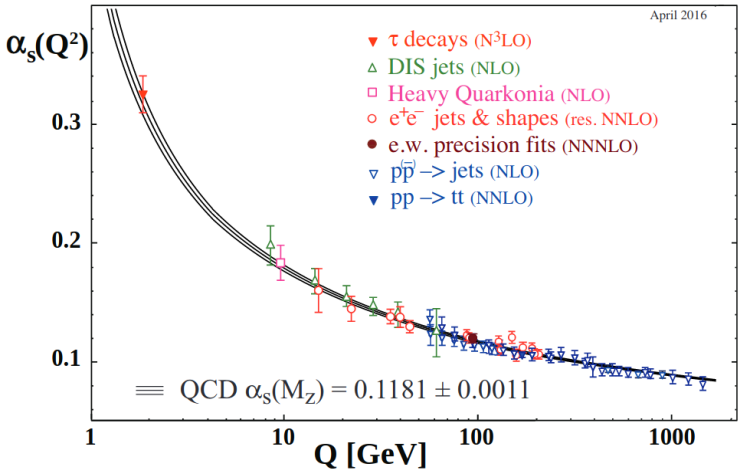

Figure 1.1: Variation of running coupling strength versus energy scale. (Image taken from the Ref. [1]).

The Quantum Chromodynamics (QCD) provides the detailed theoretical description of the strong interaction between quarks and gluons. The strength of interaction between partons is governed by the strong interaction coupling constant (α_s) and the QCD calculation suggests that with an increase in the momentum transfer scale (Q), the α_s decreases as depicted in Fig. 1.1. The nature of strong interaction and the requirement of color neutrality prohibits isolation of quarks and gluons in physical vacuum (laboratories) [40], however, due to the running nature of coupling constant, partons may behave asymptotically free at extremely high momentum transfer scale. QCD predicts that nuclear matter undergoes a phase transition at a temperature of about 10^{12} K, density 10^{15} gcm^{-3} [41, 42] and an energy density of about 0.7 $GeVfm^{-3}$ [43]. At such critical conditions, bound states of

nuclear matter lose their identity and dissolve into a deconfined and chiral symmetric state of quarks and gluons [44]. In 1973, G. F. Chapline, M.H. Johnson, E. Teller & M.S. Weiss, discussed the possibility of creating a very hot and dense nuclear matter in the laboratory by colliding highly energetic heavy-ions [45]. Also, in 1975, J. C. Collins and M. J. Perry discussed the possibility of existence of such extreme condition of temperature and energy density in the core of neutron star, exploding black holes and during very early stages of universe expansion after the big-bang [46]. So, QCD predictions on asymptotic freedom of quarks and gluons [47, 48] can be tested by probing nucleons at very high four-momentum transfer squared Q^2 (as $Q^2 \rightarrow \infty$, the coupling constant $\alpha_s(Q^2) \rightarrow 0$) [49, 50]. Later, in the early 21^{st} century heavy-ion collision experiments managed to provide the experimental evidence for the creation of this new state of deconfined quark and gluon known as the Quark-Gluon Plasma (QGP). Historically, it is said that the QGP state is *"thermally equilibrated state of matter in which quarks and gluons are deconfined from hadrons, so that color degree of freedom become manifest over nuclear volume rather than a nucleonic volume"*[1].

Understanding the evolution and dynamics of systems involving strong interaction makes the study of relativistic heavy-ion collisions an interdisciplinary and emerging field of research in high energy physics. The matter produced in relativistic heavy-ion collision enables the physicists to explore the phase diagram of QCD, the quantum theory which governs the strong interactions. In a broader sense, it extracts information about the properties and states of matter that exist at very high temperatures and high densities produced by colliding highly accelerated particles. The prediction of standard model can also be examined by exploring heavy-ion collisions.

A wide variety of ions such as Niobium ($^{93}_{41}Nb$), Gold ($^{197}_{79}Au$), Sulphur ($^{32}_{16}S$), Lead ($^{208}_{82}Pb$) and Xenon ($^{129}_{54}Xe$) has been accelerated in different experiments such as Super Proton Synchrotron (SPS) [52], Relativistic Heavy Ion Collider (RHIC) [53], Large Hadron Collider (LHC) [54]. The basic criteria that needs to be followed in the selection of a nucleus are:

- A sufficiently high nucleon density is required for QGP formation and that is why we go for heavy ions.
- A spherical nucleus is required to simplify the collision geometry (However, there is

[1]This definition is taken as it is from Ref. [51]

also a growing interest in the study using nonspherical prolate Uranium nuclei as it can provide additional information about the dynamics of the system [55, 56, 57, 58]).

- Nucleus should be stable so that it will not decay during the acceleration process.

Gold and lead are the most extensively used nuclei in heavy-ion collision experiments. RHIC experiment used $^{197}_{79}Au$ because it is the only stable isotope of gold. With advancements in technology, the European Organization for Nuclear Research (CERN) manages to accelerate heavier ions hence chooses $^{208}_{82}Pb$, which is the heaviest stable spherical nuclei known so far. Although Bismuth ($^{209}_{83}Bi$) is also stable, it has a non-zero quadrupole moment and hence not spherical.

As briefly mentioned above, QCD provides the theoretical description of the strong partonic interaction, in the next section, we will discuss the formalism and the prediction of this quantum theory of strong interaction.

1.1 Quantum Chromodynamics

The underlying quantum theory, which describes the interaction between quarks and gluons in a strongly interacting matter, is known as QCD.

Lagrangian of QCD is given as

$$\mathcal{L} = \overline{q}(i\gamma^{\mu}\partial_{\mu} - m)q - g'(\overline{q}\gamma^{\mu}T_a q)G^a_{\mu} - \frac{1}{4}G^a_{\mu\nu}G^{\mu\nu}_a \tag{1.2}$$

with

$$G^a_{\mu\nu} = \partial_{\mu}G^a_{\nu} - \partial_{\nu}G^a_{\mu} - g f_{abc}G^b_{\mu}G^c_{\nu} \tag{1.3}$$

where G^a_{μ} are gluon field, $q, \overline{q}$ are quark and antiquark fields, g' is coupling strength, T_a are generators, m is quark mass and γ^{μ} are gamma matrices. The coupling strength g' determines the strength of interaction between constituent quark matter in the system.

One loop running β function for QCD is given as

$$\mu' \frac{dg'}{d\mu'} = -bg'^3 \Rightarrow g' = \frac{g'_0}{\sqrt{1 + 2bg'_0 ln(\mu'/\mu'_0)}} \tag{1.4}$$

where $b = \frac{11 - \frac{2n_f}{3}}{16\pi^2}$. Here n_F is number of quark flavors, μ' is the energy, μ'_0 is reference energy scale and g'_0 is value of g' at that reference energy scale. From Eq. (1.4) we observe

that the coupling strength decreases with increasing energy scale. The Fig. 1.1 depicts the variation of strong coupling constant with the momentum transfer scale.

So the Eq. (1.4) and corresponding figure 1.1 tells us that if we keep on increasing energy scale, we reach a certain threshold value after which quark and gluons appear to be asymptotically free from their nucleonic volume and form a state called the QGP state. This decline in coupling strength with energy is popularly known as the asymptotic freedom.

QCD is an elegant approach to study the quark interactions. In order to study the evolution dynamics of such a strongly interacting system, we apply perturbation theory which involves applying small perturbation and see how the system behaves to this change. However, the increase in the QCD coupling strength in low energy regime means that the perturbation theory is not a viable option to study the dynamics of partons interaction. Several solutions to this problem is suggested and, in this section, we will discuss the MIT Bag model and the Lattice QCD model developed to study the quark interactions.

1.1.1 MIT Bag Model

To understand the laws of motion of quarks confined inside a hadron, bag model was proposed for the first time in 1967 by P. N. Bogoliubov [59]. This model assumes a bag of fixed, infinite, square-well, scalar potentials [60] and quarks are completely confined within this bag. This model lacked a stabilizing pressure which was later included in the MIT bag model. The MIT bag model considers a bag of finite dimension where quarks are confined in it (quarks are assumed to be massless inside the bag). This model also assumes that the quarks are infinitely massive outside the bag. Confinement is the result of the balance between the bag pressure B, which is directed inwards and the outward pressure caused by the quarks field [61].

In the framework of the MIT bag model, for a system of N quarks confined in a bag of radius R, the energy is given as [62]:

$$E = \frac{2.04N}{R} + \frac{4\pi}{3}R^3B \tag{1.5}$$

At the equilibrium radius, which is determined by the solution of $dE/dR = 0$, the bag

pressure constant 'B' is given as:

$$B^{1/4} = \left(\frac{2.04N}{4\pi}\right)^{\frac{1}{4}} \frac{1}{R} \tag{1.6}$$

Considering a three quarks system and a confinement radius of 0.8 fm, the value of bag constant is:

$$B^{1/4} = 206\ MeV \tag{1.7}$$

Different groups have calculated the value of bag constant and the values vary significantly with the Los Alamos National Laboratory (LANL) group reporting a value of 145 MeV [63] whereas a higher value of 235 MeV is reported by the group at CERN [64].

This model also describes the formation of a deconfined state of quarks. This state is achieved when the inward bag pressure is not sufficient enough to hold the outward pressure exerted by quarks. This large pressure of quark can occur at very high temperature or very high number density. For example, as calculated in Ref. [62], at $T = 0$ transition from hadronic matter to QGP occurs at a critical baryon number density of $0.72/fm^3$, whereas, this transition occurs at a critical temperature of 144 MeV for the case of no net baryon number.

1.1.2 Lattice QCD

The growth of the QCD coupling constant in the infrared (low energy) regime limits the applicability of perturbative QCD theories only to high energies. This leads to serious problems in developing the theoretical description of QCD matter produced during high energy collision.

The solution to this problem was proposed in terms of a Lattice gauge theory by Kenneth Wilson [40] in 1974. His proposal was to discretize the Euclidean space-time into lattices with lattice spacing a. This discretization of space-time reduces the degree of freedom of fields from infinity to a finite value which can be controlled. However, the finite lattice dimension breaks the Lorentz invariance, which can be restored in the continuum $(a \to 0)$ limit. A simple two-dimensional representation of lattice is shown in the Fig. 1.2. Where the *site* represent the lattice points and the shortest distance between two adjacent sites are the *link*. Lattice QCD calculations are based on the path integral approach and one can calculate the partition function in this framework. Following the standard thermodynamics

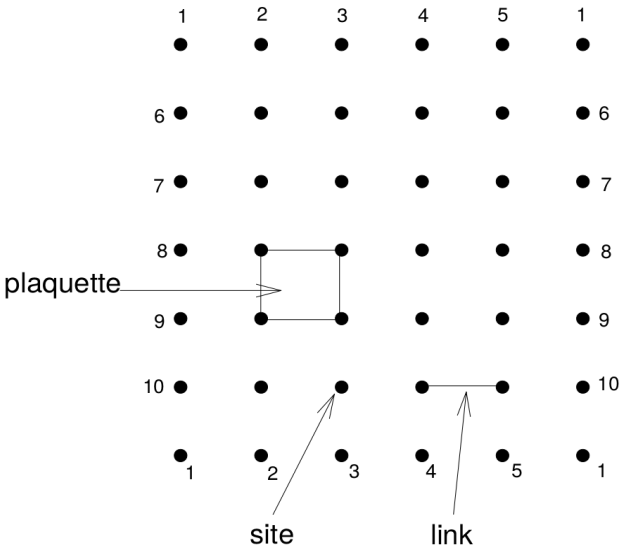

Figure 1.2: A sample lattice in two dimension. (Figure from Ref. [2])

relations, we can extract different thermodynamical variables using the partition function.

The importance of the discretization of space-time is that it limits the ultraviolet divergence in theory by utilizing lattice spacing a as an ultraviolet regulator. The continuum theory can be recovered by applying the limit of vanishing lattice spacing.

The presence of large number of links on the lattice makes Lattice QCD calculation extremely computer-intensive. Limitation in the availability of computational resources constrains the usage of Lattice QCD by restricting the minimum value that can be taken for spacing a.

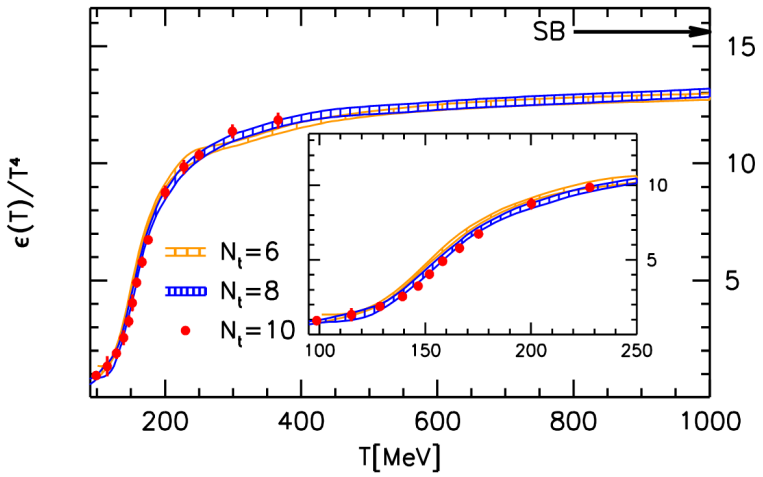

Figure 1.3: Variation energy density normalized with T^4 as a function of temperature from lattice QCD calculation for $6, 8$ and 10 lattices. (Figure from Ref. [3])

Figures above depicts the variation of normalized energy density (Fig. 1.3), entropy den-

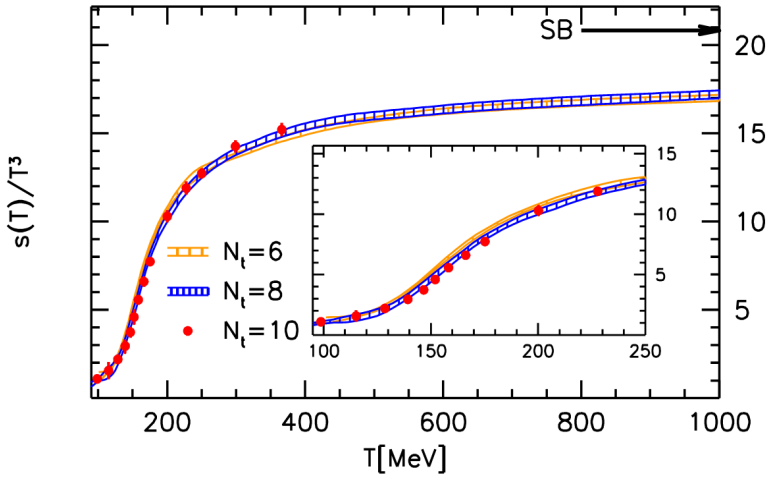

Figure 1.4: Variation entropy density normalized with T^3 as a function of temperature from lattice QCD calculation for $6, 8$ and 10 lattices. (Figure from Ref. [3])

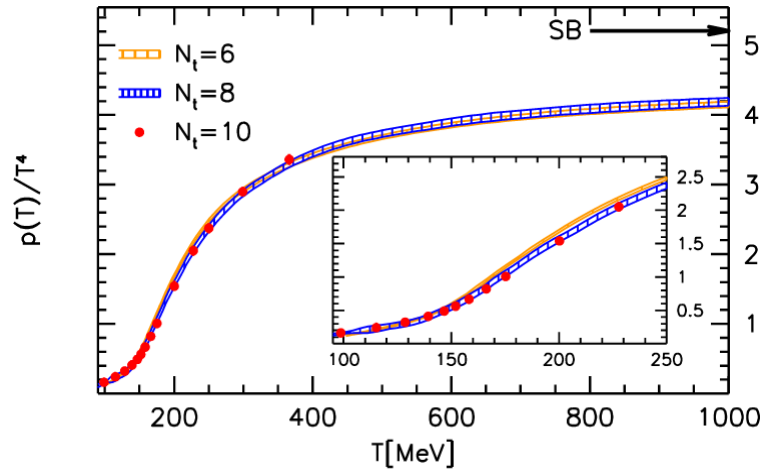

Figure 1.5: Variation pressure normalized with T^4 as a function of temperature from lattice QCD calculation for $6, 8$ and 10 lattices. (Figure from Ref. [4])

sity (Fig. 1.4) and pressure (Fig. 1.5) with temperature based on the Wuppertal-Budapest simulations [3, 4]. Here we observe a steep rise in ϵ/T^4, p/T^4 and s/T^3 in narrow temperature range after which it saturates at higher temperature. Temperature dependence of these thermodynamic variables indicate a rapid change in degree of freedom in temperature range of $150 - 200$ MeV.

Although Lattice QCD become quite successful in the non-perturbative calculation, there are certain bottlenecks that limit its application in understanding dynamic properties of deconfined QCD matter. There are two broad categories of the property of QGP, namely the static and dynamic (or real-time) properties [65]. The static includes a set of properties that can be directly deduced using the Euclidean formulation of finite temperature gauge

theory. Lattice QCD plays a crucial role in studying the static properties of QGP in a strongly coupled, non-perturbative regime. However, the problem arises in studying the dynamic properties because they are formulated in Minkowski space, whereas Lattice QCD is inherently Euclidean. Hence, it is a challenging task to utilize Lattice QCD to study particle production in the low energy regime.

To overcome this constraint in developing theoretical formalism to study the transverse momentum spectra in the heavy-ion collision, we resort to phenomenological models to study the low-p_{T} part of the spectra, which corresponds to the particle produced in soft processes. On the other hand, we use a well defined QCD based power-law form of distribution function to study the high-p_{T} regime where hard QCD processes dominate particle production [66].

Both the MIT bag model and the Lattice QCD formalism point toward the formation of a deconfined state of quark and gluons where the partons are free to move over a nuclear volume rather than being confined into a nucleonic volume. So far, we have discussed the theoretical understanding of the QGP and the quark interaction. In the next section, we will discuss the QGP state and some of the experimental observables that point toward the formation of QGP in heavy-ion collider experiments.

1.2 Quark Gluon Plasma

The QGP is a transient state of QCD matter where quarks and gluons are no longer bound into hadrons [67]. Such a state of matter is expected to exist in the primordial universe, a few microseconds after the Big Bang, and may still exist today in the cores of neutron stars. Thus, the importance of the QGP study is two-fold: extracting the information about the early universe and revealing the nature of various phases of QCD matter. The collision experiments performed to study particle production involve proton-proton (pp), proton-nucleus (pA) and nucleus-nucleus (AA) collisions [68, 69, 70]. The pp collision provides baseline data in the nuclear collision study. Meanwhile, pA collision aids in understanding the transition from pp to AA collisions. In particular, AA collision possesses high particle multiplicity and serves as an important tool in understanding QCD matter and its phases [71]. It is evident from the experiments conducted at the RHIC [72, 73, 74, 75] and LHC [76, 77, 78] that QGP is formed during heavy-ion collision at relativistic energies and be-

haves as quasi-free particles. The experiments conducted for AA collisions have indicated that QGP behaves like a hot and strongly interacting matter and its small shear viscosity makes it a nearly perfect fluid. Let's look into various experimental signatures that are widely used to explore the properties of QGP formed in heavy-ion collision.

1.3 High Energy Collision Experiments

The heavy-ion collision experiments at projectile beam energies greater than 10 GeV per nucleon have been pioneered initially in mid 80's in Alternating Gradient Synchrotron (AGS) at Brookhaven National Laboratory (BNL) and in SPS at CERN [79]. The major breakthrough in heavy-ion collision experiments took place in 2000 when the first magnificent machine in RHIC was set into operation at BNL, New York. Later, the advent of technology upgraded the collision energy, ion beams and detector fields and made it possible to accelerate particles from a few GeV to TeV energies in LHC at CERN. RHIC and LHC are the two largest inoperation heavy-ion colliders. RHIC started its mission in 2000 and is the only collider that collides spin-polarized proton beams. RHIC has four detectors PHOBOS, BRAHMS, STAR and PHENIX. PHOBOS and BRAHMS terminated their operation in 2005-2006. PHENIX is under upgradation from 2016 for its new state-of-art sPHENIX.

LHC at CERN also hosts four major experiments, namely A Toroidal LHC ApparatuS (ATLAS), Compact Muon Solenoid (CMS), A Large Ion Collider Experiment (ALICE) and Large Hadron Collider beauty (LHCb). ALICE is an experimental setup dedicated to study the heavy-ion collision. A good performance at high multiplicities makes ALICE detector system a suitable choice for exploring the high multiplicity pp and AA collision events. Further, excellent particle identification capabilities make ALICE detector suitable for studying the different conserved quantities such as strangeness, baryon number and charge which has a direct connection to thermal system and can shed some light on the phase transition.

The heavy-ion collision at ultra-relativistic speed in the experiment can deposit a large amount of energy in a tiny volume providing enough energy density for the formation of QGP state. The extremely small time scale of QGP formation ($\sim 10^{-22}s$) and limited detector capabilities makes it impossible to perform direct observation and confirm the

formation of this state in heavy-ion collision. However, there are some indirect signatures that suggest the presence of a strongly interacting medium.

1.4 QGP Observables

The formation of QGP can be manifested through various observables - global observables, jet quenching, photon and dilepton production, J/Ψ suppression, strangeness enhancement, antibaryon production, and strong collective flow. Initially, there was no unique signal that can endorse QGP formation. Jet quenching, strangeness enhancement, and J/Ψ suppression were proposed as QGP signatures. Later, the commencement of various experiments along this line predicted other signatures like the collective flow and quark number scaling.

1.4.1 Jet Quenching and Nuclear Modification Factor

The energy modification of high-p_{T} partons due to QGP medium is studied in terms of jet suppression in heavy-ion collisions with respect to pp collision where there is no in-medium energy loss. Hard scattering processes occurring in the early stage of collision produce adjoining parton pairs with high transverse momentum. The beam of collimated hadrons produced from the fragmentation of outgoing partons that travel in the direction of initially produced partons is called jets. The recoiled partons dissipate energy and finally fragments into hadrons. Jets are produced in the early stages of collision and interact with the surrounding ultra-dense and hot medium. This interaction will cause broadening and softening of final state jet showers – called jet quenching predicted by Xin-Nian Wang and Mikles Gyulassy [80]. Comparison of jets in AA collision with pp collision can provide signal of possible QGP formation as the pp collision will not have any medium for jet to loose energy. This jet quenching or high-p_{T} suppression is expressed in terms of the nuclear modification factor (R_{AA}). It is a p_{T}-dependent observable and provides us with crucial information about the difference in the system produced in pp and pA or AA collisions. Partons are expected to lose some energy as they pass through the QGP medium. Hence, high-p_{T} particles, which are primarily produced from the jet, provide an essential tool to understand the energy loss by parton as they traverse the medium. This in-medium energy loss of parton leads to the suppression of p_{T}-spectra in the high-p_{T} region compared to the spectra expected by considering heavy-ion collision as an incoherent superposition of pp

collision. This suppression in the production of high-p_{T} particles is quantified using the nuclear modification factor.

Measurement of nuclear modification factor has been carried out by different experiments with varying collision energies. WA98 experiment in SPS at CERN measured the nuclear modification factor for 12.7% most central $PbPb$ collision at $158A$ GeV [81]. Different experiments at RHIC such as BRAHMS, PHOBOS [73], STAR [82] and PHENIX [75] also analyzed the suppression factor for different collision energies accessible at RHIC. With the commissioning of LHC, higher energy collisions are accessible and nuclear modification at these energies are studied by ALICE [16], CMS [27, 28] and ATLAS [5] experiments. Significant suppression in nuclear modification factor at mid-p_{T} range has been observed at

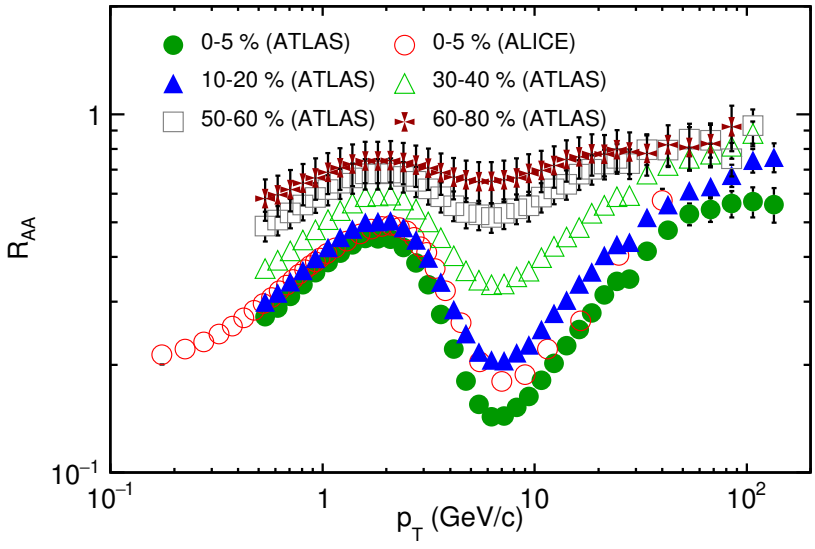

Figure 1.6: Variation of Nuclear modification factor of charged particles with centrality for $PbPb$ collision measured by ATLAS experiment ($|\eta| < 2.0$) [5] at $\sqrt{s_{NN}} = 2.76$ TeV energy along with most central data of $XeXe$ collision at 5.44 TeV from ALICE experiment ($|\eta| < 0.8$) [6].

RHIC ($p_T > 2$ GeV/c) and LHC ($5 \leq p_T \leq 10$ GeV/c) energies reflecting strong medium effect on particle production as shown in Fig. 1.6.

1.4.2 Strangeness Enhancement

The strangeness content of quark matter is cooked up when the fireball is created. Strangeness is among one of the initially proposed signals of formation of the deconfined state of matter [83, 84]. The colliding hadronic matter is made up of “up” and “down” quarks and their quark-antiquark pairs can be easily produced due to their small masses. On the other

side, strange quarks are massive and their quark-antiquark pairs can be created only at high temperature or energy density. This temperature scale is equivalent to the magnitude of temperature required to produce QGP. The detection of strange quarks is sensitive to evolution of QGP [84, 85, 86]. Creation of strange quarks is expected to follow gluon fusion reaction $gg \rightarrow s\bar{s}$ [87]. The strange quark-antiquark pairs formed ultimately reunite with available non-strange quarks to form final state strange hadrons, which are detected through tracks formed by their decay products. This enhancement is studied in terms of strangeness enhancement factor. The experimental data on strangeness enhancement in $AuAu$ collision at $\sqrt{s_{NN}} = 200$ GeV is shown in Fig. 1.7. Different research groups have reported the strangeness enhancement from time to time [88, 89, 90, 91, 7]. The enhancement has also

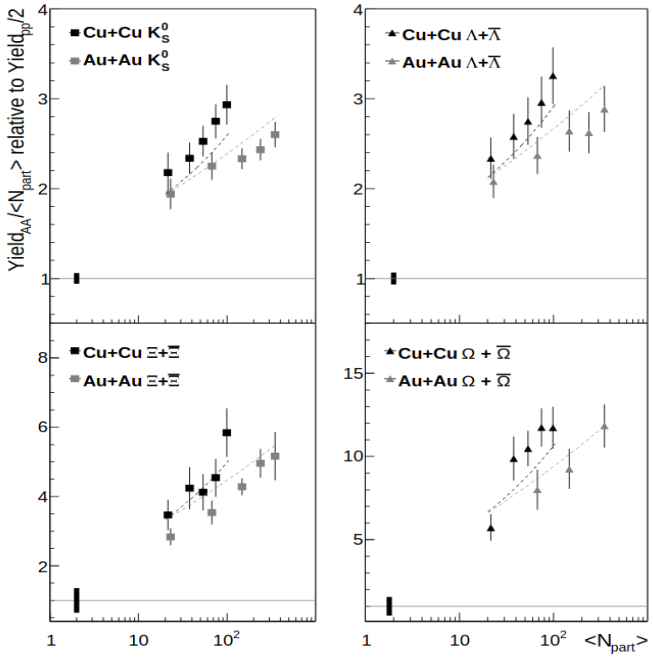

Figure 1.7: The variation of enhancement factor for strange hadrons produced in $CuCu$ and $AuAu$ collision at 200 GeV [7].

been found in hidden strange ϕ meson [92]. However, the strangeness enhancement in AA collision with respect to the pp collision is still debatable on the basis of canonical suppression. It is predicted that strangeness production is limited in case of pp collision to conserve strangeness, which gives rise to canonical suppression [93, 94, 95]. The strangeness yield and yield of photons and dileptons is related to the initial conditions of QGP. But little background in case of strangeness and its source (gluons) make it a better signal to study QGP.

1.4.3 Electromagnetic Probes

Hadrons are the final state product produced from the freeze-out surface whereas photons and dileptons are emitted from the initial state throughout the entire volume. The photons and dileptons do not carry any color charge and undergo only electromagnetic or weak interaction, hence they escape from the strongly interacting medium without undergoing through any interaction in the QGP medium. So they can bring lot of information about the QGP, hence they are categorized as electromagnetic probes. The photons produced in high energy collision can be divided into two different categories, direct photon are produced during the initial collision and through the decay of partons during the early stage of collision, whereas the decay photons constitute the photons produced by the decay of hadrons. There are various types of direct photons, including prompt photons, fragmentation photons, pre-equilibrium photons and thermal photons. The annihilation, Compton process and Bremsstrahlung are important photon production processes. Direct photon can be considered as a QGP diagnostic probe, but large background from hadron decay (mainly) hinders the signal. Many methods have been introduced to abolish background, but it still needs attention. The study of photons can give us information about the temperature of the plasma and the evolution of the system size. The elliptic flow of photons can also shed some light on the momentum anisotropy of initial partons. Dileptons emerging in the collision process from the decay of virtual photons are also a profound signal of quark matter. Photons and dileptons are produced by the annihilation of quark-antiquark and are considered as a primary diagnostic tool [50]. The yield ratio of photons to dileptons is 300, but the background in the case of dileptons is very low compared to photons. Further, dilepton pairs have some other origins and their production pattern is difficult to interpret. A detailed discussion regarding the electromagnetic probes in high energy collision can be found in Ref. [96].

1.4.4 J/ψ Suppression

The most common bound state of charm quark-antiquark ($J/\psi = c\bar{c}$) is observed to be suppressed in $158A$ GeV $PbPb$ collision. This suppression has been linked to the formation of QGP, which hinders the binding of charm quark-antiquark (color screening) or break down their bound state. Charm quarks are formed when colliding nuclei begin to penetrate each

other as colliding nucleons have sufficient energy to produce charm quarks. The existence of a QGP during the evolution process hinders the formation of the charmonium as the distance travelled by J/ψ meson depends on the impact parameter. This effect is predominant in most central collisions and offers an opportunity to determine interaction strength. It was proposed in 1986 by Matsui and Satz [97] that J/ψ suppression w.r.t pp collision is a signature of QGP appearance which was observed in NA50 [98] for the first time and later in other experiments [99, 100, 101]. The Fig. 1.8, shows a clear suppression of the production

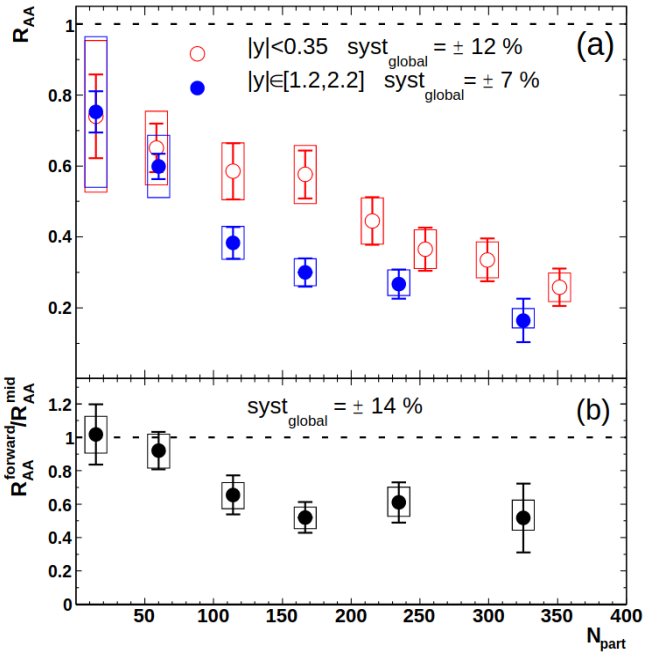

Figure 1.8: Variation of nuclear modification factor with N_{part} for J/ψ produced in $AuAu$ collision at $\sqrt{s_{NN}} = 200$ GeV [8].

of J/ψ as we move from peripheral to the central collision. Such suppression are also observed in pA collision which is popularly known as the Cold Nuclear Matter (CNM) effect. However, as discussed in Ref. [8], the magnitude of suppression in the heavy-ion collision is much large and cannot be accounted for by simply extrapolating the CNM effects of pA collision.

From an experiment point of view, an important step ahead in understanding the phase transition is to scan the QCD phase diagram and look for the critical point. We will discuss it in detail in the next section.

1.5 QCD Phase Diagram

Phase transition is a physical processes in which certain thermodynamical property of a system changes (mostly abruptly) due to change in external parameters such as pressure, temperature etc. Following the Ehrenfest classification, phase transition can be categorized based on the order of the lowest derivative of Gibbs free energy (G) which shows a discontinuity upon the transition. During a first order phase transition, entropy $\{S = -(\partial G/\partial T)_P\}$ and volume $\{V = (\partial G/\partial P)_T\}$ is discontinuous. In a second order phase transition, specific heat $\{c_p = (\partial^2 G/\partial T^2)_P\}$ shows a discontinuity across a transition. Another type of transition where there is a phase change is the "crossover" transition. In crossover transition, the phase change occurs in a smooth manner without involving any discontinuity in the thermodynamic observables.

It is a natural quest to ask whether the QGP formation is accompanied by some phase change and if so, what is the phase diagram of the QGP? To answer this question, experiments have been exploring the QCD phase diagram in order to search for the critical point and to gain more insight into the quark-hadron phase transition.

QCD phase diagram is a plot of temperature (T) as a function of chemical potential (μ) of the system under consideration (in our case, we consider chemical potential to be baryon chemical potential (μ_B)). We can obtain temperature T from p_{T}-spectra and chemical

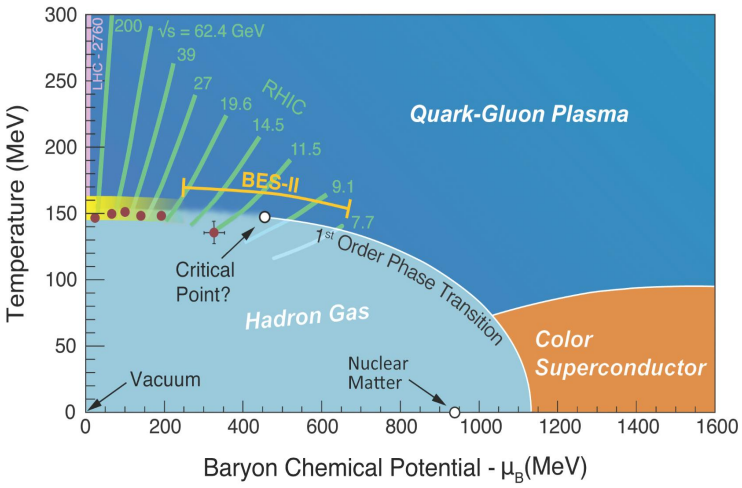

Figure 1.9: QCD phase diagram.

potential μ_B from the ratio of hadrons and using these value, we construct $T - \mu_B$ phase

diagram. In the QCD phase diagram, quark-hadron phase transition at μ_B close to zero is expected to be a simple crossover, whereas it is a first-order phase transition at higher μ_B.

So based on the phase diagram, there are two different ways to explain the QGP. One way is to increase the temperature at very low baryon chemical potential until we cross the transition temperature. Other way is to increase the baryon chemical potential at low temperature. As per Lattice QCD calculations, transition in the direction of increasing temperature is a crossover and the transition point along increasing baryon chemical potential is a first-order phase transition. And the critical point lies at the end of the first-order phase transition.

The study of the QCD phase diagram to search for critical point and phase boundary of the quark-hadron phase transition is one of the major goals of current particle physics experiments across the globe. Beam Energy Scan (BES) program has been started at RHIC to scan the QCD phase diagram by colliding $AuAu$ with varying collision energies starting from 39 GeV to lowest beam energy of 7.7 GeV. These results were complemented by the earlier datasets for $AuAu$ collision at 62.4, 130 & 200 GeV. The main aim of BES is to find the critical point and the phase boundary in QCD phase diagram. As we discussed, any abrupt change in the signatures of QGP with decreasing energy will be a smoking gun signal of the existence of the QCD phase boundary, below which QGP phase cannot exist, indicating a quark-hadron phase transition.

It has been suggested in several manuscripts [102, 103, 104] that there would be an enhancement in fluctuation in multiplicity distribution of net-charge, net-strangeness and net Baryon number near the critical point. Higher moments of the distribution of these conserved quantities are expected to be sensitive at the phase boundary. Product of moments such as $\kappa\sigma^2$ for the net baryon distribution is believed to show a significant deviation from unity near the critical point [105, 106]. Further, skewness (S') of the distribution as a function of energy density can also show a change in sign near the phase boundary [102, 107].

A notable reduction in net-electric charge fluctuation as compared to that in ordinary hadron gas system is also expected in the phase transition from QGP to hadronic phase because the electric charge in the QGP phase is fractional [108, 109, 110]. A detail understanding of the QGP and the study of QCD phase diagram requires the thermodynamical consideration of the QGP state.

1.6 Thermodynamics of the QGP

The study of the QCD phase diagram is important to extract information about the type of phase transition and the critical point. To explain a "phase transition", one needs to know the order parameter of such phase changes. And hence, a detailed study of the phase transition requires the information about the thermodynamical quantities such as the temperature and the chemical potential etc., of the system under consideration. In experiments, we only have the information of kinematic observables such as the transverse momentum, pseudorapidity, etc. Hence, a statistical thermodynamical description of particle production is necessary to extract the thermodynamical parameters of interest from the distribution of final state particles.

Out of several kinematic observable, the energy distribution of final state particles is an important variable in the study of thermodynamic properties of the fireball created during high energy collision. As shown in Eq. (B.5), the energy of a particle is related to its transverse mass ($m_T = \sqrt{p_T^2 + m^2}$) and rapidity as:

$$E = m_T cosh(y) \tag{1.8}$$

Since most of the studies are performed in the mid-rapidity region where $cosh(y) \sim 1$ and hence $E \sim m_T$. This makes the transverse momentum spectra of final state particles an important observable and the proper parameterization of its distribution an important challenge that needs to be addressed. The next section includes a detailed discussion about the transverse momentum spectra.

1.7 Transverse Momentum Spectra

The p_{T}-spectra is an important variable for studying the QCD phase diagram. It plays a pivotal role in understanding the particle production mechanism and evolution of the system. The analysis of the p_{T}-spectra of final state hadrons is crucial in understanding the mechanisms of nuclear collisions and the properties of QGP. The importance of transverse momenta and its properties are listed below:

- The component of momenta transverse to the beam axis has very little contribution from the beam remnants which act as a huge background in the longitudinal direction,

hence the transverse momentum is preferred over the longitudinal momentum.

- As discussed earlier, the transverse momentum spectra also act as a proxy for the energy distribution. So, it can be fitted with a statistical thermal model to extract the thermodynamical quantities such as the temperature of the system.

- The suppression of transverse momentum of the high-p_{T} particles in central heavy-ion collisions compared to pp collisions can signal the presence of a QGP medium. This suppression of p_{T} can be explained through the large energy loss of the high momentum partons moving in a high density medium of color charges.

- The information about the radial flow can be extracted by analyzing the transverse momentum spectra. In central heavy-ion collisions with vanishing impact parameter, radial flow is supposed to play a significant role in the thermodynamic expansion of the produced fireball.

The measurement of the p_{T}-spectra has been carried out in the collision at different energy, collision system and centrality's by several experiments. A brief discussion about different experimental data is provided in the next section.

1.8 Experimental data on transverse momentum spectra

Among the first high energy accelerator for heavy-ion was AGS [111] at BNL, which started in 1960. Experiments like E866, E895, E891, E917, E802, E877 has measured the transverse mass spectra of different hadron at several low energies like $2A$ GeV, $4A$ GeV, $6A$ GeV, $10.8A$ GeV [112, 113, 114, 115, 116, 117, 118, 119, 120, 121]. The measurement of the p_{T}-spectra of ϕ meson with centrality has revealed an interesting feature of heavy-ion collision. The yield of both strange ϕ meson and the non-strange π meson increases as we move toward central collision, however, as discussed in the Ref. [112], the ratio of ϕ to π meson increases as we move toward central collision [112]. This indicates that the enhancement in the production of strange hadrons is stronger than that of non-strange hadrons as we move toward central collision pointing toward the strangeness enhancement which is a signature of QGP formation.

SPS is another high energy accelerator that accelerated heavy ions at several beam energies like 20, 30, 40, 80 and $158A$ GeV etc. The transverse mass ($m_T = \sqrt{m^2 + p_T^2}$) spec-

tra have been measured for different hadrons using NA44, NA49, NA57 and NA61/SHINE experiment [122, 123, 124, 125, 126, 127, 128, 129, 130, 131, 132, 133]. From the

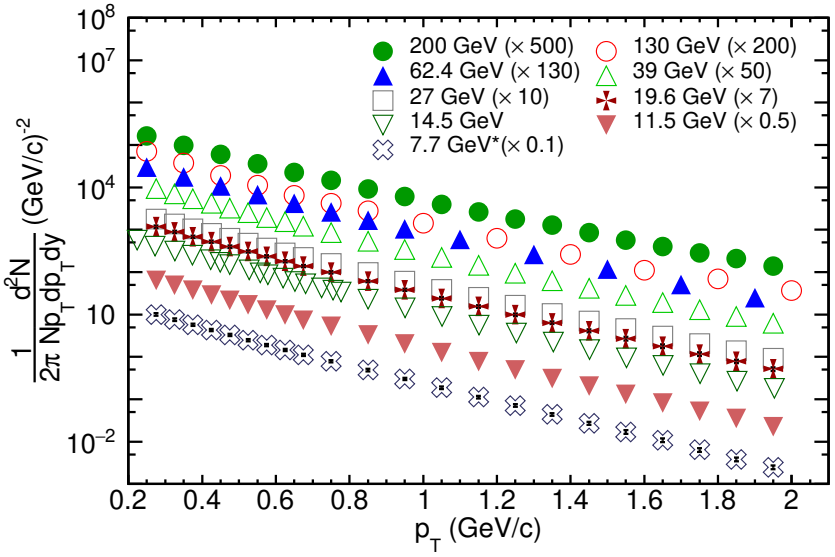

Figure 1.10: Transverse momentum spectra of π^+ produced in most central $AuAu$ collision at different energies in BES program [9, 10, 11, 12, 13]

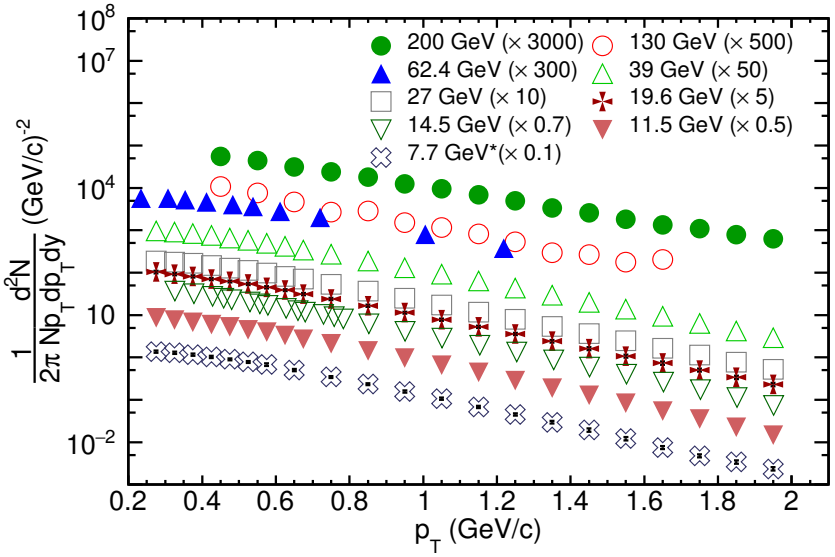

Figure 1.11: Transverse momentum spectra of K^+ produced in most central $AuAu$ collision at different energies in BES program [9, 10, 11, 12, 14]

study of the energy dependence of charged hadron spectra, a non-monotonic dependence in the ratio of K^+ to π^+ on energy has been observed with a peak around $40A$ GeV after which the value are nearly constant. This feature is specific to the heavy-ion collision as no such energy dependence was observed in hadron collisions. As discussed in the Ref. [122], this energy dependence can be explained by considering the possibility of the formation

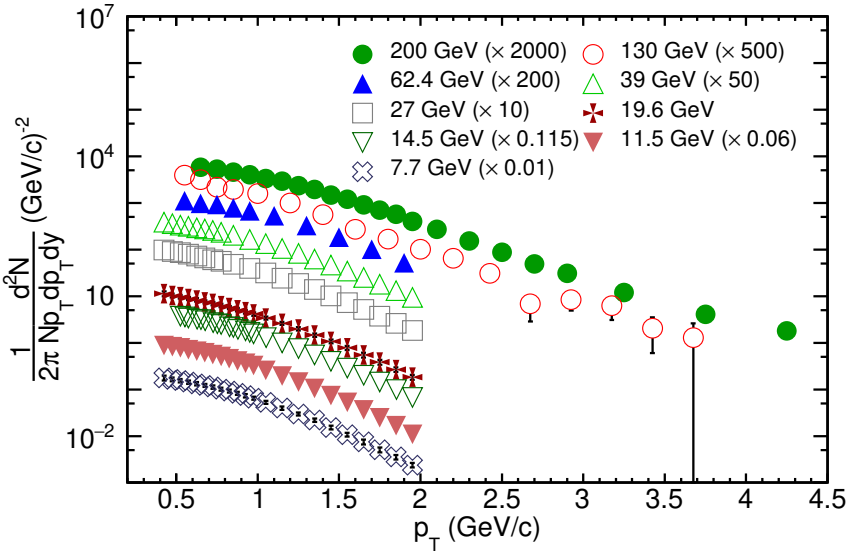

Figure 1.12: Transverse momentum spectra of proton produced in most central $AuAu$ collision at different energies in BES program [9, 10, 11, 12, 13]

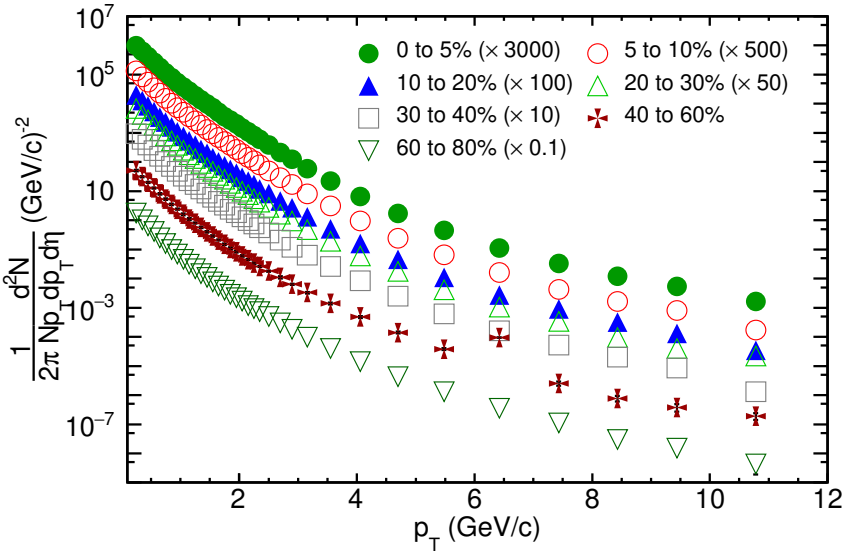

Figure 1.13: Transverse momentum spectra of charged hadrons at different centrality produced in 200 GeV $AuAu$ collision [15]

of a transient deconfined state in the $PbPb$ collision above $40A$ GeV. The measurement of negatively charged hadrons in the collision with different nuclei indicates that their mean transverse momentum at midrapidity does not depend on the mass of colliding nuclei [123]. Other system size dependent studies of hadron spectra also reveal that there is an enhancement in baryon stopping [124, 129] and the collective flow [125] with an increase in system size. The study of the energy dependence of inverse slope parameter extracted from the transverse mass spectra of positive and negative kaons shows a plateau at low SPS energies

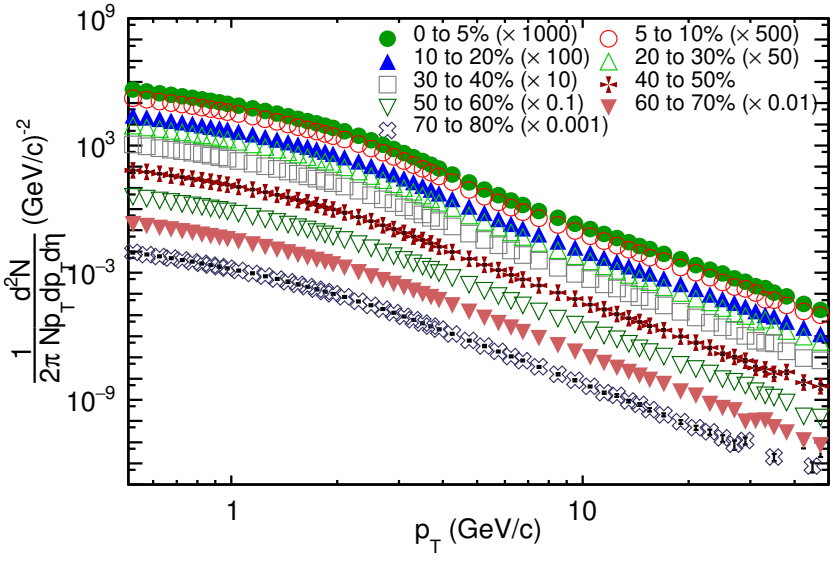

Figure 1.14: Transverse momentum spectra of charged hadrons at different centrality produced in 2.76 TeV $PbPb$ collision [16]

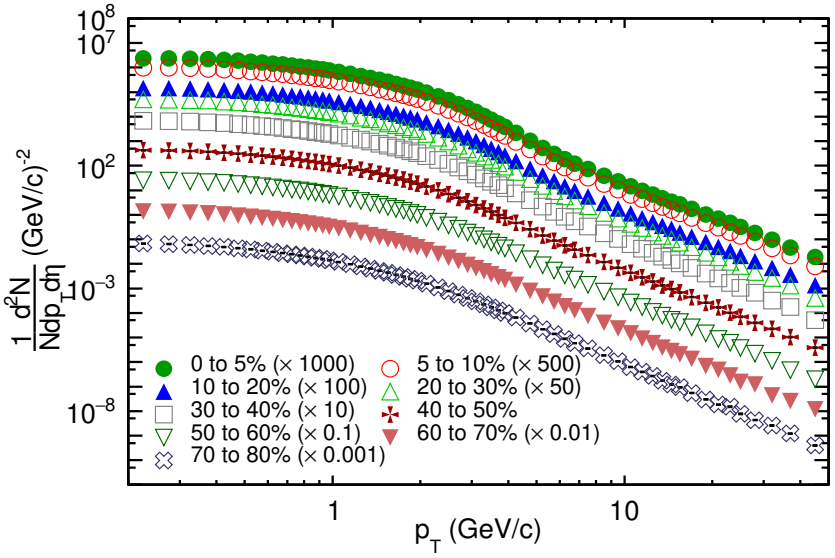

Figure 1.15: Transverse momentum spectra of charged hadrons at different centrality produced in 5.02 TeV $PbPb$ collision [17]

[133]. Further, mean transverse mass ($\langle m_T \rangle$) also shows energy independence at low SPS energies. These two observations are in contrast to the rise observed in lower AGS energies and higher RHIC energies.

The p_{T}-spectra for several identified particles (π, K, p, Λ, χ, Ω, ϕ) have been studied extensively in the experiments at SPS, RHIC and LHC. The fixed target experiments such as NA49 and NA61/SHINE have carried out the measurement of spectra by accelerating the heavy-ion at $20A$, $30A$, $40A$, $80A$, $158A$ etc., in the SPS accelerator at CERN. The

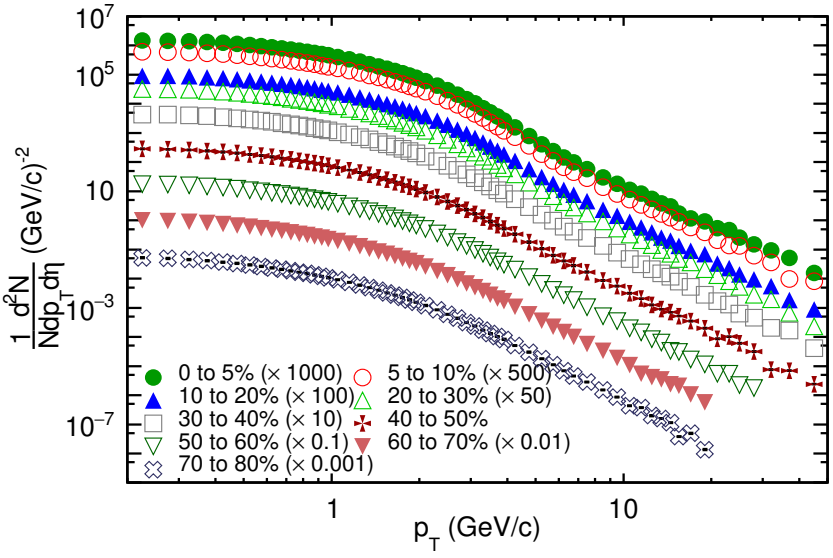

Figure 1.16: Transverse momentum spectra of charged hadrons at different centrality produced in 5.44 TeV $XeXe$ collision [6]

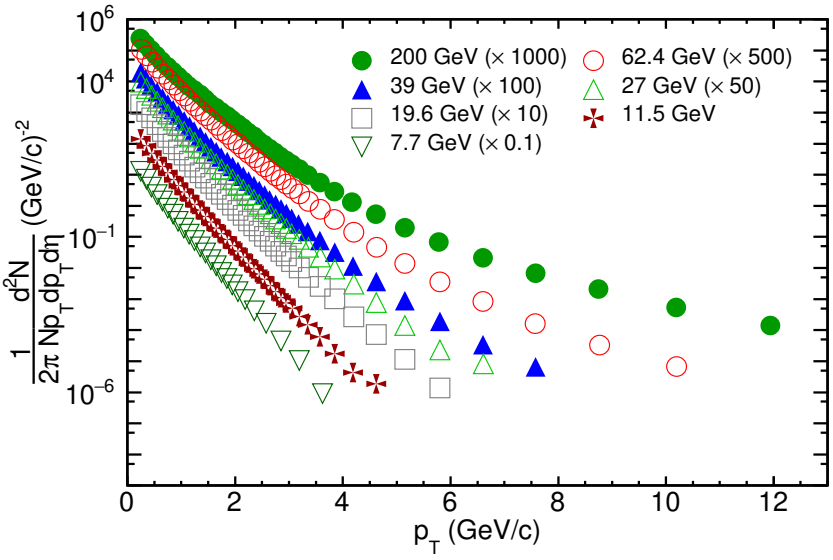

Figure 1.17: Transverse momentum spectra of negative hadrons produced in most central $AuAu$ collision at different energies in BES program [18]

higher center of mass energies has been achieved in the RHIC accelerator. The experiments at RHIC are the collider experiments and the measurement of the spectra has been performed by accelerating different heavy-ion (such as $AuAu$, $CuCu$) at energies ranging from 7.7 GeV upto 200 GeV. The Fig. 1.10, 1.11 & 1.12 show the p_{T}-spectra of π^+ , K^+ and protons respectively at the highest RHIC energy. Highest energies achieved so far in particle accelerator is at LHC in CERN. Four main experiment at CERN, ATLAS, CMS, LHCb and ALICE performed measurement of p_{T}-spectra for different particles in

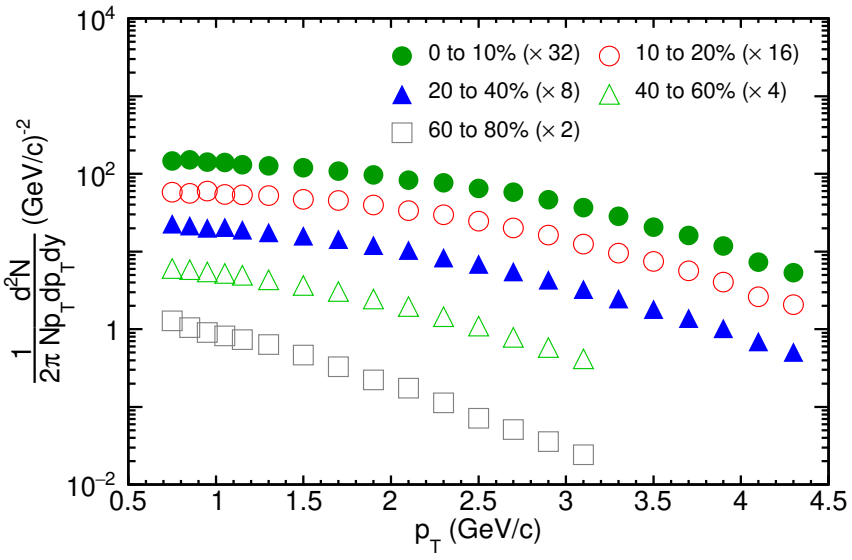

Figure 1.18: Transverse momentum spectra of deutron produced in $PbPb$ collision at different centrality measured by ALICE experiment [19].

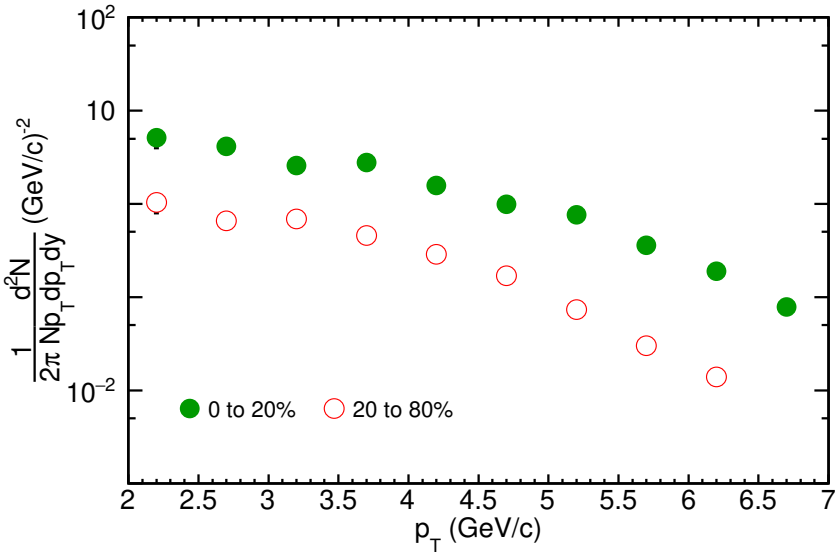

Figure 1.19: Transverse momentum spectra of He^3 produced in $PbPb$ collision at different centrality measured by ALICE experiment [19].

$PbPb$ and $XeXe$ collision at 2.76, 5.02 & 5.44 TeV energies. Apart from the identified particle spectra, experiments have also measured the inclusive charged hadron spectra. The Fig. 1.13, 1.14 & 1.15 show the transverse momentum spectra of charged hadrons at different centrality classes produced in 200 GeV $AuAu$ collision, 2.76 TeV $PbPb$ collision and 5.02 TeV $PbPb$ collisions respectively. The Fig. 1.16 presents the p_{T}-spectra of charged hadrons produced in 5.44 TeV $XeXe$ collision whereas the Fig. 1.17 shows spectra of negative hadron produced in $AuAu$ collision at various energies of the BES program. ALICE

experiment also analyzed deutron and He nuclei and anti-nuclei production in $PbPb$ collision at 2.76 TeV [19]. The transverse momentum spectra of deuterons and He^3 produced in $PbPb$ collision at different centrality measured by ALICE experiment is shown in Fig. 1.18 and Fig. 1.19 respectively. In the study of p_{T}-spectra of nuclei, a decline in yield by a factor of 307 ± 76 has been observed for each additional nucleon.

The Fig. 1.20 shows variation of mean transverse momentum $\langle p_T \rangle$ with mass of differ-

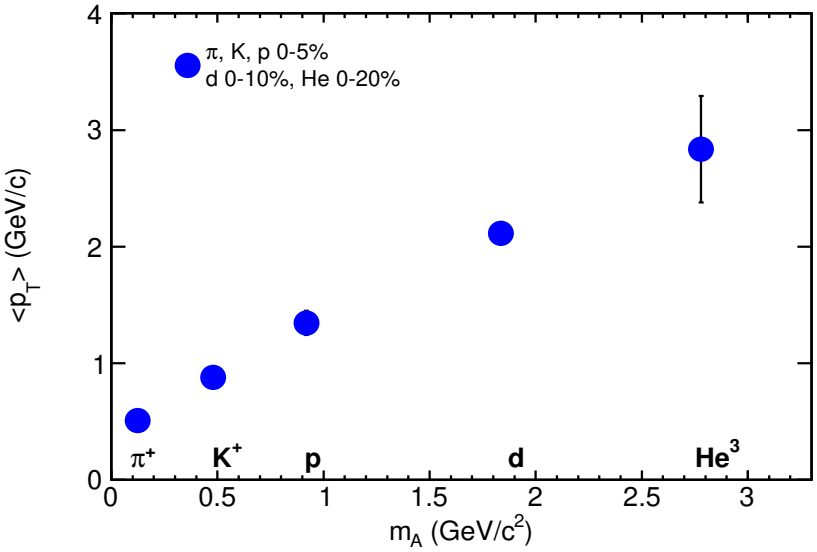

Figure 1.20: Dependence of mean transverse momentum $\langle p_T \rangle$ versus particle mass at different centrality in $PbPb$ collision measured by ALICE experiment [19].

ent particle species. It can be inferred from Fig. 1.20 that mean transverse momentum increases with the increase in particle mass. This observation is in line with the expectation considering the particles are emitted from a radially expanding source [19].

In phase I of the BES program, $AuAu$ collision has been performed for 39, 27, 19.6, 11.5 and 7.7 GeV beam energy. These energies and other collision results at 62.4, 130 and 200 GeV allow us to explore phase diagram over a broad range of baryon chemical potential μ_B. First-order phase transition and critical point are expected to exist within the BES energy range [134]. A systematic study of several observables in the heavy-ion collision has been performed over BES wide energy range in order to understand the evolution dynamics of the system produced in the collision with varying energy and ultimately look for the critical point and phase boundary.

An enhancement in hadronic interactions compared to the partonic ones has been observed with the decrease in energy, particularly below 11.5 GeV [135]. Several other pre-

liminary results helped in understanding the QCD phase diagram. However, statistics are not sufficient in this phase of BES in order to arrive at any conclusion. Hence, BES phase II has been proposed by the collaboration to explore the phase diagram with increased statistics at low energies. BES phase II is expected to become operational by 2020. The $AuAu$ collision will be performed in BES II with $\sqrt{s_{NN}} =$ 19.6, 14.5, 11.5, 9.1 and 7.7 GeV energies.

Apart from the heavy-ion collision, the measurement of transverse momentum spectra has also been performed for smaller collision system such as pp and pA collision. Experiments such as ATLAS [136] and CMS [26, 27, 28] have measured the spectra of charged hadron over a broad p_{T} range upto few hundred GeV/c produced in pp collision at various center of mass energies. The p_{T}-spectra of identified particles produced in pp collision have also been studied in different experiments. For example, in Ref. [137, 138, 139, 140] the PHENIX collaboration have provided the spectra of neutral & charged mesons and the direct photon produced in pp collision at 200 GeV. These results are presented in terms of invariant differential cross-section and it is related to transverse momentum spectra as:

$$E\frac{d^3\sigma}{dp^3} = \sigma_{inel}^{pp} \times \frac{1}{2\pi p_T}\frac{1}{N_{evt}}\frac{d^2N}{dp_T dy} \tag{1.9}$$

The measurement of p_{T}-spectra are one of the first & initial results published by almost all experiments. In this context the p_{T}-spectra for pp collision has been published for higher center-of-mass energy at ALICE [141, 142, 143, 144, 145, 146], CMS [147], LHCb [148, 149, 150] etc. Recently released multiplicity divided data on the transverse momentum spectra of hadrons produced in pp collision at different energies measured by ALICE experiment [151, 29] has opened up a new avenue to search for the presence of QGP like medium in small collision system. The ALICE experiment results on the spectra of strange hadrons discussed in the Ref. [152] show the enhancement in the production of multi-strange particles pointing toward the formation of a QGP like medium in the high multiplicity pp collision.

The measurement of spectra in pA collision play an important role in the study of the CNM effect. As discussed in section 1.4.1, to study the in-medium energy loss due to the presence of strongly interacting QGP, other effects that can mimic these observations need to be identified and removed. Some of the CNM effects include the modification in the parton distribution function in nuclear environment (popularly known as the nuclear

shadowing). Another such effect is the Cronin enhancement [153], where multiple scattering leads to the hardening of transverse momentum spectra in pA collision. To this end, measurement has been carried for dAu collision in RHIC and pPb collision at LHC over different energies and a brief discussion about these can be found in Ref. [154, 155, 156].

Problem Statement

As discussed in the previous sections, p_{T}-spectra is an important observable and plays a significant role in developing our understanding of the QGP medium created during very early stage of heavy-ion collision. For this purpose, a proper parameterization of the p_{T}-spectra is the need of the hour to extract the quantities of interest. Although, QCD is the underlying theory to describe the strongly interacting system, due to the asymptotic freedom and the very nature of QCD coupling it is difficult to apply a perturbative theory in the low-p_{T} region. Hence we rely on the phenomenological models to explain the spectra. Among these models, the most widely used are the statistical thermal and hydrodynamical models.

The transverse momentum distribution contains a broad spectrum of physics information. Several models have been developed to study the physics aspects of it. Further, owning the difference in the underlying process of particle production, the p_{T}-spectra can be divided into two distinct regions. The low-p_{T} regime of the spectra (below $2.2 - 2.5$ GeV/c) can be explained using soft nonperturbative QCD, whereas perturbative QCD comes into play when we study the high-p_{T} region, which corresponds to the hard scattering process. To study the low-p_{T} region of the spectra purely statistical models such as Boltzmann-Gibbs (BG) approach [68], Levy [157, 158], and non-extensive Tsallis statistics [159, 160, 161] have been introduced. Apart, from these the statistical hydrodynamical models such as Boltzmann-Gibbs Blast-wave (BGBW) [162] and Tsallis Blast-Wave (TBW) [162, 163] are also used to study the low-p_{T} part of the spectra. The BGBW and TBW model are the hydrodynamics inspired models taking into consideration the flow effect in high energy collision. To parameterize high-p_{T} part of the spectra, a well defined QCD inspired power-law form of the distribution function is used. Further, the distribution function like q-Weibull [24] also takes into account the effect of hard QCD processes which affect the high-p_{T} part of spectra. The detail of different models is provided in the third chapter of

the thesis.

> *A complete model to explain transverse momentum spectra must include the non-extensivity and collective flow on top of random thermal motion and should also be able to explain the effects in high-p_{T} range arising due to hard pQCD processes. Although there are different models tackling different aspects of the physics, there does not exist a unified model that can explain a broad p_{T} range in a consistent manner. It is important to note that although there are different underlying physics governing perturbative and nonperturbative regimes, there is no fine line separating these two regions of the spectra hence a unified model is necessary to take ultimate benefit from the spectra.*

With an aim of analyzing the broad p_{T} range of the spectra and studying different aspect of it, this thesis presents the development of a unified statistical framework using the Pearson probability distribution.

1.9 Thesis Plan

The primary work discussed in this thesis is related to developing a unified formalism to study the transverse momentum spectra in both low- and high-p_{T} region. An accurate theoretical description of transverse momentum spectra is the need of the hour to tap into the full potential of the ongoing heavy-ion program at RHIC and LHC to study the confinement-deconfinement phase transition. In this direction, we have worked toward developing a unified thermodynamical formalism to study the particles produced in soft processes and hard scattering process.

The thesis is organised in the following ways:

1. The second chapter of the thesis is devoted to the theoretical description of the statistical mechanics and its application in high energy physics. A brief discussion about the application of the statistical thermal models in studying the spectra of particles produced in high energy collision is provided in this chapter.

2. In chapter 3, a detailed discussion of statistical thermal models developed to study the distribution of particles in high energy collision is presented. This chapter also in-

cludes a comparison of different models that are being used to study different aspects of transverse momentum spectra.

3. The unified formalism developed based on Pearson distribution to study the particle production in high energy collision is described in chapter 4. This chapter also includes a detailed thermodynamical consistency check of unified formalism.

4. The results obtained by fitting transverse momentum spectra over different energies, different collision systems (pp, $AuAu$, $PbPb$, $XeXe$) and different particles such as charged hadrons, pions is provided in the chapter 5.

5. Chapter 6 describes the application of unified formalism to study the pseudorapidity distribution. This also includes a brief discussion about different quantities that can be extracted using this framework, such as the speed of sound, isothermal compressibility and flow parameter.

6. The final chapter includes the summary of the work done in the direction of parameterizing transverse momentum spectra and extracting crucial information related to the medium created in high energy collision.

7. In Appendix A and B, the basics of heavy-ion collision, space-time evolution, kinematic observables and the collision geometry is discussed and the problem of low χ^2/NDF is addressed in appendix C.

Chapter 2

Statistical Thermal Model

A proper parameterization of transverse momentum spectra of final state particles produced in high energy collision is important as it can provide us with crucial information about the macroscopic properties of the medium created during early stage of collision. Due to the nature of QCD coupling constant, we cannot apply the perturbative QCD to explain the spectra, hence we rely on the phenomenological models. Several formalism with different physics input have been developed to study various aspects of the physics of $p_{\rm T}$-spectra. Some of the broad categories of the models used to study the spectra are listed below:

- The statistical thermal models include Boltzmann-Gibbs (BG) approach [164], Tsallis statistics [165] and its modified form such as Tsallis-Pareto [166] & Tsallis-factorized statistics [167] etc. These are purely based on the standard statistical mechanics or its extension to the non-extensive regime.

- The statistical hydrodynamical models are the hybrid models incorporating the physics of fluids into the statistical models. This include Blast-Wave model with Boltzmann statistics [162] and the Blast-Wave model with Tsallis statistics [162] etc.

- The above models are primarily used to study low-$p_{\rm T}$ region where the soft-processes dominate the particle production. For high-$p_{\rm T}$ region, where the particle production is dominated by the hard scattering processes, the QCD based power-law form of function, known as the Hagedorn function [66], is used to fit the spectra. In Ref. [168], a relativistic hard scattering model is also introduced to explain the contribution of hard-scattering processes to the spectra. The q-Weibull [24] is another function introduced to study the broader $p_{\rm T}$ range of the spectra.

– There are also several multi-component models such as two-component BG function [169], modified Tsallis/Hagedorn function [25] etc., tackling different p_{T} range with different function.

Statistical thermodynamics is the backbone of many phenomenological models that are used to fit the p_{T}-spectra, so in this chapter, we will discuss the basic statistical mechanics and its application in the high energy physics.

2.1 Basics of Statistical Mechanics

Statistical mechanics is the branch of physics in which we relate the microscopic parameters of the constituent particle to the macroscopic properties of the system. We utilize the laws of statistical mechanics to analyze the macroscopic thermodynamical behaviour of a system of large number of constituent particles. In statistical mechanics, we characterize a macroscopic system in terms of the state variables such as the energy density (ϵ), number density (n') and pressure (P). These state variables can be further utilized to study the dynamics of the system. These quantities can be expressed in term of the distribution function for energy as:

$$n' = \int \frac{d^3p}{(2\pi)^3} \times f(E) \tag{2.1}$$

$$\epsilon = \int \frac{d^3p}{(2\pi)^3} E \times f(E) \tag{2.2}$$

$$P = \int \frac{d^3p}{(2\pi)^3} \frac{p^2}{3E} \times f(E) \tag{2.3}$$

The factor that is common to the above three equation and is of significant interest in statistical mechanics is the distribution function of the energy $(f(E))$ of constituent particles. Distinguishable particles are treated under Maxwell-Boltzmann (MB) statistics; Fermi-Dirac (FD)statistics describe fermions and the Bose-Einstein (BE) statistics explain Bosons. It is important to mention here that both FD and BE statistics reduces to MB statistics at large temperature.

The production of large number particles during high energy collision motivates us to apply statistical thermal models to study the equilibrium dynamics of the system created during high energy collisions. We can utilize the momentum and energy spectra of the final state particles produced in the collision to analyze several thermodynamical parameters

such as energy density, temperature, pressure along with the level of equilibrium achieved. Further, the temperature at which we expect the formation of QGP is of the order 10^{12} K, hence we focus on the classical statistics since at such high temperature both FD and BE statistics reduces to classical MB statistics.

2.1.1 A Brief History of the Application of Statistical Methods in High Energy Physics

The application of statistical methods to study particle production was proposed for the first time in 1948 by Heinz Koppe. The statistical model developed by Koppe includes the particle production, formation and decay of resonances, along with the temporal and the thermal evolution of the interacting system. It also included the approaches to apply MB, FD or BE statistics. Koppe also estimated the equilibrium concentration of different type of produced particles.

The rate of particle (meson) production is given as:

$$\nu(T(t)) = \frac{m_b \sigma}{\pi^2 \hbar^3} T(t)^2 e^{-\frac{m_b c^2}{T(t)}} \tag{2.4}$$

here m_b is the meson mass, $T(t)$ is the temperature at time t and σ is the cross section of excited nuclei (resonances). Integration with respect to time [170] will result in

$$N = a_0(m_1 + m_2) T_0 e^{-\frac{m_b c^2}{T_0}} \tag{2.5}$$

with $m_1(m_2)$ representing mass of projectile (target), $a_0 = 0.031$ and T_0 is the temperature of excited daughter nucleus. Substituting for the values for energy and T_0 gives the estimate for the number of mesons produced per unit time in 380 MeV αA collision to be $\sim 1.7 \times 10^{-4}$ [171, 172].

Two years later, in 1950, Fermi proposed a generalized statistical method for the production of multiple particles in high energy collision. The abstract of his seminal work reads: *"A statistical method for computing high energy collisions of protons with multiple production of particles is discussed. The method consists in assuming that as a result of fairly strong interactions between nucleons and mesons the probabilities of formation of the various possible numbers of particles are determined essentially by the statistical weights*

of the various possibilities."[1]

Fermi model assumes that during high energy collision, energy is localized to a small spatial volume which further decays into a different final state. This was a generalized formulation in the sense that it starts with the basic cross-section formula and includes assumptions about the matrix element of the decay process. Here, different decay modes are assigned to statistical weights. This formalism finds its application in various processes such as pion and strange particle production in nucleon-nucleon and meson-nucleon collision. Although the Fermi model was quite successful in the energy range corresponding to cosmic ray, it breaks at lower energies.

In 1965, Hagedorn provided a systematic thermodynamic description for the strong interaction. He assumed that *"higher and higher resonances of strongly interacting particles occur and take part in thermodynamics as if they were particles."*[2] Based on the asymptotic bootstrap principle, a limiting temperature T_a was introduced in Ref. [174]. Hagedorn introduced the mass spectrum $J(m)$, which represents the distribution of number of resonances produced with masses lying between m and $m + dm$. The relation between the number of resonances produced and their mass given as:

$$J(m) = const.m^{-\frac{5}{2}} e^{\frac{m}{T_a}} \tag{2.6}$$

Here, temperature T_a puts an upper bound on the temperature upto which the strong interaction can occur. This model accurately estimates the total multiplicity of the hadron produced in the collision. The modified version of this model is still used to understand the hadronic phase of the system created in high energy collision.

A comparative study of the QCD thermodynamics obtained from the statistical thermal model and the Lattice QCD simulation was performed in 2003 in the seminal work [175, 176]. Results obtained from the statistical model were in line with Lattice QCD's expectation, further strengthening the need for a statistical approach to study particle production. These seminal works on the statistical description of the spectra of final state particle produced in high energy collision have, over the past several decades, guided the formulation of a large number of models with an aim toward characterizing the particle production spectra. Following the standard laws of statistical mechanics, we can formu-

[1] These lines are taken as it is from Ref. [173]

[2] This line is taken as it is from Ref. [174]

late the distribution function for the transverse momentum spectra within the framework of MB statistics. The detail description of p_{T}-spectra in MB statistics is provided in the next section.

2.2 Boltzmann-Gibbs approach

Boltzmann distribution is a simple distribution function used to describe the distribution of classical particles over various energy states in thermal equilibrium. If we consider purely thermal origin for the system created in high energy collision, BG distribution is the most appropriate choice to start the study of the energy distribution of particles [177, 164]. Further, the quantum statistics such as FD and BE statistics approaches the classical MB statistics at high temperature, and theoretical prediction on the environment required for QGP formation estimated a very high temperature ($\sim 10^{12}\ K$), hence it is justifiable to use the BG approach in the studies related to the particle production spectra. In BG approach, the distribution of particles can be described using the distribution function, which is given in terms of the negative exponential of the energy of macrostates.

In general, for a state s of a statistical system with energy ϵ_s, the average number of particle is given as:

$$n'_s = \frac{1}{e^{\beta(\epsilon_s - \mu)} \pm 1} \tag{2.7}$$

And, if the total number of particle in the system is fixed, we can determine μ using the constraint:

$$\sum_s n'_s = \sum_s \frac{1}{e^{\beta(\epsilon_s - \mu)} \pm 1} = N \tag{2.8}$$

The plus $(+)$ and minus $(-)$ signs in the denominator of the above equation are for Bosons and Fermions, respectively. In the classical limit, where the temperature is very high, a large number of high energy states are occupied, and for such high energy states $\epsilon_s >> \mu$. In order to satisfy the constraint of keeping N fixed, the relation $e^{\beta(\epsilon_s - \mu)} >> 1$ must hold true. So, the distribution of the number of particles is given as:

$$n'_s = e^{-\beta(\epsilon_s - \mu)} \tag{2.9}$$

As discussed above, considering the classical statistics, the probability of occupancy of each microstate or the population of particles in a particular state of the system in equilibrium is

given in the form of the exponential of energy. The number density for a system of particles following BG distribution is given as:

$$n' = \frac{g}{(2\pi)^3} \int d^3p \; exp\left(\frac{\mu - E}{T}\right) \tag{2.10}$$

And the corresponding functional form of energy density and pressure is expressed as:

$$\epsilon = \frac{g}{(2\pi)^3} \int d^3p \; E \; exp\left(\frac{\mu - E}{T}\right) \tag{2.11}$$

$$P = \frac{g}{(2\pi)^3} \int d^3p \; \frac{p^2}{3E} exp\left(\frac{\mu - E}{T}\right) \tag{2.12}$$

The Eq. (2.10) can be written in the differential form as:

$$\frac{d^3N}{dp^3} = \frac{gV}{(2\pi)^3} \; exp\left(\frac{\mu - E}{T}\right) \tag{2.13}$$

where, g is the spin degeneracy factor and the numerical value of g is 1 for pseudoscalar mesons (pions, kaons) and 2 for spin half particles (proton and anti-proton). On expanding the three dimensional momentum element into polar coordinates, we get:

$$d^3p = 2\pi p_T \; dp_T dp_z$$

where p_{T} and p_z are transverse and longitudinal momentum respectively. Using the expansion above, we can modify the right hand side of Eq. (2.13) as:

$$E\frac{d^3N}{dp^3} = \frac{d^2N}{dp_T^2 dy} = \frac{d^2N}{2\pi p_T dp_T dy} \tag{2.14}$$

We used the relation $\frac{dp_z}{E} = dy$ where y is the rapidity variable. Using this modification, we get the final form of the distribution of number of particles as:

$$\frac{d^2N}{2\pi p_T dp_T dy} = E\frac{gV}{(2\pi)^3} \; exp\left(\frac{\mu - E}{T}\right) \tag{2.15}$$

In statistical thermal models, we usually study the energy distribution of the particles; however, as discussed in section 1.6, transverse momenta can be considered as a proxy for the energy of the particle as far as measurement is concerned.

We can express the energy E in terms of transverse mass m_T and rapidity y and the relation is $E = m_T cosh(y)$ where $m_T = \sqrt{m^2 + p_T^2}$. Further, assuming equal number of particles and anti-particles at LHC energies, we can put the value of μ to be zero and also in the mid-rapidity region $cosh(y) \simeq 1$ $(y = 0)$. Considering these assumptions, the final form of the distribution of the transverse momentum spectra following the BG approach can be described as:

$$\frac{d^2N}{2\pi p_T dp_T dy} = m_T \frac{gV}{(2\pi)^3}\, exp\left(\frac{-m_T}{T}\right) \tag{2.16}$$

Application of this equation to study the experimental data on transverse momentum spectra is discussed in the next chapter.

2.3 Summary

To extract the thermodynamical properties of the medium created in high energy collision and also the study of the quark-hadron phase transition require a statistical thermal description of the final state particles. So, the main aim of this chapter is to provide a basic introduction of statistical mechanics and its application to study the particle production spectra in high energy collision. This chapter covers an introduction to the statistical thermal approach and its application to study the transverse momentum spectra. An overview of some of the initial works that have paved the way for the application of statistical approach in high energy physics is also provided in the chapter.

The next chapter, will discuss the different statistical and hydrodynamical inspired approaches to study the transverse momentum spectra. We will also provide the results obtained by fitting the transverse momentum spectra to various distribution functions.

Chapter 3

Phenomenological Models for Transverse Momentum Spectra

In high energy heavy-ion collision experiment, two nuclei moving at relativistic speed collide and create a fireball of quark and gluons. This fireball expands with time undergoing the quark-hadron phase transition followed by the chemical and kinetic freeze-out, after which the hadrons freely stream to the detectors. We observe these final state particles in the detectors and analyze their trajectory to extract physics. Although it is difficult to directly observe the initial stages of the expansion, we utilize the information carried by the final state hadrons to study the properties of the initial fireball, which could give us the insight into the very early stages of the expansion of universe after the Big Bang. In experiments, we measure the trajectory of each particles in form of their kinematics such as the rapidity (y), emission angle (θ), pseudorapidity (η) etc. However, *as far as the study of the thermodynamical properties of the medium created during the collision is concerned,* most important observable is the transverse momentum (p_{T}) spectra which is a proxy for the energy distribution of final state particles.

A good understanding of transverse momentum spectra is crucial in order to understand the thermal and the bulk properties of the QCD matter created during the high energy heavy-ion collision. A proper theoretical description of the form of p_{T}-spectra is necessary to extract the parameter of interest such as the volume (V), temperature (T) $\&$ flow velocity (β_T) etc. The underlying theory, which governs the strongly interacting system is QCD but we cannot apply the perturbative QCD to explain the spectra because of the asymptotic behaviour of the strong coupling constant. The effect is more prominent in the low-p_{T} region

because of the high coupling strength making it impossible to perform the perturbative expansion in this region of the spectra. Hence, the explanation of the spectra depends mostly on the phenomenological models. Among several models, statistical thermal models are widely used due to their simplicity and the possibility to extract macroscopic properties of the system using the microscopic properties of the constituent particles.

The statistical description of particle production was first proposed in 1948 by Koppe in his seminal work in the Ref. [171, 172]. This formalism, along with the efforts by Fermi [173, 178] and Hagedorn [174, 66] are some of the initial works that laid the foundation for the application of statistical thermal methods to study the particle production spectra. A detailed discussion on the statistical thermal approach to study particle spectra can be found in Ref. [179]. Large number of final state particles produced during the heavy-ion collision, quest to study the equilibrium dynamics of the system and idea of a confinement-deconfinement phase transition motivates the statistical thermodynamical treatment of the medium created during such collision experiments. In standard thermodynamics, a macroscopic system can be characterized using the state variables such as energy density (ϵ), number density (n'), pressure (P), chemical potential (μ), temperature (T) etc. The quantity of prime interest in the study of a macroscopic system is the distribution function $f(x, p)$ of the constituent particles. Considering a statistical system of a large number of particles, we can use the distribution function to extract the parameters necessary for the thermodynamical description of the system. The detail thermodynamical treatment of a system with large number of constituent particles is given in chapter 2 of the thesis.

Several phenomenological models have been developed based on the statistical thermodynamics and its extension to other fields with an aim to study different aspects of the p_{T}-spectra. These models can broadly categorized into three main categories.

1. First category include the standard statistical thermal models such as the BG approach, Tsallis statistics, Tsallis-Pareto and Tsallis-factorized statistics. BG approach is the standard choice to study thermodynamical properties of a system with large number of constituent particles in thermal equilibrium. However, BG approach demands the entropy to be extensive and additive, which limits its applicability. This condition can be relaxed in the Tsallis statistics, which is a generalized version of BG approach with an additional parameter q taking care of non-extensivity in the system. Several modification in the Tsallis statistics has also been proposed such

as the Tsallis-Pareto, Tsallis-factorized statistics etc., and some of them will be discussed in the upcoming sections.

2. Next category includes the statistical hydrodynamical models such as the Boltzmann-Gibbs Blast-Wave (BGBW) and the Tsallis Blast-Wave (TBW) model. These models also take into consideration the fluid behaviour of the medium created in heavy-ion collision.

3. The last category of models include some non-standard models such as Single Freeze-Out Model (SFOM), dynamical initial state model, out-of-equilibrium model, q-Weibull model etc. Apart from these, the last category also include several multi-component models such as the two component BG model, Modified Tsallis/Hagedorn model wherein we consider different distribution functions to fit different part of the spectra.

In the upcoming sections of this chapter, we will provide the detailed discussion about the different models that has been used to study the p_{T}-spectra.

3.1 Boltzmann-Gibbs Approach

To explain the energy distribution of particles produced from a purely thermal source, the natural choice is to use BG approach. Detail of the formalism of this statistics is discussed in section 2.2. The functional form of p_{T} distribution in BG is given in Eq. (2.16) and it has been extensively used to fit the spectra [164, 180, 181].

Fitting p_{T}-spectra with the above equation gives the effective temperature, which is different from thermal freeze-out temperature. Considering the particle produced during the collision are of purely thermal origin, we have fitted the p_{T}-spectra of π^+ three different centralities of 2.76 TeV in Fig. 3.1 and at different energies in Fig. 3.2 with BG distribution. However, a significant deviation from thermal BG distribution is observed at low and high-p_{T}, which suggest that simple BG distribution is not sufficient for a complete and consistent description of the system produced during the collision. To tackle this issue a two-component BG model is introduced in the Ref. [169] and the detail of which is discussed below.

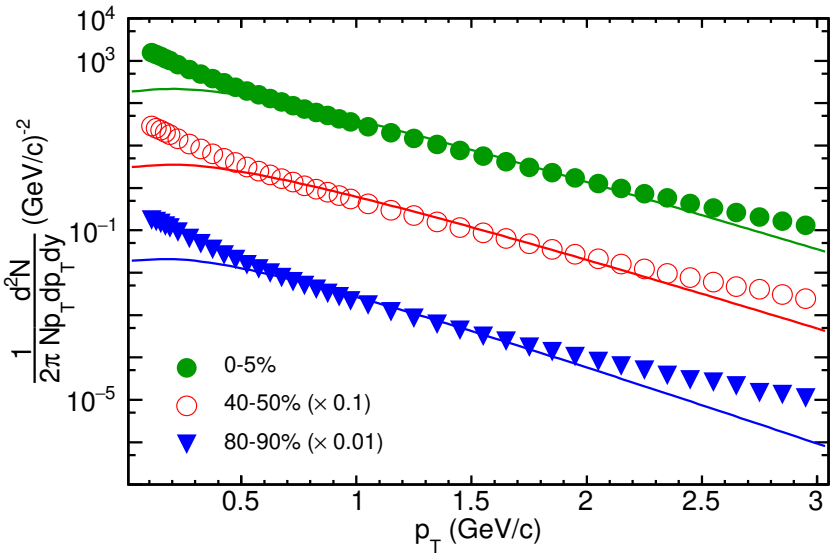

Figure 3.1: The BG distribution fit (Eq. 2.16) to the p_{T}-spectra data of π^+ at three different centralities produced at collision energy of 2.76 TeV [20].

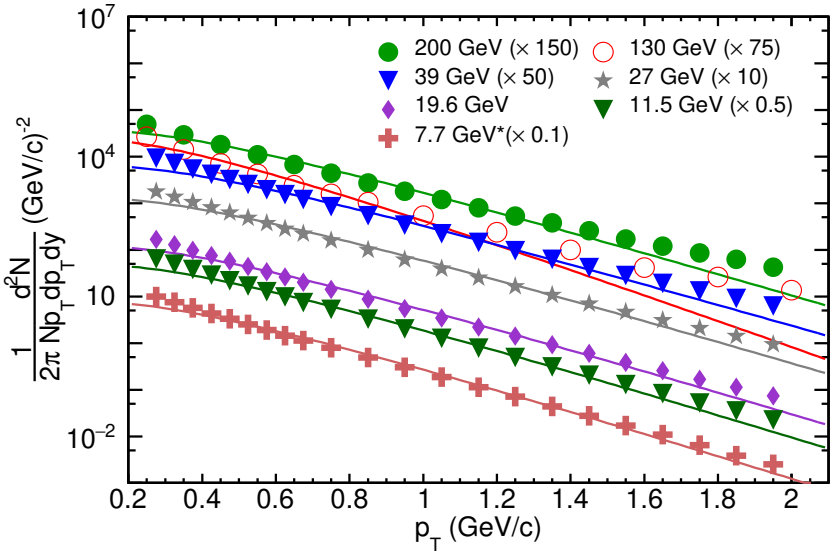

Figure 3.2: The BG distribution fit (Eq. 2.16) to the p_{T}-spectra data of π^+ at different energies [9, 10, 11].

3.1.1 Two-Component BG model

In standard BG approach, the general assumption is that the system is in equilibrium and all the particles originate from the same macroscopic state represented by thermodynamic variables (T, V, μ). The application of BG distribution function Eq. (2.16) requires the system of particle to be in equilibrium as the Eq. (2.16) is obtained by using the maximum entropy principle. Since it is not possible to explain such a complex dynamical processes (particle production in high energy collision is a complex dynamical process) of the formation of

large number of particles using one simple equilibrium state of the system. Assuming that all the particles do not originate from the same macroscopic state of the system, a two-component BG distribution function is introduced in the Ref. [169]. In this formalism, we consider a two-source system with particle originating in two different macrostates of the system. The general function for all three types of particles (bosons, fermions and classical particles) is given as:

$$\begin{aligned}\frac{d^2N}{dp_T dy} =& \frac{gV_1}{(2\pi)^2} p_T\, m_T\, cosh(y) \frac{1}{e^{\frac{m_T\, cosh(y)-\mu_1}{T_1}} + \tau} \\ &+ \frac{gV_2}{(2\pi)^2} p_T\, m_T\, cosh(y) \frac{1}{e^{\frac{m_T\, cosh(y)-\mu_2}{T_2}} + \tau}\end{aligned} \tag{3.1}$$

Here factor τ is the input for type of particle with $\tau = -1$ for Bose-Einstein statistics, $\tau = 1$ for Fermi-Dirac statistics and $\tau = 0$ for Maxwell-Boltzmann statistics. In this two-

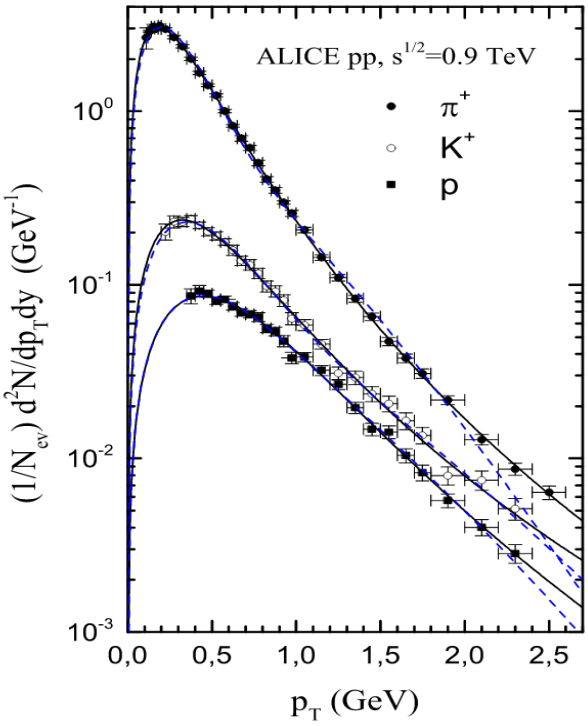

Figure 3.3: The p_{T}-spectra data of π^+, K^+ and p produced at collision energy of 0.9 TeV, the dashed curve represent the fit using the two-component BG distribution Eq. (3.1) whereas the solid curve represent fit to Tsallis-factorized distribution. (The plot is taken from the Ref. [169].)

component form, each term represents a different macrostate of the equilibrium system. The first term in the Eq. (3.1) represents particles originate from one macrostate (T_1, V_1, μ_1) whereas the second term corresponds to the particles from another macrostate (T_2, V_2, μ_2).

The p_{T}-spectra of pions, kaons and protons produced in pp collision at 0.9 TeV are analyzed using this two-component distribution in the Ref. [169] and corresponding fit is shown in the Fig. 3.3. In this distribution, the fit yields two different sets of parameters corresponding to macrostates. The first set corresponds to the low-p_{T} (soft) part of the spectra and gives a smaller temperature and larger volume compared to the second part, which corresponds to the high-p_{T} (hard) part of the spectra. It can be inferred from these results that the high-p_{T} hadrons are created when the system has small volume and high temperature. This two-component formalism provide better fit to the data compared to standard BG distribution, however, it starts to deviate in the higher p_{T} region of the spectra.

The formalisms discussed above do not take into account the hydrodynamical characteristics, however, the observation of collective flow [182] and shear viscosity to entropy density [183] in the heavy-ion collision experiments points toward the fluid-like behaviour of the medium created during collision. An extension of the standard BG distribution was proposed to include the hydrodynamics description of the medium created in heavy-ion collision. This model is known as the Boltzmann Gibbs Blast-Wave (BGBW) model and is discussed in the next section.

3.1.2 Boltzmann Gibbs Blast-Wave Model

During the non-zero impact parameter collision, the initial overlap region is not purely spherical in shape and leads to some geometrical effect in the produced fireball. This initial state spatial anisotropy might not get washed away during the course of expansion and bury some of its imprints into the momentum distribution of the final state particles. Hence, it is customary to consider that the transverse momentum distribution as a composition of two distinct parts. The thermal part is because of the random thermal motion of particles after the kinetic freeze-out and the collective part, which arises from the geometric effect during the collision and leads to the non-isotropic azimuthal distribution of particles. BGBW (also known as BW) is a hydrodynamics motivated model developed to enhance our understanding of kinetic freeze-out and the transverse collective flow. The distribution of transverse

momentum of particles in the BGBW model is of the form:

$$\frac{dN}{p_T dp_T} \propto \int_0^R r\ dr\ m_T\ I_0\left(\frac{p_T\ sinh\ \rho(r)}{T_{kin}}\right) \times K_1\left(\frac{m_T\ cosh\ \rho(r)}{T_{kin}}\right) \tag{3.2}$$

where $\rho(r) = tanh^{-1}\beta$, β represents the transverse radial flow velocity, I_0, K are modified Bessel functions and m_{T} is the transverse mass. We can parameterize the transverse flow velocity profile in the form of a power law given as $\beta_T(r) = \beta_s(r/R)^w$. Here w is the exponent of the flow profile, β_s is the surface flow velocity and r/R provides the information about the radial position of thermal source at any given moment and R is the maximum radius at thermal freeze-out. The average transverse flow velocity ($\langle\beta_T\rangle$) is given in term of β_s and exponent w as $\langle\beta_T\rangle = \beta_s \times \frac{2}{2+w}$ [162]. BGBW fit has been used on many particles

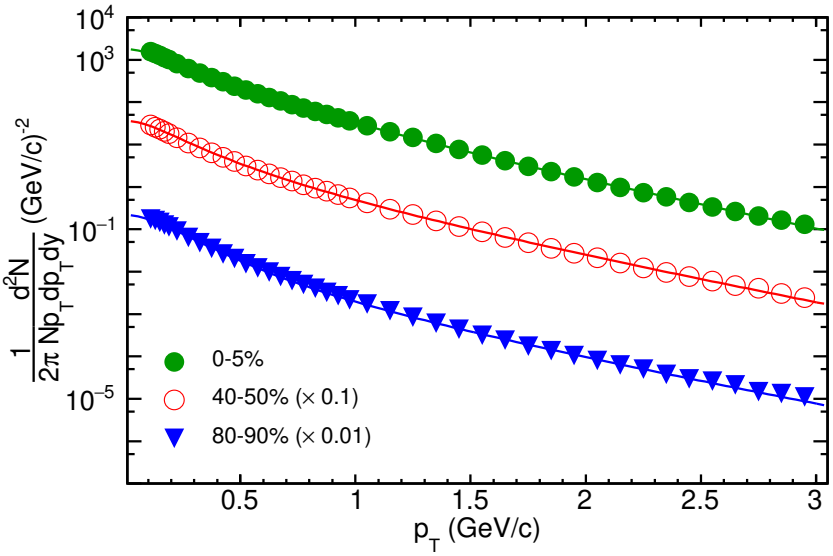

Figure 3.4: The BGBW fit (Eq. 3.2) to the p_{T}-spectra data of π^+ at three different centralities produced at collision energy of 2.76 TeV [20].

to extract the temperature at kinetic freeze-out surface (T_{kin}) and transverse flow velocity (β_T) in order to study the freeze-out properties of the fireball produced in heavy-ion collision at RHIC and LHC [162, 184].

In Ref [162], Ultra-Relativistic Quantum Molecular Dynamics (UrQMD) [185] event generator is used to investigate the energy and centrality dependence of transverse collective flow. An increase in collective flow was reported with an increase in the center of mass energy. Further collective flow also reveals an increasing trend as we go from peripheral to

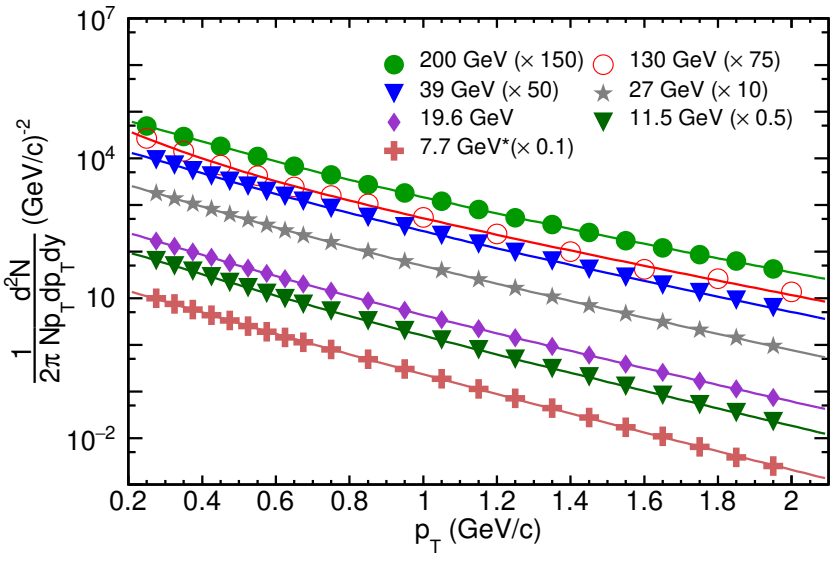

Figure 3.5: The BGBW fit (Eq. 3.2) to the p_{T}-spectra data of π^+ at different energies [9, 10, 11].

central collision. The effective temperature T_{eff} extracted from Boltzmann and Tsallis fit contains a contribution from both thermal part and collective flow part and given as [181]:

$$T_{eff} = T_{kin} + f(\beta_T) \tag{3.3}$$

where $f(\beta_T)$ is some function of collective transverse velocity β_T given in the Ref. [186] and the kinetic freeze-out temperature (T_{kin}) can be extracted using BGBW fit. From Fig. 3.4 and Fig. 3.5 BGBW fit turns out to be a good explanation of the system produced in the collider experiments at different energies as well as different centralities.

3.1.3 Limitation of Standard BG Approach

Although BG approach is very successful in other areas of physics (such as in condensed matter physics), there are some constraints related to its application in high energy physics. One such constraint is that it applies only to the system where the number of the constituent particles is of the order of Avogadro number ($N_A = 6.023 \times 10^{23}$). However, as measured in different experiments, the number of particles produced in a heavy-ion collision is in few thousand only making it difficult to apply the standard BG approach. Another constraint is related to the extensivity of the system, the BG approach requires that the entropy of the system must be additive and extensive. However, there exist a category of system

with long-range interactions where entropy can be non-extensive or non-additive. Some of the processes, including such systems are ferromagnetism, solar neutrinos, black holes, cosmology, high energy collisions of particles. The presence of long-range interaction, the formation of Color Glass Condensate (CGC) and other effects in high energy collision can cause a deviation from thermal equilibrium. These effects might not get washed away during QGP expansion and the multi-particle interaction and affect the final state spectra. This is also reflected in the Fig. 3.1, 3.2 where we observe that the fit function deviate heavily from the experimental data in low- and high-p_{T} region. To take care of such non-equilibrium effect Tsallis statistics has been proposed as a generalization of the BG approach by C. Tsallis in 1988. Detail of this approach is discussed in the next section.

3.2 Tsallis Statistics

The non-extensive statistical mechanics was constructed as a generalization to BG theory utilizing the entropy proposed in 1988 by C. Tsallis in his seminal work [165]. An important property of Tsallis entropy is that it converges to the standard BG entropy within some limit on its parameter q. This parameter gives us information about the extent of non-extensivity in the system. Further, this parameter can also be interpreted as a scaling factor necessary to apply laws of statistical mechanics to the system with the low number of constituent particles.

Tsallis statistics is also applicable to the system where the temperature fluctuates around some mean value T_0 and the non-extensivity parameter q is related to the variance of the temperature as [187, 188]:

$$q - 1 = \frac{Var(T)}{\langle T \rangle^2} \tag{3.4}$$

A major modification that separates the algebra of Tsallis statistics from that of BG is the q-logarithm & q-exponential and they are given as:

$$exp_q(x) = [1 + (q-1)x]^{\frac{1}{q-1}} \tag{3.5}$$

and

$$ln_q(p_i) = \begin{cases} ln(p_i), & \text{if } p_i \geq 0, q = 1 \\ \frac{p_i^{1-q}-1}{1-q}, & \text{if } p_i \geq 0, q \neq 1 \\ undefined, & \text{if } p_i \leq 0 \end{cases}$$

Non-extensive entropy as proposed by Tsallis [165] is defined as:

$$S_q = -k_B \sum_i p_i^q ln_q(p_i) \tag{3.6}$$

$$= -k_B \sum_i p_i^q \frac{p_i^{1-q} - 1}{1-q} \tag{3.7}$$

$$= -k_B \sum_i \frac{p_i - p_i^q}{1-q} \tag{3.8}$$

$$= k_B \frac{1 - \sum_i p_i^q}{q-1} \tag{3.9}$$

which in the limit $q \longrightarrow 1$ gives standard BG entropy

$$S = -k_B \sum_i p_i ln(p_i) \tag{3.10}$$

In Ref. [189, 190], the foundation and application of Tsallis statistics and its thermodynamical aspect has been discussed in great detail.

In order to obtain the functional form of distribution of transverse momentum in Tsallis statistics, one can replace the normal exponential in BG distribution with the q-exponential. The distribution function that has been widely used to study the transverse momentum spectra in the Tsallis framework is given as:

$$\frac{1}{2\pi p_T} \frac{d^2N}{dp_T dy} = \frac{gVm_T}{(2\pi)^3} \left[1 + (q-1)\frac{m_T - \mu}{T}\right]^{-\frac{q}{q-1}} \tag{3.11}$$

Here, m_{T} is the transverse mass and p_{T} is the transverse momentum of the particle, T and V are the temperature and volume of the system, g is the spin degeneracy factor and y is the rapidity of particle. The non-extensive generalization of the Fermi-Dirac and Bose-Einstein statistics and the corresponding entropy is discussed in Ref. [191]. The quantities such as the number density, pressure, energy density etc., can be derived in the framework of Tsallis statistics.

For the distribution function f_i, constraint on the total number of particles N and total energy E in standard BG approach is given as:

$$N = \sum_i f_i \tag{3.12}$$

$$E = \sum_i f_i E_i \tag{3.13}$$

The constraint on N and E in case of Tsallis statistics is given as:

$$\begin{aligned} N &= \sum_i f_i^q \\ E &= \sum_i f_i^q E_i \end{aligned} \tag{3.14}$$

In the classical limit, the functional form of entropy in Tsallis statistics is given as [191]:

$$S_T = -g \sum_i (f_i^q ln_q f_i - f_i) \tag{3.15}$$

were, the q-logarithm $(ln_q(x))$ is defined as:

$$ln_q(x) \equiv \frac{x^{1-q} - 1}{1 - q} \tag{3.16}$$

On substituting the expansion of $ln_q(x)$, we will get the entropy:

$$S_T = g \sum_i \left[\frac{q f_i}{q-1} - \frac{f_i^q}{q-1} \right] \tag{3.17}$$

On maximising the entropy Eq. (3.17) under the constraints given in Eq. (3.14) we will get variational equation:

$$\frac{\delta}{\delta f_i} \left[S_T + \alpha_1 \left(N - \sum_i f_i^q \right) + \alpha_2 \left(E - \sum_i f_i^q E_i \right) \right] = 0 \tag{3.18}$$

In the equation given above, α_1 and α_2 are the Lagrange multipliers corresponding to the total number of particles and total energy, respectively. On solving the variational equation,

we will obtain the distribution function, f_i:

$$f_i = \left[1 + (q-1)\frac{E_i - \mu}{T}\right]^{-\frac{1}{q-1}} \tag{3.19}$$

The function needs to be thermally consistent to be able to apply on a thermodynamical system. Therefore, we will discuss the thermodynamical consistency of the Tsallis formalism by checking whether the distribution function above follows the standard relation in thermodynamics.

3.2.1 Thermodynamics Consistency for Tsallis Statistics

The thermal consistency of a formalism requires it to hold the four fundamental relations as discussed in Ref. [191]:

$$T = \left.\frac{\partial \epsilon}{\partial s}\right|_{n'} \tag{3.20}$$

$$\mu = \left.\frac{\partial \epsilon}{\partial n'}\right|_{s} \tag{3.21}$$

$$n' = \left.\frac{\partial P}{\partial \mu}\right|_{T} \tag{3.22}$$

$$s = \left.\frac{\partial P}{\partial T}\right|_{\mu} \tag{3.23}$$

Using the equation corresponding to the first law of thermodynamics:

$$P = \frac{-E + TS + \mu N}{V} \tag{3.24}$$

To prove the relation we do partial derivative of above equation with respect to μ,

$$\left.\frac{\partial P}{\partial \mu}\right|_{T} = \frac{1}{V}\left[\frac{-\partial E}{\partial \mu} + T\frac{\partial S}{\partial \mu} + N + \mu\frac{\partial N}{\partial \mu}\right] \tag{3.25}$$

On expanding

$$\begin{aligned}\left.\frac{\partial P}{\partial \mu}\right|_{T} = \frac{1}{V}\sum_i \Bigg[f_i^q - \frac{T}{q-1}\left(1 + (q-1)\frac{(E_i - \mu)}{T}\right)\frac{\partial f_i^q}{\partial \mu} \\ + \frac{Tq(1-f_i)^{q-1}}{q-1}\frac{\partial f_i}{\partial \mu}\Bigg]\end{aligned} \tag{3.26}$$

In order to solve the above equation we use the form of f_i from Eq. (3.19) and consider the standard replacement for small intervals $\sum_i \longrightarrow V \int \frac{d^3p}{(2\pi)^3}$. The equation for number density in Tsallis statistics is given as:

$$n' = g \int \frac{d^3p}{(2\pi)^3} \left(1 + (q-1)\frac{(E_i - \mu)}{T}\right)^{\frac{-q}{q-1}} \tag{3.27}$$

Using the equations (3.26) and (3.27) we can verify that:

$$\left.\frac{\partial P}{\partial \mu}\right|_T = n' \tag{3.28}$$

This proves that Tsallis distribution is thermodynamically consistent.

Tsallis distribution has been shown to fit the spectra much nicely compared to the BG distribution. The fit of the transverse momentum spectra at different centralities of 2.76 TeV is provided in the Fig. 3.6 and the corresponding fit at different energies is shown in Fig. 3.7. It is clear from the results presented in Fig. 3.6 and Fig. 3.7 that Tsallis distribution fit $p_{\rm T}$-spectra very nicely compared to BG distribution. This partly solves the problem in fitting the $p_{\rm T}$-spectra and provides a function that can fit the spectra with better accuracy.

The Eq. (3.11) has been used extensively to fit data of $p_{\rm T}$-spectra [192, 191, 193, 194, 195, 188] of different particles produced in the high energy collisions. A review on the implementation of Tsallis statistics to describe the heavy-ion collision is provided in Ref. [196, 187], these works also present a novel interpretation of the non-extensivity parameter. The importance of power-law and the non-extensive statistical mechanics is also discussed in Ref. [197, 198]. A multiple emission source scenario and its Tsallis form are explored in Ref. [199] and the transverse momentum spectra of negatively charged pions are analyzed using these distribution functions.

As evident from the fit results and the discussion presented above, the Tsallis approach to study the particle spectra is more appropriate as compared to the BG approach. The Tsallis statistics can provide a good thermal description of the particle production, however, it lacks the hydrodynamical description of the fluid-like medium created during early stage of the collision. Hence, to include both the effects in a consistent manner the Tsallis Blast-Wave (TBW) model [163] has been proposed and its detail is discussed in the next section.

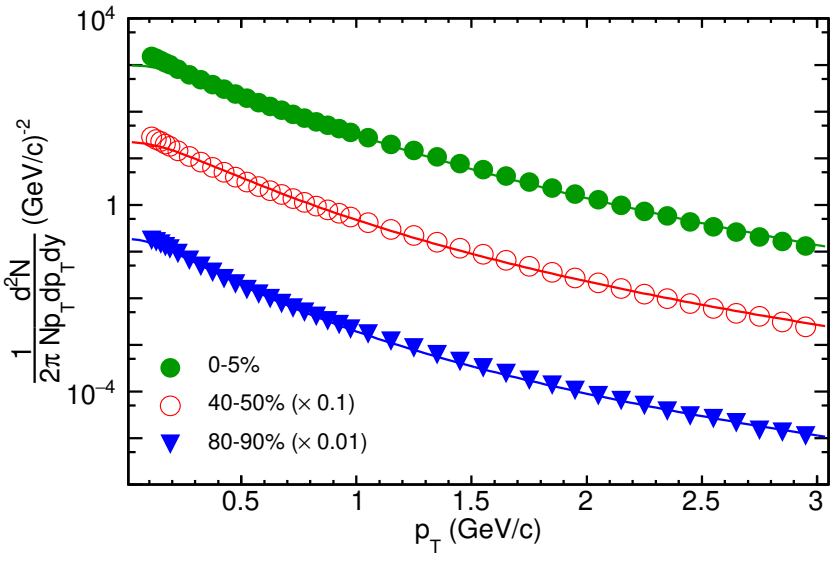

Figure 3.6: The Tsallis fit (Eq. 3.11) to the p_T-spectra data of π^+ at three different centralities produced at collision energy of 2.76 TeV [20].

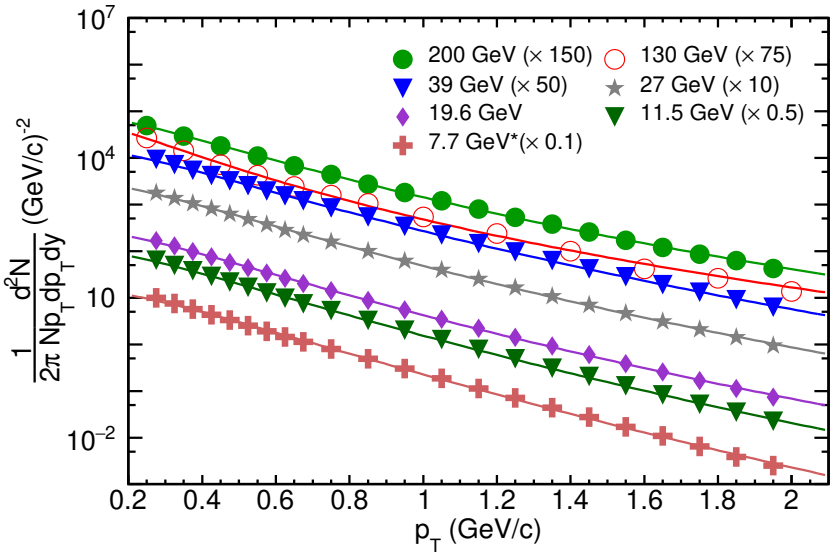

Figure 3.7: The Tsallis fit (Eq. 3.11) to the p_T-spectra data of π^+ at different energies [9, 10, 11].

3.2.2 Tsallis Blast Wave Model

One drawback of the BGBW model is that it assumes the system to be in thermal equilibrium and it is only applicable on the extensive system which might not always be the case. Hence a Tsallis generalization known as TBW model [163] was proposed to take care of the deviation from thermal equilibrium. TBW is a convolution of the Blast-Wave and Tsallis functions with an aim to include the effect of non-extensivity in the system characterized by parameter q. TBW fit function is calculated from BW function by incorporating Tsallis

formalism in place of standard BG formalism [163, 162]. In the framework of TBW model, p_{T}-spectra is given as

$$\frac{dN}{p_T dp_T} \propto m_T \int_{-Y}^{Y} cosh(y)\, dy \int_{-\pi}^{\pi} d\phi \int_{0}^{R} r dr \times \left(1 + \frac{q-1}{T}(m_T\, cosh(y)\, cosh(\rho) - p_T\, sinh(\rho)\, cos\phi)\right)^{\frac{-1}{q-1}} \tag{3.29}$$

Where ρ is the flow profile in transverse direction given as $\rho(r) = tanh^{-1}(\beta_s(r/R)^w)$ and average transverse flow velocity is $\langle\beta_T\rangle = \beta_s \times \frac{2}{2+w}$. Fluctuation around thermal equilibrium may lead to the creation of several hot spots in the system where more particles are created and cause a collective flow and increasing local temperature above equilibrium value. Figures 3.8 and 3.9 show the TBW fit on transverse momentum spectra for positive pions at different centralities and at different energies respectively. It can be concluded from plots above as well as the χ^2/NDF values from Table 3.1 that TBW fit transverse mo-

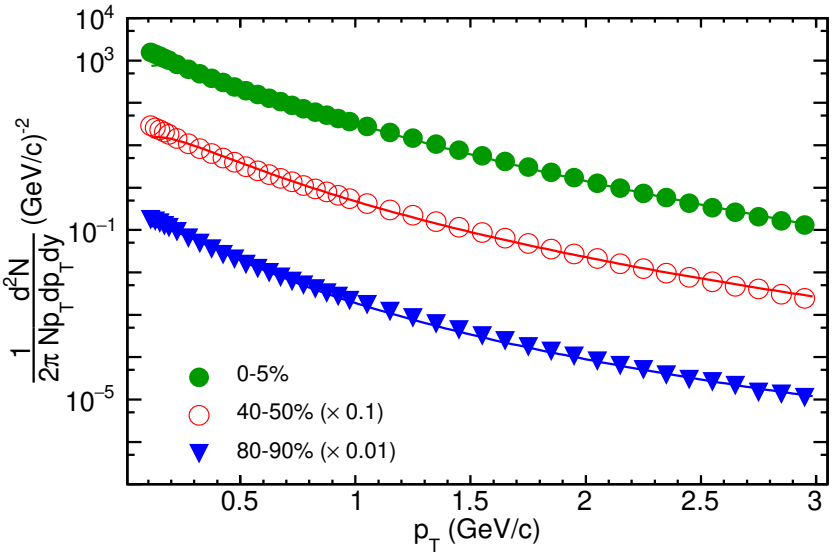

Figure 3.8: The TBW fit (Eq. 3.29) to the p_{T}-spectra data of π^+ at three different centralities produced at collision energy of 2.76 TeV [20].

Table 3.1: This is a table for value of fitting parameters as well as χ^2/NDF at different centralities corresponding to Fig. 3.8.

Centrality	$\langle\beta_T\rangle$	q-1	χ^2/NDF
0-5%	0.363 ± 0.0239	0.091 ± 0.004	2.46
40-50%	0.316 ± 0.029	0.119 ± 0.003	2.99
80-90%	0.243 ± 0.0394	0.141 ± 0.002	1.89

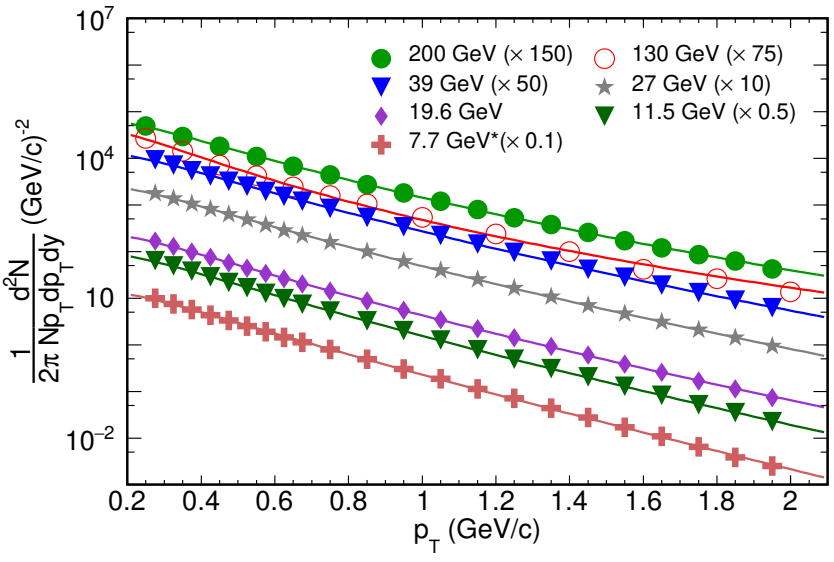

Figure 3.9: The TBW fit (Eq. 3.29) to the p_{T}-spectra data of π^+ at different energies [9, 10, 11].

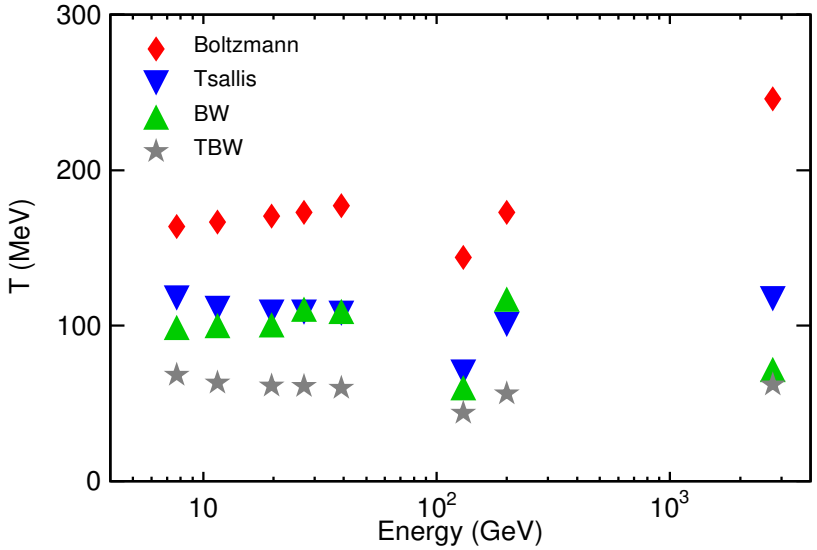

Figure 3.10: This is a plot for value of temperature extracted by fitting π^+ data at different energies with Boltzmann, Tsallis, BGBW and TBW distribution.

mentum spectra quite nicely for $p_{\mathrm{T}} < 3$ GeV/c. The value of the non-extensivity parameter q approaches one, indicating that the system is going from being highly non-equilibrium in the peripheral collision to near equilibrium in the central collision.

In Fig. 3.10 we have plotted the best fit values of temperature parameter at different energies extracted using BG, Tsallis, BGBW and TBW fit to the p_{T}-spectra.

Among all the methods discussed above, the best fit to the experimental data is obtained for the TBW model. However, the applicability of all these models based on BG and

Tsallis approach discussed above is limited to the low-p_{T} region where particle production is dominated by the soft processes. Apart from these formalisms, there are few other non-standard distributions have been developed to study the p_{T}-spectra. Some of these will be discussed in the upcoming sections.

3.3 Out-of-equilibrium p_{T}-spectra

An out-of-equilibrium process for pion production has been explored in the Ref. [200, 21] where the assumption of chemical equilibrium at the time of freeze-out is relaxed. This model considers an excess of positive pions compared to the chemical equilibrium and this excess is incorporated into the formula in term of a positive chemical potential for pions. A cylindrical tube of matter of radius R is considered in this model and is assumed to be expanding longitudinally but with zero transverse flow.

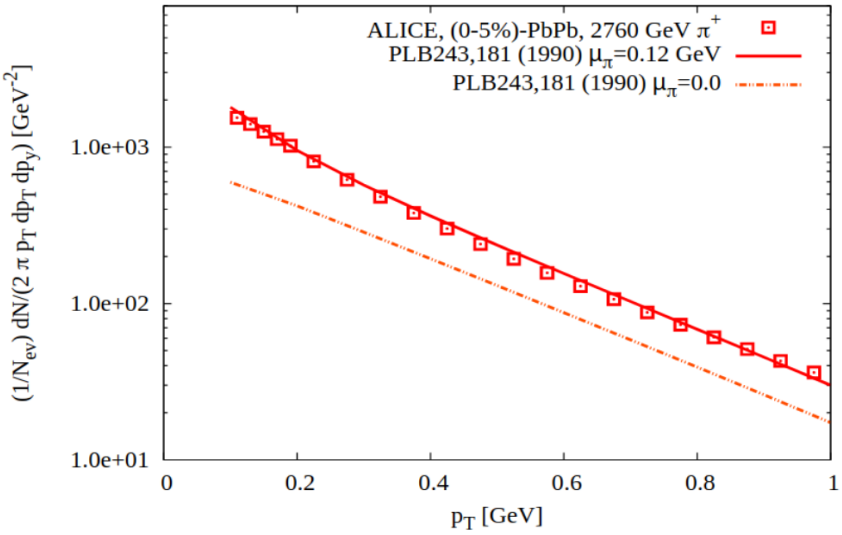

Figure 3.11: The p_{T}-spectra of positive pions produced in most central $PbPb$ collision at 2.76 TeV measured by the ALICE experiment [20], the solid line represent the fit using Eq. (3.30) at $\mu_\pi = 0.12$ whereas the corresponding fit at vanishing $\mu_\pi = 0$ is presented by the dashed-dotted line. (Image taken from Ref. [21])

The distribution function for the p_{T}-spectra of pions at finite rapidity in out-of equilibrium scenario reads:

$$\frac{1}{2\pi p_T}\frac{d^2N_\pi}{dp_T dy} = (\pi R^2 \tau_{fo})\frac{m_T cosh(y)}{(2\pi^3)}\sum_{n=1}^{\infty}(\pm)^{n+1}\, exp(n\frac{\mu_\pi}{T})\, K_1\,(n\frac{m_T}{T}cosh(y)) \quad (3.30)$$

In the above equation, p_{T} represent the transverse momentum and m_{T} is the transverse mass, τ_{fo} is the freeze-out time, y is the rapidity, μ_π is the pion chemical potential and K_1 represent the modified Bessel function.

The p_{T}-spectra of π^+ produced in $PbPb$ collision at 2.76 TeV has been examined within the out-of-equilibrium scenario ($\mu_\pi \neq 0$) in the Ref. [21] and the corresponding fit result is presented in the Fig. 3.11. The best fit to experimental data is obtained for $\mu_\pi = 0.12$ GeV and $\mu_\pi = 0$ line deviate heavily from the data. This result indicate the importance of considering a non-zero chemical potential while studying the spectra of identified particles.

Another non-standard distribution developed to study the p_{T}-spectra is the Single Freeze-Out Model (SFOM) which assumes that the chemical and kinetic freeze-out surface coincides. The detail of this model is discussed in the next section.

3.4 Single Freeze-Out Model

During the expansion of the fireball created in the heavy-ion collision, the system undergoes two stages of freeze-out namely: the chemical freeze-out and the kinetic freeze-out (a description is added in appendix A). It is generally assumed that these two freeze-out occur at different times during the expansion, however, in some of the works [201, 202, 203, 23] a simultaneous kinetic and chemical freeze-out scenario has been explored. SFOM is a convolution of the thermal model along with the hydrodynamics expansion model with an interesting assumption that the time difference between the point when the inelastic interaction ceases and point when the elastic hadrons interaction becomes ineffective is extremely small. This means that the hadrons completely decouple at the freeze-out and there are no elastic rescattering among hadrons after the chemical freeze-out. This model also includes the contribution from all the resonance decay in the calculation of hadron multiplicities and the spectra.

The soft part of the p_{T}-spectra of particles like $\pi, K, p, \Omega, \lambda, \Xi$ at SPS and RHIC energies have been accurately reproduced using this model. From the Fig. 3.12 we observe a good agreement between the experimental data of identified hadrons produced in 200 GeV $AuAu$ collision with the SFOM. These results suggest that the approximation considered in the SFOM regarding the simultaneous freeze-out works well for the study of p_{T}-spectra.

All the models discussed above are used primarily to study the low-p_{T} part of the spec-

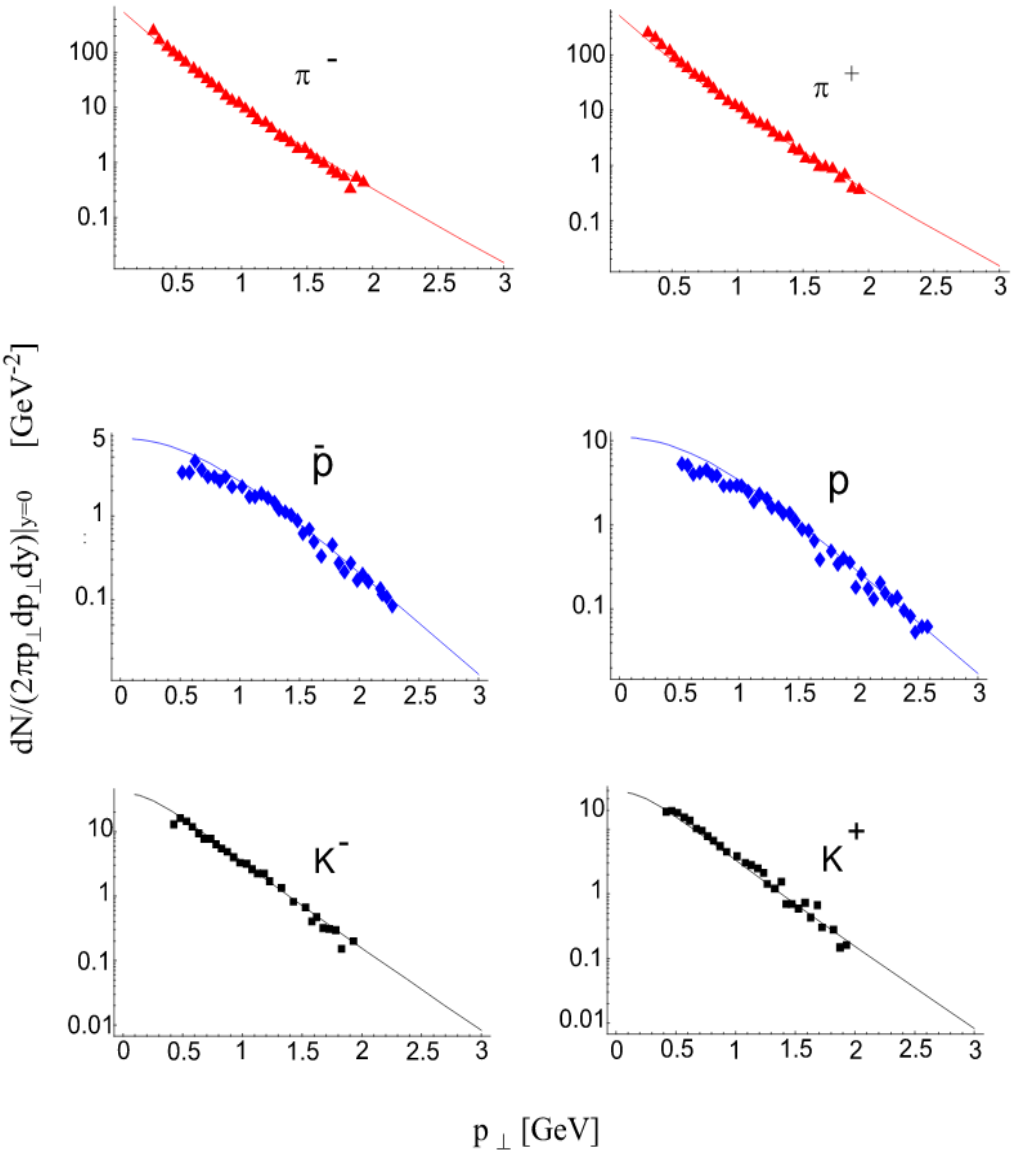

Figure 3.12: The SFOM fit p_{T}-spectra of identified hadrons produced in most central $AuAu$ collision at 200 GeV measured by the BRAHMS experiment [22]. (Image taken from Ref. [23])

tra and they start to deviate from the experimental data in high-p_{T} region. The particle production in high-p_{T} region is dominated by the hard scattering process and we use the QCD inspired power-law form of the distribution function to study this regime of the spectra. There are certain efforts made to study the broad p_{T} range and some of them will be discussed below.

3.5 q-Weibull Distribution

In the hunt to determine a distribution function that can be used to study a broad $p_{\rm T}$ range of the spectra, physicists have tried to explore the applicability of q-Weibull distribution. The Weibull distribution is a continuous probability distribution described in 1951 by Swedish mathematician Waloddi Weibull. In Weibull distribution, the probability distribution function is given as:

$$P(x,\lambda,k) = \begin{cases} \frac{k}{\lambda}\left(\frac{x}{\lambda}\right)^{k-1} \; e^{-(x/\lambda)^k} & x \geq 0 \\ 0 & x < 0 \end{cases}$$

Here k represent the shape parameter and λ is the scale parameter of the distribution and k & $\lambda > 0$. Weibull distribution has been used previously to describe the process where the dynamical evolution of the system is driven by the fragmentation and sequential branching [204, 205], which makes it a suitable & alternate choice to be tested in particle production study.

With an aim toward developing a thermal model to study broader $p_{\rm T}$ range of the spectra, the Tsallis formalism has been incorporated to the Weibull distribution in the Ref. [24] giving the q-Weibull distribution of the form:

$$P_q(x,q,\lambda,k) = \frac{k}{\lambda}\left(\frac{x}{\lambda}\right)^{k-1} \; e_q^{-(\frac{x}{\lambda})^k} \tag{3.31}$$

where

$$e_q^{-(\frac{x}{\lambda})^k} = \left(1-(1-q)\left(\frac{x}{\lambda}\right)^k\right)^{\left(\frac{1}{1-q}\right)} \tag{3.32}$$

In the limit $k = 1$ and $q \neq 1$,Eq. (3.32) reduces to q-exponential.

Almost all of the distribution function discussed above are applicable in a limited $p_{\rm T}$ range, mainly in the low-$p_{\rm T}$ region. However, q-Weibull show promising results in a broad range of $p_{\rm T}$ including high-$p_{\rm T}$ regime.

The Fig. 3.13 shows the fit of q-Weibull distribution to a broad $p_{\rm T}$ range and we observe a good agreement with the data. The fit for low-$p_{\rm T}$ range is presented in the Fig. 3.14 and these result suggest that the q-Weibull distribution provide a good explanation to the data.

Two different $p_{\rm T}$ range has been fitted with the q-Weibull distribution in the Ref. [24] to study the difference in the behaviour of fit parameters when particle production is dominated by hard and soft processes. Soft processes dominate in the low-$p_{\rm T}$ range of spectra

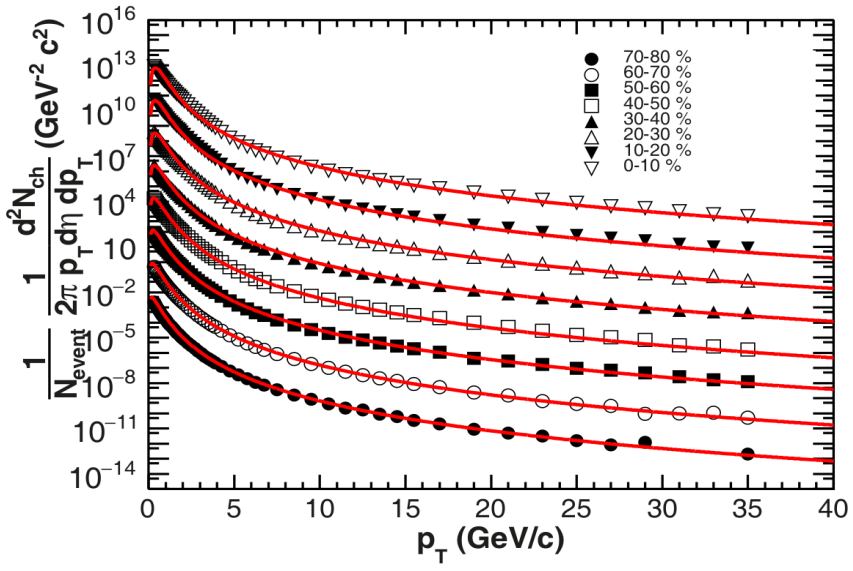

Figure 3.13: The q-Weibull fit (Eq. 3.31) to the p_{T}-spectra data of charged hadrons at different centralities produced in collision energy of 2.76 TeV measured by the ALICE experiment [16]. (Image taken from the Ref. [24])

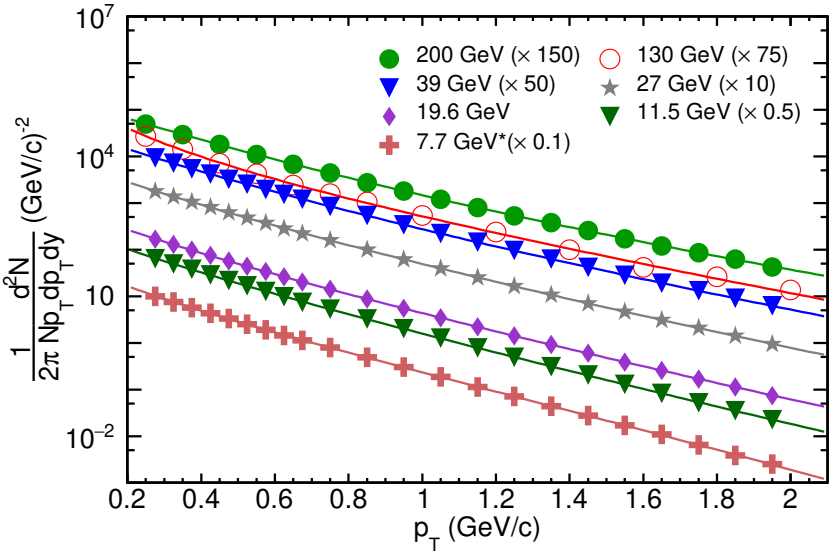

Figure 3.14: The q-Weibull fit (Eq. 3.31) to the p_{T}-spectra data of π^+ at different energies [9, 10, 11].

(usually $p_{\mathrm{T}} < 2$ GeV/c) and the rest is taken to study particle production dominated by hard processes. For the fitting with $p_{\mathrm{T}} < 2$ GeV/c, q value increases as we go from central to peripheral collision, which is similar to the trend observed in Tsallis as well as TBW fits. However, if we consider the entire p_{T} range, there is a trend reversal, with more central collisions having higher values of q. This can be attributed to a larger deviation from equilibrium compared to peripheral collisions. This suggests that pQCD hard scattering

processes (which dominates the high-p_{T} regime) favor non-equilibrium scenario.

3.6 Modified Tsallis/Hagedron Distribution

As discussed in the section 1.4.1, the quenching of jet passing through the QGP medium leads to modification in p_{T}-spectra at high-p_{T} values. The piecewise modification in Tsallis/Hagedron function has been implemented in the Ref. [25] to incorporate the effect of the in-medium energy losses with an additional feature to include the transverse collective flow. Modified function to describe p_{T}-spectra is given as:

$$E\frac{d^3N}{dp^3} = \begin{cases} A_1\left[exp\left(-\frac{\beta p_T}{p_{[1]}}\right) + \frac{m_T}{p_{[1]}}\right]^{-n_{[1]}} & p_T < p_{T_{th}} \\ A_2\left[\frac{B}{p_{[2]}}\left(\frac{p_t}{q_0}\right)^{\alpha} + \frac{m_T}{p_{[2]}}\right]^{-n_{[2]}} & p_t > p_{T_{th}} \end{cases}$$

Here the first function takes care of thermal and flow effect in the spectra with tempera-

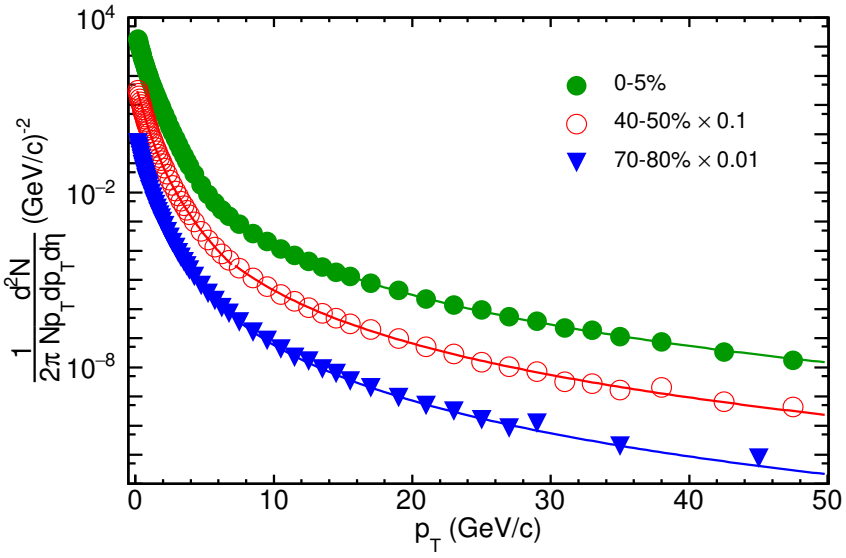

Figure 3.15: Modified Tsallis function [25] fitted to charged particle spectra produced in $PbPb$ collision at 2.76 TeV [16].

ture given as $T = p_{[1]}/n_{[1]}$ and β is transverse flow velocity. Parameter α quantifies the in-medium energy loss regime for the light quarks in medium, where $p_{[2]}$ quantifies the medium size. In Fig. 3.15, we have fitted charged hadron spectra with p_{T} upto 50 GeV/c produced in $PbPb$ collision at 2.76 TeV.

In Ref. [25], the distribution function has been shown to fit p_{T}-spectra very nicely over a wide range of p_{T} from 0.2 to 300 GeV/c for charged particle spectra produced in $PbPb$ col-

lision at 5.02 TeV.

It has been observed that the low-energy section of the hadron transverse energy E_T spectra shows exponential dependence on E_T whereas the spectra looks more like a power law at high E_T. Another two-component model has been introduced in Ref. [206, 207] to explain the hadron spectra. This model uses a combination of exponential form and the power-law form given as:

$$\frac{d^2\sigma}{\pi dy dp_t^2} = A_e exp\left(-\frac{E_{Tkin}}{T_e}\right) + \frac{A_p}{\left(1+\frac{p_T^2}{T_p^2 N_p}\right)N_p} \tag{3.33}$$

Here $E_{Tkin} = \sqrt{p_T^2 + m^2} - m$ and m is the hadron mass. The rest of the parameters A_e, A_p, T_e, T_p, N_p are free parameters and can be obtained by fitting the data with the above function. A significant improvement in the data-to-fit ratio compared to a single function has been reported for inclusive charged particle spectra at different energies. Although these multi-component models provide a good fit to the spectra, however, and important point to consider is that there is no fine line separating the two region making it difficult to apply a piecewise function.

3.7 Summary

Before discussing the new model, it is customary to provide brief introduction of the existing phenomenological models that are being used to study the transverse momentum spectra. In this chapter, we have introduced some of the widely used models along with the corresponding fit results to the spectra data.

1. The statistical thermal models form the backbone of the study related to the parameterization of transverse momentum spectra in high energy collision. Considering the thermal distribution of particles, most natural choice to study the spectra is the BG distribution, however, it deviates heavily from the experimental data. The applicability of BG distribution is constrained only to the extensive system with number of constituents is of the order of Avogadro number, hence, a generalization is required to explain the system created in high energy collision where number of constituents particle is low ($10^2 - 10^4$). This generalization was put forth by *Brazillian physicist Constantino Tsallis in the year 1988*. Tsallis statistics introduces a non-extensivity

parameter q making the standard statistical mechanics applicable to the non-extensive system. The q parameter also acts as a scale factor necessary to apply the standard BG approach to system with low number of particles.The distribution function based on Tsallis statistics provide better fit to the p_{T}-spectra compared to the BG distribution.

2. The observation of flow and shear viscosity to entropy density points toward the fluid-like behaviour of the system, limiting the use of simple BG or Tsallis statistics. The hydrodynamics inspired extension of these distribution, known as Boltzmann-Gibbs Blast Wave (BGBW) and Tsallis Blast Wave (TBW), has been provided in the Ref. [163, 162]. These models incorporates the flow effects into the statistical thermal distribution of particles and provide a better explanation to the experimental data. However, there are certain constraints limiting the applicability of these models to low-p_{T} region.

3. The transverse momentum spectra can be divided into two different regions: the low-p_{T} and the high-p_{T} region. The particle production in the low-p_{T} regime is dominated by the soft process and the statistical thermal $\&$ hydrodynamical models discussed above are primarily used to study this region of the spectra. The hard scattering processes dominate the production of high-p_{T} particles and a QCD inspired power-law form of the distribution function is used to the high-p_{T} region. Also, there are several non-standard models such as q-Weibull and several multi-component methods have been formulated to study the broader p_{T} range of the spectra but there is no fine line separating the two regions [21]. Hence, the search for a distribution function to study broad p_{T} range is still an open problem.

In the next chapter we have provided the detailed description of the unified statistical framework, developed to study soft processes and hard scattering processes in a unified manner.

Chapter 4

Unified Statistical Framework

The proper parameterization of the transverse momentum spectra is an important task and it can provide the crucial information related to the medium created in the high energy heavy-ion collision. Several theoretical models have been developed to study the transverse momentum spectra in collider experiments. A brief discussion of various models are given in chapter 3. The statistical thermal & hydrodynamical models nicely explain the low-$p_{\rm T}$ part of the spectra, however, these models start to deviate heavily from the experimental data in the high-$p_{\rm T}$ region. As a solution, a power-law form of distribution function is used to study high-$p_{\rm T}$ region. Also, several two- and multi-component model have been developed since it is difficult to explain high- & low-$p_{\rm T}$ region using a single probability distribution function. However, characterizing the clear boundary between these two regions is a complex task. Therefore, formulating a distribution function to study the physics of both regions in a unified manner is still an open problem and our interest lies in tackling this problem using Pearson probability distribution.

Calculation based on the perturbative QCD suggest that the $p_{\rm T}$-spectra in the high-$p_{\rm T}$ region can be analyzed using the power-law form of distribution function, which is expressed as [199, 208, 209, 210, 211, 212]:

$$f(p_T) = \frac{1}{N}\frac{dN}{dp_T} = Ap_T\left(1+\frac{p_T}{p_0}\right)^{-n} \tag{4.1}$$

In the equation above, A is the normalization constant and n & p_0 are the free parameters obtained by fitting the function with the experimental data. Our proposal to the question stated above is to develop a generalized formalism by combining inverse power-law and

Tsallis distribution in a consistent manner.

4.1 Proposal

The proposal is to search for a distribution function which should explain the transverse momentum spectra of final state particles in heavy-ion collision. ***New Approach:*** The primary goal is to provide a distribution function that not only can mathematically explain the p_{T}-spectra, but also it should be able to establish the particle production mechanisms in the produced system. Mathematically, one can start with the important question *why not to chose a simple polynomial function to fit the spectra over a thermodynamics function?*.

4.1.1 Polynomial function

We have tried to check whether we can use a simple polynomial function to fit the transverse momentum spectra. We fitted the p_{T}-spectra of charged hadron produced in 2.76 TeV $PbPb$ collision with a fifth order polynomial given as:

$$f(p_T) = p_0 * (p_1 x^{-1} + p_2 x^{-2} + p_3 x^{-3} + p_4 x^{-4} + p_5 x^{-5}) \tag{4.2}$$

Here the parameters p_0, p_1, p_2, p_3, p_4 & p_5 are the free parameters that can be obtained by fitting the data. The polynomial fit to the experimental data is presented in the Fig. 4.1. The

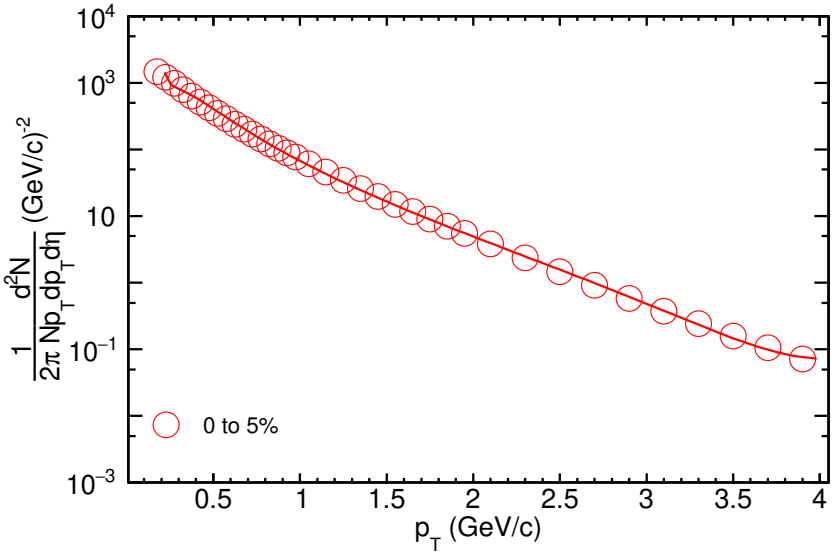

Figure 4.1: The polynomial function fitted to charged particle spectra produced in $PbPb$ collision at 2.76 TeV [16].

best fit value of χ^2/NDF is 0.428 suggesting an excellent explanation to the experimental data. *Although the polynomial function (Eq. 4.2) mathematically fits to the data, however, it is not simply possible to attribute all extracted parameters into appropriate physics correspondences.*. Hence it lacks the ability of explaining physics out of pure polynomial functions. Therefore, we need a distribution function which must leverage the physics connections.

One can start from already available models that are used to explain a statistical thermal system must follows the standard laws of thermodynamics. Also, in order to extract detail physics information from the $p_{\rm T}$-spectra, a model should include the essence of both soft process and hard scattering processes. In this direction, we have explored different distribution function and observed that the Pearson probability distribution has the structure to include both Tsallis and the inverse power-law form of functions in a unified manner. Detail of Pearson function is discussed in the next section.

4.1.2 Pearson Distribution

Pearson probability distribution was first introduced in 1895 by Karl Pearson in his seminal work [213]. The main idea of introducing this formalism was to classify a distribution function based on the first four moments of the distribution. These moments are related to the mean, standard deviation, skewness and kurtosis of the distribution and they specify the shape of a probability distribution. The first moment of the distribution is mean and it represents the average value, whereas the standard deviation shows the spread or dispersion in the data around the mean value. Skewness and kurtosis are the shape parameters. The skewness represents the asymmetry in the data around the mean value and the peakedness of the distribution is quantified using kurtosis. Pearson family of the curve includes a large number of distribution function such as Gaussian, gamma, beta, inverse-gamma, Student's t-distribution, exponential etc. Hence, it is considered as the generalized probability distribution function and it is used extensively in a broad spectrum of fields such as geophysics, financial marketing and biostatistics etc. In Pearson formalism, the probability density $p(x)$ is presented in terms of a differential equation [214]:

$$\frac{1}{p(x)}\frac{dp(x)}{dx} + \frac{a+x}{b_0 + b_1 x + b_2 x^2} = 0 \tag{4.3}$$

with the parameters a, b_0, b_1, b_2 related to the first four moments given as:

$$a = b_1 = \frac{m_3(m_4 + 3m_2^2)}{10m_2m_4 - 18m_2^3 - 12m_3^2} \tag{4.4}$$

$$b_0 = \frac{m_2(4m_2m_4 - 3m_3^2)}{10m_2m_4 - 18m_2^3 - 12m_3^2} \tag{4.5}$$

$$b_2 = \frac{2m_2m_4 - 6m_2^3 - 3m_3^2}{10m_2m_4 - 18m_2^3 - 12m_3^2} \tag{4.6}$$

In the relations above, m_1, m_2, m_3 and m_4 are the first four central moments respectively, and $m_1 = 0$.

Depending on the root of the quadratic equation present in the denominator of Eq. (4.3), we can classify the Pearson family of curves into twelve different kinds. A selection criterion known as the Pearson criteria, k_p, is also used to classify the curves. It is defined as:

$$k_p = \frac{b_1^2}{4b_0b_2} \tag{4.7}$$

And different values and range of the value of k_p determine the type of the curve. A brief discussion about the different type of Pearson curves is provided in section 4.2 and one can refer to the article [215] for more details.

4.2 Different Solution of Pearson Probability Distribution

As already discussed, considering the differential equation involving the Pearson probability function $p(x)$:

$$\frac{1}{p(x)}\frac{dp(x)}{dx} + \frac{a + x}{b_0 + b_1x + b_2x^2} = 0 \tag{4.8}$$

depending on the root of the quadratic equation in the denominator and the constraints on its parameters, twelve different category of solution [216, 217] can be obtained. In this section, we will provide a brief discussion on the different type of solutions to the above equation.

Type I :

$$p(x) = C\left(1 + \frac{x}{a_1}\right)^{m_1}\left(1 - \frac{x}{a_2}\right)^{m_2} \tag{4.9}$$

$$-a_1 < x < a_2 \;\;\&\;\; m_1, m_2 > 0$$

Beta distribution of first kind falls into this category.

Type II :

$$p(x) = C\left(1 - \frac{x^2}{a^2}\right)^{m'} \tag{4.10}$$

$$-a < x < a \ \ \& \ \ m' > -1$$

Type III :

$$p(x) = C\left(1 + \frac{x}{a}\right)^{\mu a} exp(-\mu x) \tag{4.11}$$

$$-a < x < \infty \ \ \& \ \ \mu, a > -1$$

Chi-squared distribution and Gamma distribution belong to this type.

Type IV :

$$p(x) = C\left(1 + \frac{x^2}{a^2}\right)^{-m'} exp(-\mu tan^{-1}(x/a)) \tag{4.12}$$

$$-\infty < x < \infty \ \ \& \ \ a, m', \mu > 0$$

Cauchy distribution is a limiting case of this particular type.

Type V :

$$p(x) = Cx^{-p} exp\left\{-(\alpha/x)\right\} \tag{4.13}$$

$$0 < x < \infty \ \ \& \ \ \alpha > 0, p > 1$$

Inverse-gamma distribution belongs to this category.

Type VI :

$$p(x) = Cx^{-p}(x - a)^q \tag{4.14}$$

$$a < x < \infty \ \ \& \ \ p < 1, q > -1, p > q - 1$$

Beta distribution of second kind and Fisher–Snedecor distribution (F-distribution) belong to this category of Pearson solution.

Type VII :

$$p(x) = C\left(1 + \frac{x^2}{a^2}\right)^{-m'} \tag{4.15}$$

$$-\infty < x < \infty \ \ \& \ \ m' > 1/2$$

Student's t distribution is one such example of this type.

Type VIII :

$$p(x) = C\left(1 + \frac{x}{a}\right)^{-m'} \tag{4.16}$$

$$-a < x \geq 0 \ \ \& \ \ m' > 1$$

Type IX :

$$p(x) = C\left(1 + \frac{x}{a}\right)^{m'} \tag{4.17}$$

$$-a < x \geq 0 \ \ \& \ \ m' > -1$$

Type X :

$$p(x) = C\ exp(-(x - m')/\sigma) \tag{4.18}$$

$$m' \leq x < \infty \ \ \& \ \ \sigma > 0$$

This type represents the exponential distribution.

Type XI :

$$p(x) = Cx^{-m'} \tag{4.19}$$

$$b \leq x < \infty \ \ \& \ \ m > 1$$

Pareto distribution falls into this category.

Type XII :

$$p(x) = C\left(1 + \frac{x}{a}\right)^{m'}\left(1 + \frac{x}{b}\right)^{-m'} \tag{4.20}$$

$$-a < x < b \ \ \& \ \ |m'| < 1$$

4.3 A Generalization of Tsallis Distribution

On solving the differential equation given in Eq. (4.3), we get the Pearson probability density function as follows:

$$p(x) = C' \exp \int -\frac{P(x)}{Q(x)} dx \tag{4.21}$$

$$= C' \exp \int -\frac{a_0 + a_1 x}{b_0 + b_1 x + b_2 x^2} dx \tag{4.22}$$

We can express the quadratic equation in following form,

$$b_0 + b_1 x + b_2 x^2 = b_2 (x + \alpha)(x + \beta) \tag{4.23}$$

$$p(x) = C \exp \int \frac{a_0 + a_1 x}{(x + \alpha)(x + \beta)} dx \tag{4.24}$$

$$= C \exp \int \frac{u}{x + \alpha} + \frac{v}{x + \beta} dx \tag{4.25}$$

Where u and v have following definition.

$$u = -\frac{a_0 - a_1 \alpha}{\alpha - \beta} \tag{4.26}$$

$$v = \frac{a_0 - a_1 \beta}{\alpha - \beta} \tag{4.27}$$

After integrating the Eq. (4.23),

$$p(x) = C \exp \{ ln(x + \alpha)^u + ln(x + \beta)^v \} \tag{4.28}$$

$$= C(x + \alpha)^u (x + \beta)^v \tag{4.29}$$

A general solution to the above differential equation (Eq. 4.3) can be written as:

$$p(x) = C(e + x)^f (g + x)^h \tag{4.30}$$

Here the parameters $e, f, g \ \& \ h$ are free parameters and C is a normalization constant.

We can prove that when numerator $P(x)$ is constant and the denominator $Q(x)$ in Eq. (4.21) is unity, the Pearson function reduces to the exponential function. Further, when $P(x)$ is a

linear function of x and $Q(x)$ is unity, we get the Normal or Gaussian distribution. Since the Pearson function reduces to exponential within some limits, it is possible to find a relation between the Pearson function and the thermodynamic system. This suggests that the Pearson function can be reduced to the Tsallis and BG functions.

Using simple modification, we can rewrite the Eq. (4.30) as:

$$p(x) = B\left(1+\frac{x}{e}\right)^{f}\left(1+\frac{x}{g}\right)^{h} \tag{4.31}$$

with $B = Ce^f g^h$. In the above equation, if we do the replacements $g = \frac{T}{q-1}$, $h = -\frac{q}{q-1}$, $f = -n$ and $e = p_0$, we get:

$$p(x) = B\left(1+\frac{p_T}{p_0}\right)^{-n}\left(1+(q-1)\frac{p_T}{T}\right)^{-\frac{q}{q-1}} \tag{4.32}$$

where,

$$B = C\frac{1}{(p_0)^n}\left(\frac{T}{q-1}\right)^{-\frac{q}{q-1}} \tag{4.33}$$

Hence the functional form of transverse momentum spectra in unified formalism is given as:

$$\frac{1}{2\pi p_T}\frac{d^2N}{dp_T dy} = B'\left(1+\frac{p_T}{p_0}\right)^{-n}\left(1+(q-1)\frac{p_T}{T}\right)^{-\frac{q}{q-1}} \tag{4.34}$$

where $B' = B \times \frac{V}{(2\pi)^3}$ with the additional $\frac{V}{(2\pi)^3}$ comes when we move from summation to integration.

While proposing a generalized theory, an important aspect to consider is backward compatibility. Since the unified formalism is proposed as a generalization to the Tsallis distribution, within some limit on the parameters it must reduce to the Tsallis form of distribution. It is proved in section 4.4 that in the limit $n = -1$ and $p_0 = 0$ unified distribution Eq. (4.34) reduces to the Tsallis form upto some normalization factor.

4.4 Backward Compatibility

We have stated that the unified distribution is a generalization of Tsallis statistics and it reduces to the same in limit n = -1 and p_0 = 0. The proof of this backward compatibility of distribution function as well as entropy is discussed below.

The functional form of transverse momentum spectra in case of unified distribution is

given as:

$$\frac{1}{2\pi p_T}\frac{d^2N}{dp_T dy} = B'\left(1+\frac{p_T}{p_0}\right)^{-n}\left(1+(q-1)\frac{p_T}{T}\right)^{-\frac{q}{q-1}} \tag{4.35}$$

which can be further simplified to:

$$\frac{1}{2\pi p_T}\frac{d^2N}{dp_T dy} = C\frac{gV}{(2\pi)^3}\frac{1}{(p_0)^n}\left(\frac{T}{q-1}\right)^{-\frac{q}{q-1}}\left(1+\frac{p_T}{p_0}\right)^{-n}\left(1+(q-1)\frac{p_T}{T}\right)^{-\frac{q}{q-1}} \tag{4.36}$$

Placing all terms of nth power together we get:

$$\frac{1}{2\pi p_T}\frac{d^2N}{dp_T dy} = C\frac{gV}{(2\pi)^3}\left(\frac{T}{q-1}\right)^{-\frac{q}{q-1}}(p_0+p_T)^{-n}\left(1+(q-1)\frac{p_T}{T}\right)^{-\frac{q}{q-1}} \tag{4.37}$$

Putting $n = -1$ and $p_0 = 0$ we get the Tsallis distribution upto some normalization factor.

$$\frac{1}{2\pi p_T}\frac{d^2N}{dp_T dy} = C\frac{gV}{(2\pi)^3}\left(\frac{T}{q-1}\right)^{-\frac{q}{q-1}} p_T\left(1+(q-1)\frac{p_T}{T}\right)^{-\frac{q}{q-1}} \tag{4.38}$$

Further, the entropy in case of unified distribution is given as:

$$S_p = \frac{qf_i}{(q-1)\left(Bf_E\right)^{\frac{1}{q}-1}} - \frac{f_i^q}{q-1} \tag{4.39}$$

where f_E is of the form:

$$Bf_E = \frac{C}{E(p_0)^n}\left(\frac{T}{q-1}\right)^{-\frac{q}{q-1}}\left(1+\frac{E}{p_0}\right)^{-n} \tag{4.40}$$

$$Bf_E = C\left(\frac{T}{q-1}\right)^{-\frac{q}{q-1}}\frac{1}{E}\left(p_0+E\right)^{-n} \tag{4.41}$$

which, in the limit $n = -1$ and $p_0 = 0$ reduces to unity and hence simplifying the the entropy to its Tsallis form:

$$S_{Ta} = C\left(\frac{T}{q-1}\right)^{-\frac{q}{q-1}}\left(\frac{qf_{Ta}}{(q-1)} - \frac{f_{Ta}^q}{q-1}\right) \tag{4.42}$$

From the derivation presented above, it can be inferred that the unified function can be considered as a generalization to the Tsallis formalism with an additional part that needs to be explored.

4.5 Parameter Dependence of BG, Tsallis and unified distribution function

It is important to study how the parameters of a distribution function affects the overall form, hence, in this section we will discuss the dependence of different fit parameters on the BG, Tsallis and unified distribution function. In the fig. 4.2, we have shown the variation

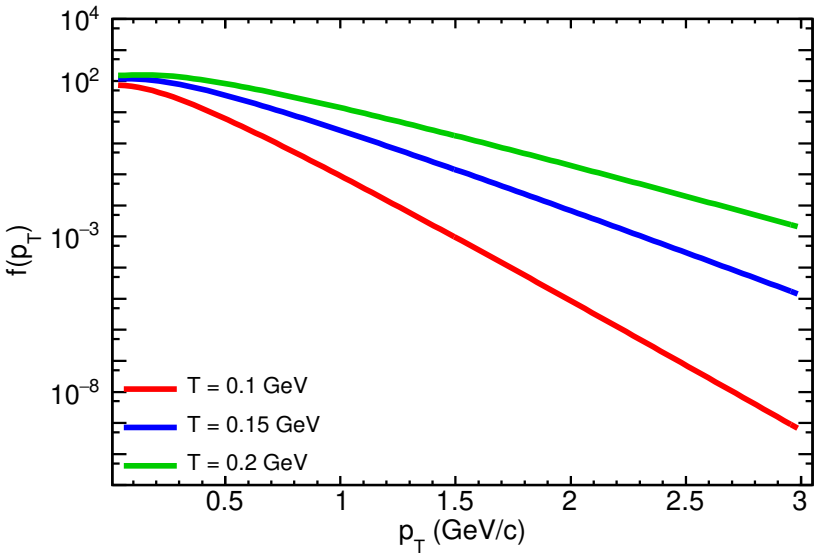

Figure 4.2: The variation of BG distribution function with the change in temperature.

of BG distribution function (Eq. 2.16) with the fit parameter T. It is observed that with the increase in the temperature, the function shifts upward and the gap between them increases as we move toward higher p_{T}.

The variation of Tsallis distribution function (Eq. 3.11) with the change in its fit parameters q & T is shown in the Fig. 4.3. The results depict that with the change in the parameter T at fixed q, the Tsallis function rises up which matches with the observation in the BG distribution. Also, in the case where the q is varied at fixed T, the Tsallis function does not changes much in the low-p_{T} region, however it starts to diverge with larger q line above the smaller q. The unified distribution function (Eq. 4.35) consist of four parameters T, q, p_0 & n apart from the normalization parameter. The dependence of unified function on parameter q and T function is shown in the Fig. 4.4 and the plots shows a trend similar to what is observed in the Tsallis case. The parameter p_0 slightly effect the function and with the decrease in n the function shifts upwards.

In the Fig. 4.5, we have presented the variation of soft and hard part separately with the

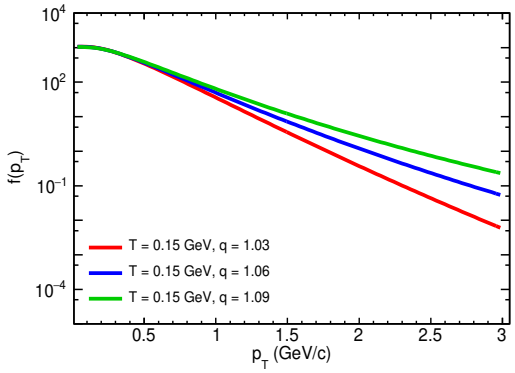

(a) variable q parameter.

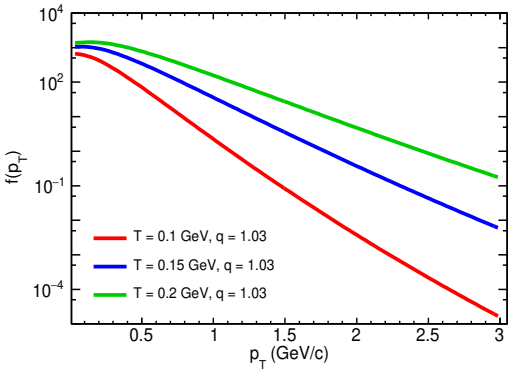

(b) variable T parameter.

Figure 4.3: The variation of Tsallis distribution function with a change in its parameters.

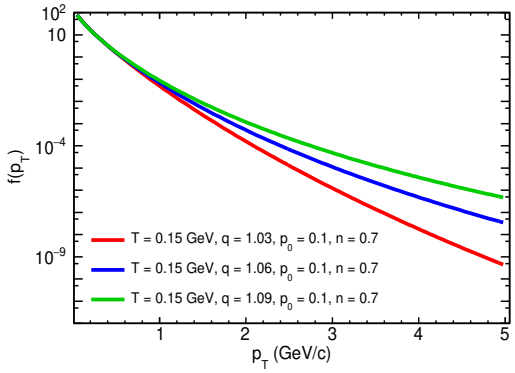

(a) variable q parameter.

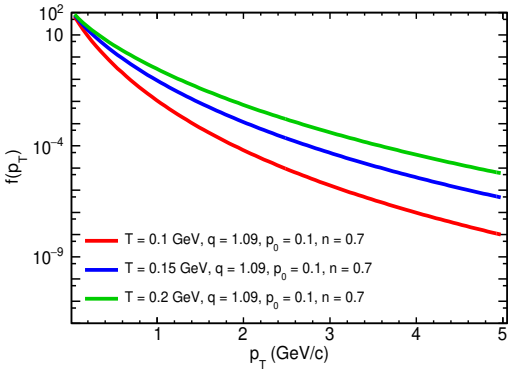

(b) variable T parameter.

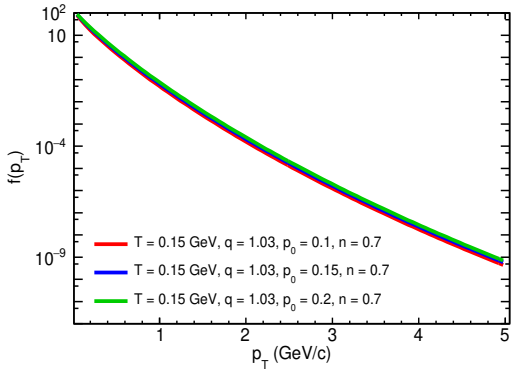

(c) variable p_0 parameter.

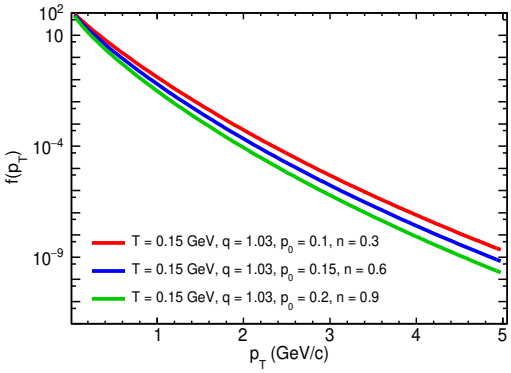

(d) variable n parameter.

Figure 4.4: The variation of unified distribution function with a change in its parameters.

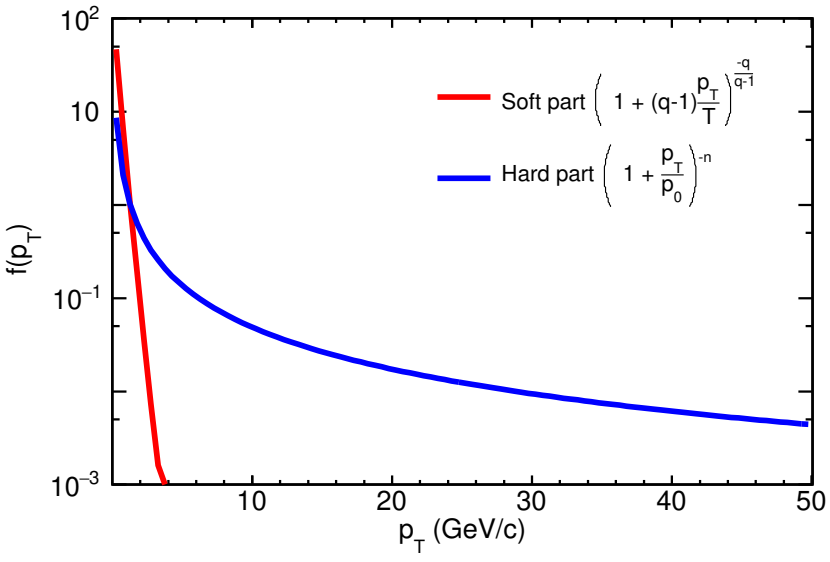

Figure 4.5: The variation soft and hard part of the unified function (Eq. 4.35) separately with the change in p_{T}.

increase in p_{T}. This plot depicts that the soft part of the spectra dominate in the low-p_{T} region and it rapidly decays down. After certain p_{T} value (in the range of $2-3$ GeV/c), the hard part becomes dominant and decays slowly with an increase in the p_{T}. From the behaviour of curves shown in the Fig. 4.5, we can infer that the first part of the unified equation (Eq. 4.35) takes care of the contribution of hard scattering processes in the high-p_{T} region whereas the second part of the Eq. (4.34) is same as the Tsallis equation and dominate in the low-p_{T} region. Hence, the unified formalism can be explained as an extension of Tsallis formalism to include the hard scattering processes in a unified manner.

4.6 Thermodynamical Consistency Check for the Unified statistical framework

The thermodynamical consistency is an important criterion that must be checked to validate if the statistical thermal model can be applied to the thermodynamical system. Following the first and second law of thermodynamics, we get the standard differential equations:

$$d\epsilon = Tds + \mu dn' \tag{4.43}$$

$$dP = sdT + n'd\mu \tag{4.44}$$

From the above two equations, taking the derivative with respect to different variables, we get the four thermodynamics relations Ref. [191]:

$$n' = \left.\frac{\partial P}{\partial \mu}\right|_{T} \tag{4.45}$$

$$T = \left.\frac{\partial \epsilon}{\partial s}\right|_{n'} \tag{4.46}$$

$$s = \left.\frac{\partial P}{\partial T}\right|_{\mu} \tag{4.47}$$

$$\mu = \left.\frac{\partial \epsilon}{\partial n'}\right|_{s} \tag{4.48}$$

The equations (4.45),(4.46), (4.47) & (4.48) must be satisfied to show that the developed statistical thermal model is thermodynamically consistent. For the Tsallis statistics, the consistency check is discussed in the previous chapter.

The equation of total number of particles and total energy remains same as in the case of Tsallis distribution:

$$\begin{aligned} N &= \sum_i f_i^q \\ E &= \sum_i f_i^q E_i \end{aligned} \tag{4.49}$$

In case of unified distribution

$$E\frac{d^3N}{dp^3} = B'\left(1+\frac{E}{p_0}\right)^{-n}\left(1+(q-1)\frac{(E-\mu)}{T}\right)^{-\frac{q}{q-1}} \tag{4.50}$$

$$\frac{d^3N}{dp^3} = \frac{B'}{E}\left(1+\frac{E}{p_0}\right)^{-n}\left(1+(q-1)\frac{(E-\mu)}{T}\right)^{-\frac{q}{q-1}} \tag{4.51}$$

We can simplify above equation to

$$\frac{d^3N}{dp^3} = B' f_E f_{Ta}^q \tag{4.52}$$

where

$$f_E = \frac{1}{E}\left(1+\frac{E}{p_0}\right)^{-n} \tag{4.53}$$

$$f_{Ta} = \left(1+(q-1)\frac{(E-\mu)}{T}\right)^{\frac{-1}{q-1}} \tag{4.54}$$

Hence, we have

$$\frac{d^3N}{dp^3} = \frac{V}{(2\pi)^3}\left\{(Bf_E)^{\frac{1}{q}}\, f_{Ta}\right\}^q \tag{4.55}$$

or more generally,

$$\frac{d^3N}{dp^3} = \frac{V}{(2\pi)^3} f_i^q \tag{4.56}$$

where

$$f_i = (Bf_E)^{\frac{1}{q}}\, f_{Ta} \tag{4.57}$$

The entropy for the unified distribution is given as:

$$S_p = \sum_i \left[\frac{qf_i}{(q-1)\,(Bf_E)^{\frac{1}{q}-1}} - \frac{f_i^q}{q-1}\right] \tag{4.58}$$

4.6.1 Relation 1 $\left\{\left.\frac{\partial P}{\partial \mu}\right|_T = n'\right\}$

For consistency check, we have to prove that:

$$\left.\frac{\partial P}{\partial \mu}\right|_T = n' \tag{4.59}$$

where n' is the number density. Using the first law of thermodynamics, we can express the pressure as:

$$P = \frac{-E + TS + \mu N}{V} \tag{4.60}$$

$$\left.\frac{\partial P}{\partial \mu}\right|_T = \frac{1}{V}\left[\frac{-\partial E}{\partial \mu} + T\frac{\partial S}{\partial \mu} + N + \mu\frac{\partial N}{\partial \mu}\right] \tag{4.61}$$

$$\begin{aligned}\left.\frac{\partial P}{\partial \mu}\right|_T = \frac{1}{V}\sum_i\Bigg[f_i^q - \frac{T}{q-1}\left\{1 + (q-1)\frac{(E_i-\mu)}{T}\right\}\frac{\partial f_i^q}{\partial \mu} \\ + \frac{Tq}{q-1}\frac{1}{(Bf_{E_i})^{\frac{1}{q}-1}}\frac{\partial f_i}{\partial \mu}\Bigg]\end{aligned} \tag{4.62}$$

$$f_i = (Bf_{E_i})^{\frac{1}{q}}\, f_{Ta_i} \tag{4.63}$$

$$\frac{\partial f_i}{\partial \mu} = \frac{(Bf_{E_i})^{\frac{1}{q}}}{T} f_{Ta_i}^q \tag{4.64}$$

$$\frac{\partial f_i^q}{\partial \mu} = Bq\frac{f_{E_i}}{T} f_{Ta_i}^{2q-1} \tag{4.65}$$

On substitution we will get,

$$\left.\frac{\partial P}{\partial \mu}\right|_T = \frac{1}{V}\sum_i f_i^q = \frac{N}{V} \tag{4.66}$$

$$\left.\frac{\partial P}{\partial \mu}\right|_T = n' \tag{4.67}$$

This proves that the relation Eq. (4.45) is valid for the unified framework.

4.6.2 Relation 2 $\left\{\left.\frac{\partial \epsilon}{\partial s}\right|_{n'} = T\right\}$

Next we try to prove equation relating the energy density with the temperature given as:

$$T = \left.\frac{\partial \epsilon}{\partial s}\right|_{n'} \tag{4.68}$$

The right hand side of this equation can be expanded as:

$$\left.\frac{\partial E}{\partial S}\right|_{n'} = \frac{\frac{\partial E}{\partial T}dT + \frac{\partial E}{\partial \mu}d\mu}{\frac{\partial S}{\partial T}dT + \frac{\partial S}{\partial \mu}d\mu} \tag{4.69}$$

$$\left.\frac{\partial E}{\partial S}\right|_{n'} = \frac{\frac{\partial E}{\partial T} + \frac{\partial E}{\partial \mu}\frac{d\mu}{dT}}{\frac{\partial S}{\partial T} + \frac{\partial S}{\partial \mu}\frac{d\mu}{dT}} \tag{4.70}$$

In this relation, n' is constant which add additional constraint given as:

$$dn' = \frac{\partial n'}{\partial T}dT + \frac{\partial n'}{\partial \mu}d\mu = 0 \tag{4.71}$$

$$\frac{d\mu}{dT} = -\frac{\frac{\partial n'}{\partial T}}{\frac{\partial n'}{\partial \mu}} \tag{4.72}$$

Solving for components of Eq. (4.70), we get:

$$\frac{\partial E}{\partial T} = \sum_i q f_i^{q-1} E_i \frac{\partial f_i}{\partial T} \tag{4.73}$$

$$\frac{\partial E}{\partial \mu} = \sum_i q f_i^{q-1} E_i \frac{\partial f_i}{\partial \mu} \tag{4.74}$$

$$\frac{\partial S}{\partial T} = \sum_i \left(\frac{q}{(q-1)\left(B f_{E_i}\right)^{\frac{1}{q}-1}} \frac{\partial f_i}{\partial T} - \frac{q f_i^{q-1}}{q-1}\frac{\partial f_i}{\partial T} \right) \tag{4.75}$$

$$\frac{\partial S}{\partial \mu} = \sum_i \left(\frac{q}{(q-1)\left(B f_{E_i}\right)^{\frac{1}{q}-1}} \frac{\partial f_i}{\partial \mu} - \frac{q f_i^{q-1}}{q-1} \frac{\partial f_i}{\partial \mu} \right) \tag{4.76}$$

$$\frac{\partial n'}{\partial T} = \frac{1}{V} \sum_i q f_i^{q-1} \frac{\partial f_i}{\partial T} \tag{4.77}$$

$$\frac{\partial n'}{\partial \mu} = \frac{1}{V} \sum_i q f_i^{q-1} \frac{\partial f_i}{\partial \mu} \tag{4.78}$$

Using the equations (4.73, 4.74, 4.77 & 4.78), numerator of the Eq. (4.70) reduces to:

$$\frac{\partial E}{\partial T} + \frac{\partial E}{\partial \mu} \frac{d\mu}{dT} = \sum_i q E_i f_i^{q-1} \frac{\partial f_i}{\partial T} - \frac{\sum\limits_{i,j} q^2 E_i (f_i f_j)^{q-1} \frac{\partial f_i}{\partial \mu} \frac{\partial f_j}{\partial T}}{\sum\limits_j q f_j^{q-1} \frac{\partial f_j}{\partial \mu}} \tag{4.79}$$

$$\frac{\partial E}{\partial T} + \frac{\partial E}{\partial \mu} \frac{d\mu}{dT} = \frac{\sum\limits_{i,j} q^2 E_i (f_i f_j)^{q-1} \frac{\partial f_i}{\partial T} \frac{\partial f_j}{\partial \mu} - \sum\limits_{i,j} q^2 E_i (f_i f_j)^{q-1} \frac{\partial f_i}{\partial \mu} \frac{\partial f_j}{\partial T}}{\sum\limits_j q f_j^{q-1} \frac{\partial f_j}{\partial \mu}} \tag{4.80}$$

This can be further reduced to

$$\frac{\partial E}{\partial T} + \frac{\partial E}{\partial \mu} \frac{d\mu}{dT} = \frac{\sum\limits_{i,j} q E_i (f_i f_j)^{q-1} C_{ij}}{\sum\limits_j f_j^{q-1} \frac{\partial f_j}{\partial \mu}} \tag{4.81}$$

where

$$C_{ij} = \frac{\partial f_i}{\partial T} \frac{\partial f_j}{\partial \mu} - \frac{\partial f_i}{\partial \mu} \frac{\partial f_j}{\partial T} \tag{4.82}$$

Using the equations (4.75, 4.76, 4.77 & 4.78) the denominator part of the Eq. (4.70) reduces to:

$$\begin{aligned} \frac{\partial S}{\partial T} + \frac{\partial S}{\partial \mu} \frac{d\mu}{dT} =& \sum_i \left(\frac{q}{(q-1)\left(B f_{E_i}\right)^{\frac{1}{q}-1}} \frac{\partial f_i}{\partial T} - \frac{q f_i^{q-1}}{q-1} \frac{\partial f_i}{\partial T} \right) - \\ & \left\{ \sum_i \frac{q}{(q-1)\left(B f_{E_i}\right)^{\frac{1}{q}-1}} \frac{\partial f_i}{\partial \mu} - \frac{q f_i^{q-1}}{q-1} \frac{\partial f_i}{\partial \mu} \right\} \frac{\frac{1}{V} \sum\limits_j q f_j^{q-1} \frac{\partial f_j}{\partial T}}{\frac{1}{V} \sum\limits_j q f_j^{q-1} \frac{\partial f_j}{\partial \mu}} \end{aligned} \tag{4.83}$$

$$\begin{aligned} = \frac{1}{\sum\limits_j f_j^{q-1} \frac{\partial f_j}{\partial \mu}} \Bigg[& \sum_{i,j} \left\{ \frac{q f_j^{q-1}}{(q-1)\left(B f_{E_i}\right)^{\frac{1}{q}-1}} \frac{\partial f_i}{\partial T} \frac{\partial f_j}{\partial \mu} - \frac{q (f_i f_j)^{q-1}}{q-1} \frac{\partial f_i}{\partial T} \frac{\partial f_j}{\partial \mu} \right\} \\ & - \sum_{i,j} \left\{ \frac{q f_j^{q-1}}{(q-1)\left(B f_{E_i}\right)^{\frac{1}{q}-1}} \frac{\partial f_i}{\partial \mu} \frac{\partial f_j}{\partial T} - \frac{q (f_i f_j)^{q-1}}{q-1} \frac{\partial f_i}{\partial \mu} \frac{\partial f_j}{\partial T} \right\} \Bigg] \end{aligned} \tag{4.84}$$

$$= \frac{1}{\sum_j f_j^{q-1}\frac{\partial f_j}{\partial \mu}} \sum_{i,j}\Bigg[\frac{q f_j^{q-1}}{(q-1)\left(B f_{E_i}\right)^{\frac{1}{q}-1}}\left\{\frac{\partial f_i}{\partial T}\frac{\partial f_j}{\partial \mu} - \frac{\partial f_i}{\partial \mu}\frac{\partial f_j}{\partial T}\right\} - \frac{q(f_i f_j)^{q-1}}{q-1}\left\{\frac{\partial f_i}{\partial T}\frac{\partial f_j}{\partial \mu} - \frac{\partial f_i}{\partial \mu}\frac{\partial f_j}{\partial T}\right\}\Bigg] \tag{4.85}$$

$$\frac{\partial S}{\partial T} + \frac{\partial S}{\partial \mu}\frac{d\mu}{dT} = \frac{\left\{\frac{q f_j^{q-1}}{(q-1)(B f_E)^{\frac{1}{q}-1}} - \frac{q(f_i f_j)^{q-1}}{q-1}\right\} C_{ij}}{\sum_j f_j^{q-1}\frac{\partial f_j}{\partial \mu}} \tag{4.86}$$

From Eq. (4.81) and (4.86) we get:

$$\frac{\partial E}{\partial S} = \frac{\sum_{i,j} q E_i (f_i f_j)^{q-1} C_{ij}}{\sum_{i,j}\left(\frac{q}{q-1}\right)\left[\frac{f_j^{q-1}}{(B f_{E_i})^{\frac{1}{q}-1}} - (f_i f_j)^{q-1}\right] C_{ij}} \tag{4.87}$$

$$\left.\frac{\partial E}{\partial S}\right|_{n'} = \frac{\sum_{i,j} q E_i (f_i f_j)^{q-1} C_{ij}}{\sum_{i,j}\left(\frac{q}{q-1}\right)\left[\frac{1}{f_i^{q-1}(B f_{E_i})^{\frac{1}{q}-1}} - 1\right](f_i f_j)^{q-1} C_{ij}} \tag{4.88}$$

$$\left.\frac{\partial E}{\partial S}\right|_{n'} = \frac{\sum_{i,j} q E_i (f_i f_j)^{q-1} C_{ij}}{\sum_{i,j}\left(\frac{q}{q-1}\right)\left[\frac{1}{(B f_{E_i})^{1-\frac{1}{q}} f_{Ta}^{q-1}(B f_{E_i})^{\frac{1}{q}-1}} - 1\right](f_i f_j)^{q-1} C_{ij}} \tag{4.89}$$

$$\left.\frac{\partial E}{\partial S}\right|_{n'} = \frac{\sum_{i,j} q E_i (f_i f_j)^{q-1} C_{ij}}{\sum_{i,j}\left(\frac{q}{q-1}\right)\left[1 + \frac{q-1}{T}(E_i - \mu) - 1\right](f_i f_j)^{q-1} C_{ij}} \tag{4.90}$$

$$\left.\frac{\partial E}{\partial S}\right|_{n'} = \frac{T\sum_{i,j} E_i (f_i f_j)^{q-1} C_{ij}}{\sum_{i,j}[E_i (f_i f_j)^{q-1} C_{ij} - \mu (f_i f_j)^{q-1} C_{ij}]} \tag{4.91}$$

But $\sum_{i,j} C_{ij} = 0$, $C_{ij} = -C_{ji}$ and also $(f_i f_j)^{q-1} = (f_j f_i)^{q-1}$. So term with μ in the denominator becomes zero and hence we get

$$\left.\frac{\partial \epsilon}{\partial s}\right|_{n'} = T \tag{4.92}$$

This shows that the second thermodynamic relation Eq. (4.46) is satisfied for the unified framework.

4.6.3 Relation 3 $\left\{ \left.\frac{\partial P}{\partial T}\right|_{\mu} = s \right\}$

The thermodynamic equation relating the pressure with the entropy density is given as:

$$\left.\frac{\partial P}{\partial T}\right|_{\mu} = s \tag{4.93}$$

Also,

$$\left.\frac{\partial P}{\partial T}\right|_{\mu} = \frac{1}{V}\Big[-\frac{\partial E}{\partial T} + S + T\frac{\partial S}{\partial T} + \mu\frac{\partial N}{\partial T}\Big] \tag{4.94}$$

So, in order to prove above relation, we have to basically prove that

$$-\frac{\partial E}{\partial T} + T\frac{\partial S}{\partial T} + \mu\frac{\partial N}{\partial T} = 0 \tag{4.95}$$

Expanding each term in the Eq. (4.95) separately,

$$\frac{\partial E}{\partial T} = \sum_i q f_i^{q-1} E_i \frac{\partial f_i}{\partial T} \tag{4.96}$$

$$\frac{\partial S}{\partial T} = \sum_i \Bigg(\frac{q}{(q-1)\left(B f_{E_i}\right)^{\frac{1}{q}-1}} \frac{\partial f_i}{\partial T} - \frac{q f_i^{q-1}}{q-1}\frac{\partial f_i}{\partial T} \Bigg) \tag{4.97}$$

$$\frac{\partial N}{\partial T} = \sum_i q f_i^{q-1} \frac{\partial f_i}{\partial T} \tag{4.98}$$

Putting it in Eq. (4.95) above we get

$$\begin{aligned} &-\frac{\partial E}{\partial T} + T\frac{\partial S}{\partial T} + \mu\frac{\partial N}{\partial T} = \\ &\sum_i \Big[-q f_i^{q-1} E_i \frac{\partial f_i}{\partial T} + \frac{Tq}{(q-1)\left(B f_{E_i}\right)^{\frac{1}{q}-1}} \frac{\partial f_i}{\partial T} - \frac{Tq f_i^{q-1}}{q-1}\frac{\partial f_i}{\partial T} + \mu q f_i^{q-1}\frac{\partial f_i}{\partial T} \Big] \end{aligned} \tag{4.99}$$

$$\begin{aligned} &-\frac{\partial E}{\partial T} + T\frac{\partial S}{\partial T} + \mu\frac{\partial N}{\partial T} = \\ &\sum_i \Big[-qE_i + \frac{Tq}{(q-1)\left(B f_{E_i}\right)^{\frac{1}{q}-1} f_i^{q-1}} - \frac{Tq}{q-1} + \mu q \Big] f_i^{q-1}\frac{\partial f_i}{\partial T} \end{aligned} \tag{4.100}$$

$$\begin{aligned} &-\frac{\partial E}{\partial T} + T\frac{\partial S}{\partial T} + \mu\frac{\partial N}{\partial T} = \\ &\sum_i \Big[-q\Big\{ (E_i - \mu) + \frac{T}{q-1} \Big\} + \frac{Tq}{(q-1) f_{Ta_i}^{q-1}} \Big] f_i^{q-1}\frac{\partial f_i}{\partial T} \end{aligned} \tag{4.101}$$

$$\sum_i \left[\frac{-qT}{q-1} \left\{ 1 + \frac{q-1}{T}(E_i - \mu) \right\} + \frac{qT}{q-1} \left\{ 1 + \frac{q-1}{T}(E_i - \mu) \right\}^{\frac{q-1}{q-1}} \right] f_i^{q-1} \frac{\partial f_i}{\partial T} = 0 \quad (4.102)$$

Hence

$$\left. \frac{\partial P}{\partial T} \right|_{\mu} = s \quad (4.103)$$

The derivation above presents the validity of thermodynamic relation Eq. (4.47) within the unified statistical framework.

4.6.4 Relation 4 $\left\{ \left. \frac{\partial \epsilon}{\partial n'} \right|_s = \mu \right\}$

The last thermodynamic relation provide the connection between the energy density and chemical potential and is given as:

$$\left. \frac{\partial \epsilon}{\partial n'} \right|_s = \mu \quad (4.104)$$

On expanding the left hand side of above equation:

$$\left. \frac{\partial E}{\partial N} \right|_s = \frac{\frac{\partial E}{\partial T} dT + \frac{\partial E}{\partial \mu} d\mu}{\frac{\partial N}{\partial T} dT + \frac{\partial N}{\partial \mu} d\mu} \quad (4.105)$$

$$\left. \frac{\partial E}{\partial N} \right|_s = \frac{\frac{\partial E}{\partial T} + \frac{\partial E}{\partial \mu} \frac{d\mu}{dT}}{\frac{\partial N}{\partial T} + \frac{\partial N}{\partial \mu} \frac{d\mu}{dT}} \quad (4.106)$$

Here s is constant so this will add an additional constraint given in the form of equation:

$$ds = \frac{\partial s}{\partial T} dT + \frac{\partial s}{\partial \mu} d\mu = 0 \quad (4.107)$$

Evaluating different terms in the right hand side of the Eq. (4.106):

$$\frac{d\mu}{dT} = -\frac{\frac{\partial s}{\partial T}}{\frac{\partial s}{\partial \mu}} \quad (4.108)$$

$$\frac{\partial E}{\partial T} = \sum_i q f_i^{q-1} E_i \frac{\partial f_i}{\partial T} \quad (4.109)$$

$$\frac{\partial E}{\partial \mu} = \sum_i q f_i^{q-1} E_i \frac{\partial f_i}{\partial \mu} \quad (4.110)$$

$$\frac{\partial s}{\partial T} = \frac{1}{V} \sum_i \left(\frac{q}{(q-1)\left(B f_{E_i}\right)^{\frac{1}{q}-1}} \frac{\partial f_i}{\partial T} - \frac{q f_i^{q-1}}{q-1} \frac{\partial f_i}{\partial T} \right) \quad (4.111)$$

$$\frac{\partial s}{\partial \mu} = \frac{1}{V}\sum_i \left(\frac{q}{(q-1)\left(Bf_{E_i}\right)^{\frac{1}{q}-1}} \frac{\partial f_i}{\partial \mu} - \frac{q f_i^{q-1}}{q-1}\frac{\partial f_i}{\partial \mu} \right) \tag{4.112}$$

$$\frac{\partial N}{\partial T} = \sum_i q f_i^{q-1} \frac{\partial f_i}{\partial T} \tag{4.113}$$

$$\frac{\partial N}{\partial \mu} = \sum_i q f_i^{q-1} \frac{\partial f_i}{\partial \mu} \tag{4.114}$$

Using the equations (4.108-4.114) we can simplify the numerator of Eq. (4.106) as follows,

$$\frac{\partial E}{\partial T} + \frac{\partial E}{\partial \mu}\frac{d\mu}{dT} = \sum_i q f_i^{q-1} E_i \frac{\partial f_i}{\partial T} - \frac{\sum_i q f_i^{q-1} E_i \frac{\partial f_i}{\partial \mu} \frac{1}{V} \sum_j \left(\frac{q}{(q-1)\left(Bf_{E_j}\right)^{\frac{1}{q}-1}} \frac{\partial f_j}{\partial T} - \frac{q f_j^{q-1}}{q-1}\frac{\partial f_j}{\partial T} \right)}{\frac{1}{V}\sum_j \frac{q}{(q-1)\left(Bf_{E_j}\right)^{\frac{1}{q}-1}} \frac{\partial f_j}{\partial \mu} - \frac{q f_j^{q-1}}{q-1}\frac{\partial f_j}{\partial \mu}} \tag{4.115}$$

$$= \frac{\sum_{i,j} \frac{q E_i f_i^{q-1}}{\left(Bf_{E_j}\right)^{\frac{1}{q}-1}} \frac{\partial f_i}{\partial T}\frac{\partial f_j}{\partial \mu} - \sum_{i,j} q E_i (f_i f_j)^{q-1} \frac{\partial f_i}{\partial T}\frac{\partial f_j}{\partial \mu} - \sum_{i,j} \frac{q E_i f_i^{q-1}}{\left(Bf_{E_j}\right)^{\frac{1}{q}-1}} \frac{\partial f_i}{\partial \mu}\frac{\partial f_j}{\partial T} + \sum_{i,j} q E_i (f_i f_j)^{q-1} \frac{\partial f_i}{\partial \mu}\frac{\partial f_j}{\partial T}}{\sum_j \frac{1}{\left(Bf_{E_j}\right)^{\frac{1}{q}-1}} \frac{\partial f_j}{\partial \mu} - f_j^{q-1}\frac{\partial f_j}{\partial \mu}} \tag{4.116}$$

$$= \frac{1}{\sum_j \frac{1}{\left(Bf_{E_j}\right)^{\frac{1}{q}-1}} \frac{\partial f_j}{\partial \mu} - f_j^{q-1}\frac{\partial f_j}{\partial \mu}} \sum_{i,j} \left[\frac{q E_i f_i^{q-1}}{\left(Bf_{E_j}\right)^{\frac{1}{q}-1}} \left\{ \frac{\partial f_i}{\partial T}\frac{\partial f_j}{\partial \mu} - \frac{\partial f_i}{\partial \mu}\frac{\partial f_j}{\partial T} \right\} - \right. \tag{4.117}$$

$$\left. q E_i (f_i f_j)^{q-1} \left\{ \frac{\partial f_i}{\partial T}\frac{\partial f_j}{\partial \mu} - \frac{\partial f_i}{\partial \mu}\frac{\partial f_j}{\partial T} \right\} \right]$$

$$= \frac{\sum_{i,j} \left(\frac{q E_i f_i^{q-1}}{\left(Bf_{E_j}\right)^{\frac{1}{q}-1}} - q E_i (f_i f_j)^{q-1} \right) C_{ij}}{\sum_j \left(\frac{1}{\left(Bf_{E_j}\right)^{\frac{1}{q}-1}} \frac{\partial f_j}{\partial \mu} - f_j^{q-1}\frac{\partial f_j}{\partial \mu} \right)} \tag{4.118}$$

Similarly, the denominator of Eq. (4.106) reduces to:

$$\frac{\partial N}{\partial T} + \frac{\partial N}{\partial \mu}\frac{d\mu}{dT} = \frac{\sum_{i,j} \left(\frac{q f_i^{q-1}}{\left(Bf_{E_j}\right)^{\frac{1}{q}-1}} - q (f_i f_j)^{q-1} \right) C_{ij}}{\sum_j \left(\frac{1}{\left(Bf_{E_j}\right)^{\frac{1}{q}-1}} \frac{\partial f_j}{\partial \mu} - f_j^{q-1}\frac{\partial f_j}{\partial \mu} \right)} \tag{4.119}$$

On dividing we get

$$\frac{\frac{\partial E}{\partial T} + \frac{\partial E}{\partial \mu}\frac{d\mu}{dT}}{\frac{\partial N}{\partial T} + \frac{\partial N}{\partial \mu}\frac{d\mu}{dT}} = \frac{\sum_{i,j} \left(\frac{q E_i f_i^{q-1}}{\left(Bf_{E_j}\right)^{\frac{1}{q}-1}} - q E_i (f_i f_j)^{q-1} \right) C_{ij}}{\sum_{i,j} \left(\frac{q f_i^{q-1}}{\left(Bf_{E_j}\right)^{\frac{1}{q}-1}} - q (f_i f_j)^{q-1} \right) C_{ij}} \tag{4.120}$$

$$= \frac{\sum_{i,j} qE_i \left(\frac{1}{\left(Bf_{E_j}\right)^{\frac{1}{q}-1} f_j^{q-1}} - 1 \right) (f_i f_j)^{q-1} C_{ij}}{\sum_{i,j} q \left(\frac{1}{\left(Bf_{E_j}\right)^{\frac{1}{q}-1} f_j^{q-1}} - 1 \right) (f_i f_j)^{q-1} C_{ij}} \tag{4.121}$$

$$= \frac{\sum_{i,j} E_i [1 + \frac{(q-1)(E_j-\mu)}{T} - 1](f_i f_j)^{q-1} C_{ij}}{\sum_{i,j} [1 + \frac{(q-1)(E_j-\mu)}{T} - 1](f_i f_j)^{q-1} C_{ij}} \tag{4.122}$$

$$\frac{\sum_{i,j} E_i E_j (f_i f_j)^{q-1} C_{ij} - \sum_{i,j} E_i \mu (f_i f_j)^{q-1} C_{ij}}{\sum_{i,j} E_j (f_i f_j)^{q-1} C_{ij} - \sum_{i,j} \mu (f_i f_j)^{q-1} C_{ij}} \tag{4.123}$$

First term in numerator and second term in denominator is zero. So on simplifying we get

$$\left. \frac{\partial \epsilon}{\partial n'} \right|_s = \mu \tag{4.124}$$

The calculations provided above clearly shows that the unified formalism and the corresponding entropy Eq. (4.58) is thermodynamically consistent.

4.7 Summary

Most of the models used to fit the transverse momentum spectra lacks a unified description. Although, we can use a simple polynomial function, however it lacks a physics explanation so, in this chapter, we have discussed a unified model based on Pearson probability distribution to study broader range of p_{T}-spectra. Some of the key features of the unified model are:

- It nicely incorporates the physics of soft processes and hard scattering process.
- It is thermodynamically consistent as it obeys standard laws of thermodynamics.
- It is backward compatible to the Tsallis and BG distribution.

The results obtained by analyzing the spectra at different energies and for different collision system using the unified formalism is discussed in the next chapter.

Chapter 5

Transverse Momentum Spectra in Unified Statistical Framework

This chapter gives a detailed discussion, validation & test of the unified model using real data taken in various experiments. We will show the results obtained by fitting unified distribution to the p_{T}-spectra data over a wide range of energies and centralities. We will also present a comparison with other models used to explain the p_{T}-spectra.

We have tested the formalism over a broad energy range, centrality and for different collision system. The data used in this analysis includes the transverse momentum spectra of charged hadrons produced in different centrality $PbPb$ collision at 2.76 TeV [16], 5.02 TeV [17] and $XeXe$ collision at 5.44 TeV [6] measured by the ALICE experiment. We have also used the spectra of identified hadron (π^+) produced in $AuAu$ collision at 19.6 GeV [9], 27 GeV [9] & 39 GeV [9] measured by STAR experiment at RHIC, 130 GeV [10] & 200 GeV [11] measured by the PHENIX experiment and $PbPb$ collision at 2.76 TeV [20] measured by ALICE experiment. To test the applicability of formalism over different collision system, apart from the heavy-ion collision we have also used the charged hadron spectra produced in pp collision at 900 GeV [26], 2.76 TeV [27], 5.02 TeV [28] & 7 TeV [26] measured by the CMS experiment. Recently released multiplicity divided data for charged hadron spectra produced in pp collision at 7 TeV [29] measured by ALICE experiment is also considered in the study. All the data discussed above are publicly available and we have downloaded it from the high energy physics data repository named 'HEPData' and other repositories. Different data discussed above are measured in different rapidity window and the detail is provided in the table 5.1. The ROOT [218] data analysis

Table 5.1: Description of the datasets used in the study

Energy	Collision System	p_{T} range (GeV/c)	Experimental cuts	Experiment
19.6 GeV	$AuAu$	0-2	$\|y\| < 0.1$, PID: π^+	STAR [9]
27 GeV	$AuAu$	0-2	$\|y\| < 0.1$, PID: π^+	STAR [9]
39 GeV	$AuAu$	0-2	$\|y\| < 0.1$, PID: π^+	STAR [9]
130 GeV	$AuAu$	0-2.3	$\|y\| < 0.5$, PID: π^+	PHENIX [10]
200 GeV	$AuAu$	0-3	$\|y\| < 0.5$, PID: π^+	PHENIX [11]
2.76 TeV	$PbPb$	0-3	$\|y\| < 0.5$, PID: π^+	ALICE [20]
2.76 TeV	$PbPb$	0-5	$\|\eta\| < 0.8$, Charge X	ALICE [16]
5.02 TeV	$PbPb$	0-5	$\|\eta\| < 0.8$, Charge X	ALICE [17]
5.44 TeV	$XeXe$	0-5	$\|\eta\| < 0.8$, Charge X	ALICE [6]
900 GeV	pp	0-37.2	$\|\eta\| < 2.4$, Charge X	CMS [26]
2.76 TeV	pp	0-112.2	$\|\eta\| < 1.0$, Charge X	CMS [27]
5.02 TeV	pp	0-400	$\|\eta\| < 1.0$, Charge X	CMS [28]
7 TeV	pp	0-201.2	$\|\eta\| < 2.4$, Charge X	CMS [26]
7 TeV	pp	0-40	$\|\eta\| < 0.5$, Charge X	ALICE [29]

framework along with the MINUIT [219] algorithm is used to perform the fitting of spectra using different functions.

5.1 Analysis of the Spectra

We have first analyzed the data of the transverse momentum spectra of charged hadrons produced in the 2.76 TeV $PbPb$ collision at different centralities [16] measured by the ALICE experiment. Figures 5.1, 5.2 & 5.3 present the fit to the data using the BG, Tsallis and unified distribution function respectively. From Fig. 5.1 we can conclude that the BG distribution function is not in good agreement with the experimental data. The Tsallis function, as shown in Fig. 5.2, shows a better fit to the data but only in the intermediate p_{T} range, it starts to deviate at very low- and high-p_{T} . The best fit is obtained using the unified distribution function, shown in the Fig. 5.3. The goodness of a fit function, i.e., how close a fit function to the experimental data, is quantified using the χ^2/NDF values. In table 5.2, the χ^2/NDF for different centralities have been provided. The corresponding value of the fit parameters obtained by fitting the BG, Tsallis and unified function is provided in the table 5.3. From the table 5.2 we can conclude that the best fit is obtained for the unified distribution, which complements the observation from Fig. 5.3.

From the statistical point of view, better fit using the unified distribution can be attributed to the presence of higher-order moments as the free parameters because, in other distribu-

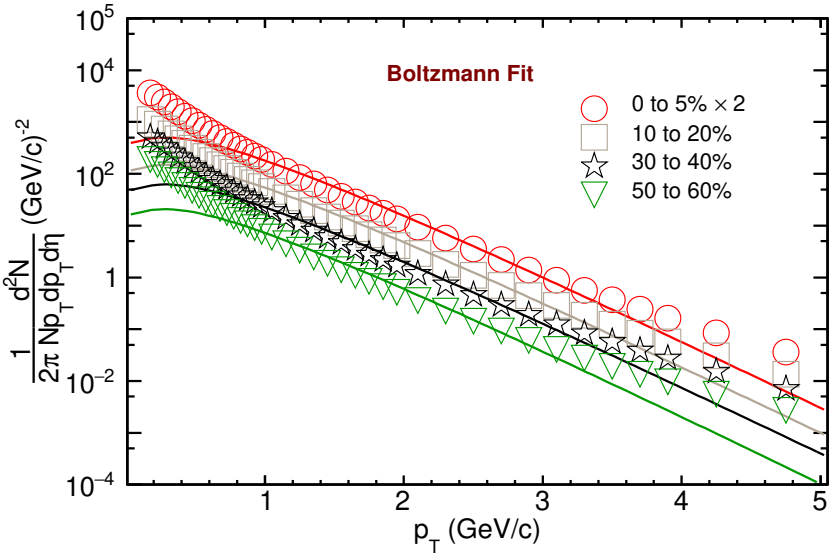

Figure 5.1: BG distribution fit of charged particle p_{T}-spectra produced in $PbPb$ collision for four different centrality bins at 2.76 TeV measured in ALICE experiment [16] at LHC.

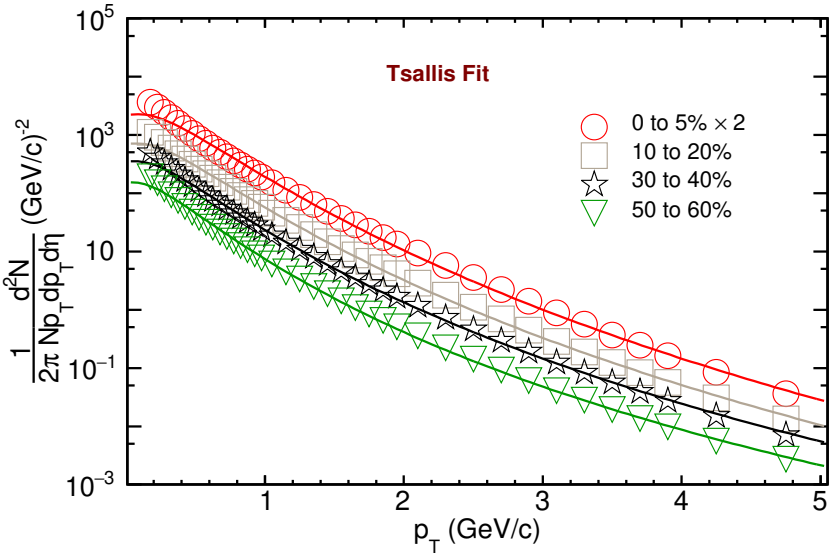

Figure 5.2: Tsallis fit of charged particle p_{T}-spectra produced in $PbPb$ collision for four different centrality bins at 2.76 TeV measured in ALICE experiment [16] at LHC.

tion, we mainly use the mean and standard deviation as the fitting parameter. As shown in Fig. 5.2, the Tsallis function starts to deviate from the experimental data at higher p_{T} values suggesting that the Tsallis function is unable to fit the tail of the distribution and the presence of additional parameter may resolve the issue. The unified function nicely fits the distribution as shown in Fig. 5.3. From the successful fitting of unified distribution, it can be inferred that the tail part depends on the higher moments. Thus any function with higher order moment as free parameter would nicely fit the data. Having such free parameters in

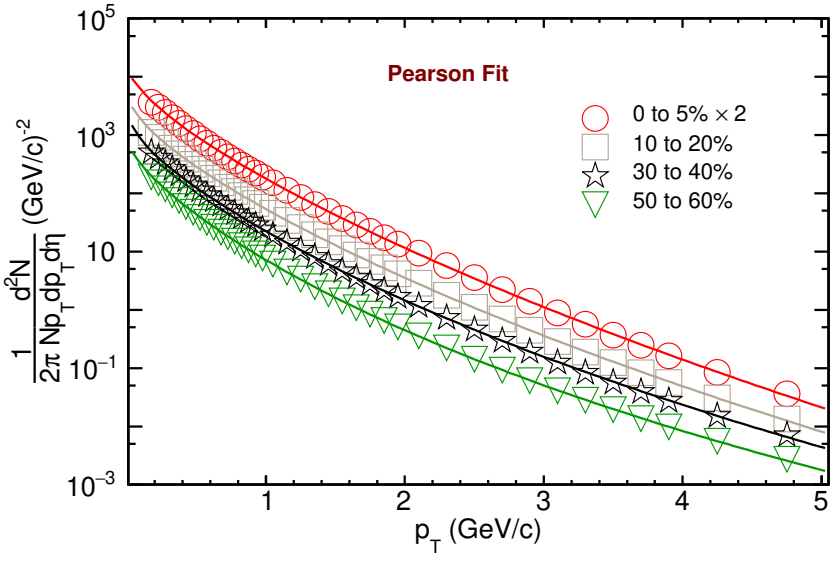

Figure 5.3: Pearson fit of charged particle p_{T}-spectra produced in $PbPb$ collision for four different centrality bins at 2.76 TeV measured in ALICE experiment [16] at LHC.

Table 5.2: Best fit value of χ^2/NDF for different centrality bins

Centrality	BG	Tsallis	Unified
0 to 5%	25.3451	1.99445	0.10100
5 to 10%	25.5971	1.86747	0.08545
10 to 20%	26.5224	1.75271	0.08609
20 to 30%	27.6911	1.57784	0.08423
30 to 40%	28.3606	1.34457	0.06994
40 to 50%	29.8191	1.1226	0.05170
50 to 60%	29.4844	0.88907	0.03901
60 to 70%	27.9139	0.65552	0.02568

the model is an extra advantage as far as fitting is concerned and unified model offers extra parameter as compared to earlier models yet standing through the thermal test.

Upon careful observation of the best fit value of parameters, we observe that the numerical value of parameter n is of the order 10^{-1}, whereas the value of non-extensivity parameter q is close to unity. This set of numerical values point towards a rapid decay of the Tsallis part of Eq. (4.34) and a slow decay of the hard scattering part. This further supports that in unified distribution, the contribution of the first part of the Eq. (4.34), which corresponds to the spectra of particles produced in hard scattering processes, is dominant at higher p_{T} values.

Although, multi-component models fit the data separately, but miss a unified explanation of the particles produced in the collision. Thus, the formalism developed based on the Pearson probability distribution can be considered a better explanation to the experimental

Table 5.3: Numerical values of the parameters obtained by fitting the experimental data of p_{T}-spectra fitted with the BG, Tsallis and unified function.

Centrality	**BG**	**Tsallis**		**Unified**			
	T	T	q	T	q	p_0	n
0-5%	0.317 $\pm$0.003	0.163 $\pm$0.004	1.095 $\pm$0.003	0.393 $\pm$0.038	1.048 $\pm$0.003	0.105 $\pm$0.207	0.749 $\pm$0.348
5-10%	0.318 $\pm$0.003	0.161 $\pm$0.004	1.098 $\pm$0.003	0.386 $\pm$0.041	1.053 $\pm$0.003	0.088 $\pm$0.191	0.700 $\pm$0.319
10-20%	0.319 $\pm$0.003	0.158 $\pm$0.004	1.101 $\pm$0.003	0.370 $\pm$0.069	1.060 $\pm$0.006	0.060 $\pm$0.179	0.619 $\pm$0.302
20-30%	0.320 $\pm$0.003	0.152 $\pm$0.004	1.106 $\pm$0.003	0.352 $\pm$0.079	1.070 $\pm$0.008	0.038 $\pm$0.180	0.548 $\pm$0.295
30-40%	0.318 $\pm$0.003	0.146 $\pm$0.004	1.112 $\pm$0.003	0.330 $\pm$0.071	1.081 $\pm$0.008	0.026 $\pm$0.197	0.489 $\pm$0.343
40-50%	0.316 $\pm$0.004	0.137 $\pm$0.004	1.119 $\pm$0.003	0.311 $\pm$0.077	1.094 $\pm$0.008	0.034 $\pm$0.248	0.474 $\pm$0.461
50-60%	0.313 $\pm$0.004	0.128 $\pm$0.004	1.125 $\pm$0.003	0.292 $\pm$0.079	1.106 $\pm$0.008	0.046 $\pm$0.317	0.468 $\pm$0.608
60-70%	0.308 $\pm$0.005	0.119 $\pm$0.004	1.132 $\pm$0.003	0.273 $\pm$0.108	1.121 $\pm$0.011	0.075 $\pm$0.487	0.487 $\pm$1.034

data. Moreover, the unified statistical framework is thermodynamically consistent and it also reduces to the Tsallis and the BG distributions under different limits on its parameters and it nicely explains the data over a broad p_{T} range.

From the results presented above, we observe that the unified formalism provides a better explanation of charged hadrons spectra produced in 2.76 TeV $PbPb$ collision. To further strengthen our approach, we also performed a similar comparative study over different energies ranging from 19.6 GeV to 2.76 TeV.

5.1.1 Energy Dependent Study

We have analyzed the transverse momentum spectra of positive pions over a broad energy range. The collision data selected for this study includes the $AuAu$ collision at 19.6 GeV, 27 GeV, 39 GeV, 130 GeV, $\&$ 200 GeV measured by the RHIC experiment, and the $PbPb$ collision data at 2.76 TeV measured by the ALICE experiment at LHC. A table including the χ^2/NDF values representing the goodness of fit of BG, Tsallis and unified functions fitted to p_{T}-spectra at several energies is given in table 5.4.

In Fig. 5.4, we have provided the BG, Tsallis and unified fit the transverse momentum spectra at different energies. We observe that the unified formalism provide the best expla-

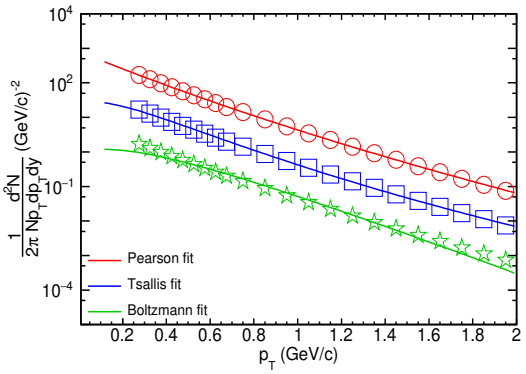

(a) 19.6 GeV measured in STAR experiment [9] at RHIC

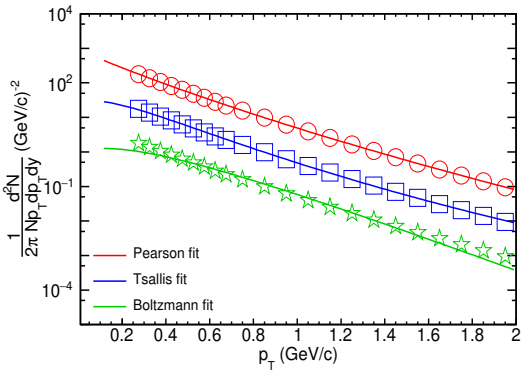

(b) 27 GeV measured in STAR experiment [9] at RHIC

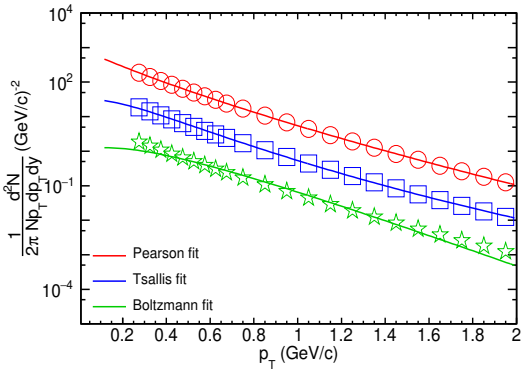

(c) 39 GeV measured in STAR experiment [9] at RHIC

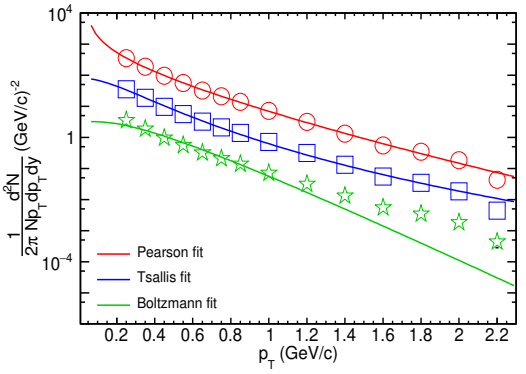

(d) 130 GeV measured in PHENIX experiment [10] at RHIC

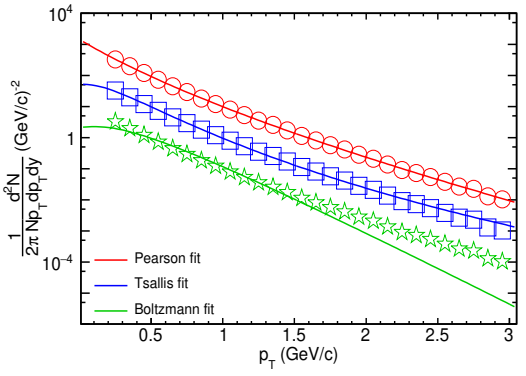

(e) 200 GeV measured in PHENIX experiment [11] at RHIC

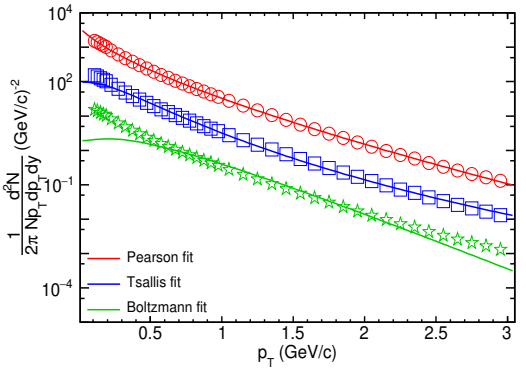

(f) 2.76 TeV measured in ALICE experiment [20] at LHC

Figure 5.4: The Boltzmann, Tsallis and unified function fit to the transverse momentum data of π^+ particles produced at different collision energies. Data points are scaled for clear presentation.

Table 5.4: The χ^2/NDF values of transverse momentum data of π^+ particles fitted to Boltzmann, Tsallis and unified functions at various collision energies is given along with the fitted value of Temperature and q parameter for unified distribution.

Collision energy (GeV)	χ^2/NDF Boltzmann	χ^2/NDF Tsallis	χ^2/NDF Unified	T (MeV)	q
19.6	9.7695	0.3916	0.05225	181.087	1.04675
27	9.9343	0.3163	0.03979	195.473	1.04482
39	10.2994	0.27538	0.002487	243.247	1.03941
130	45.747	5.11838	1.91187	268.51	1.03346
200	337.676	14.5667	1.7977	422.745	1.01778
2760	23.9804	2.31356	0.06369	381.422	1.03301

nation to the data over a wide energy range.

5.2 Model Comparison

This section presents a comparative study of the application of different distribution functions used to explain the p_{T}-spectra. We analyze the charged hadron spectra produced in 2.76 and 5.02 TeV $PbPb$ collision and study the χ^2/NDF values to determine which distribution provides best fit to the experimental data [220]. As discussed in the chapter 3, different models developed to study transverse momentum spectra have different types of physics explanation. For example, the BG distribution function is a purely thermal description of the spectra, whereas Tsallis is a generalization of BG approach to include a non-extensive system. BW and TBW are hydrodynamically inspired models that also include flow effects and q-Weibull distribution takes into account hard QCD processes. On the other hand, unified distribution is a generalized form that takes into account hard QCD process as well as non-extensivity in the system. In our preliminary check, we found that the unified model has a direct connection to second-order flow coefficient v_2.

In Fig. 5.5 & 5.6, the results obtained by fitting different phenomenological models to the charged hadron spectra produced in 2.76 TeV and 5.02 TeV $PbPb$ collision are presented. We have performed this analysis for different centrality classes ranging from most central collision $(0-5\%)$ to most peripheral $(70-80\%)$ centrality. The corresponding best fit values for different free parameters is presented in the tables 5.5, 5.6 & 5.7. The variation of parameter q and the χ^2/NDF values with centrality for different models is shown in figures 5.7, 5.8, 5.9 $\&$ 5.10.

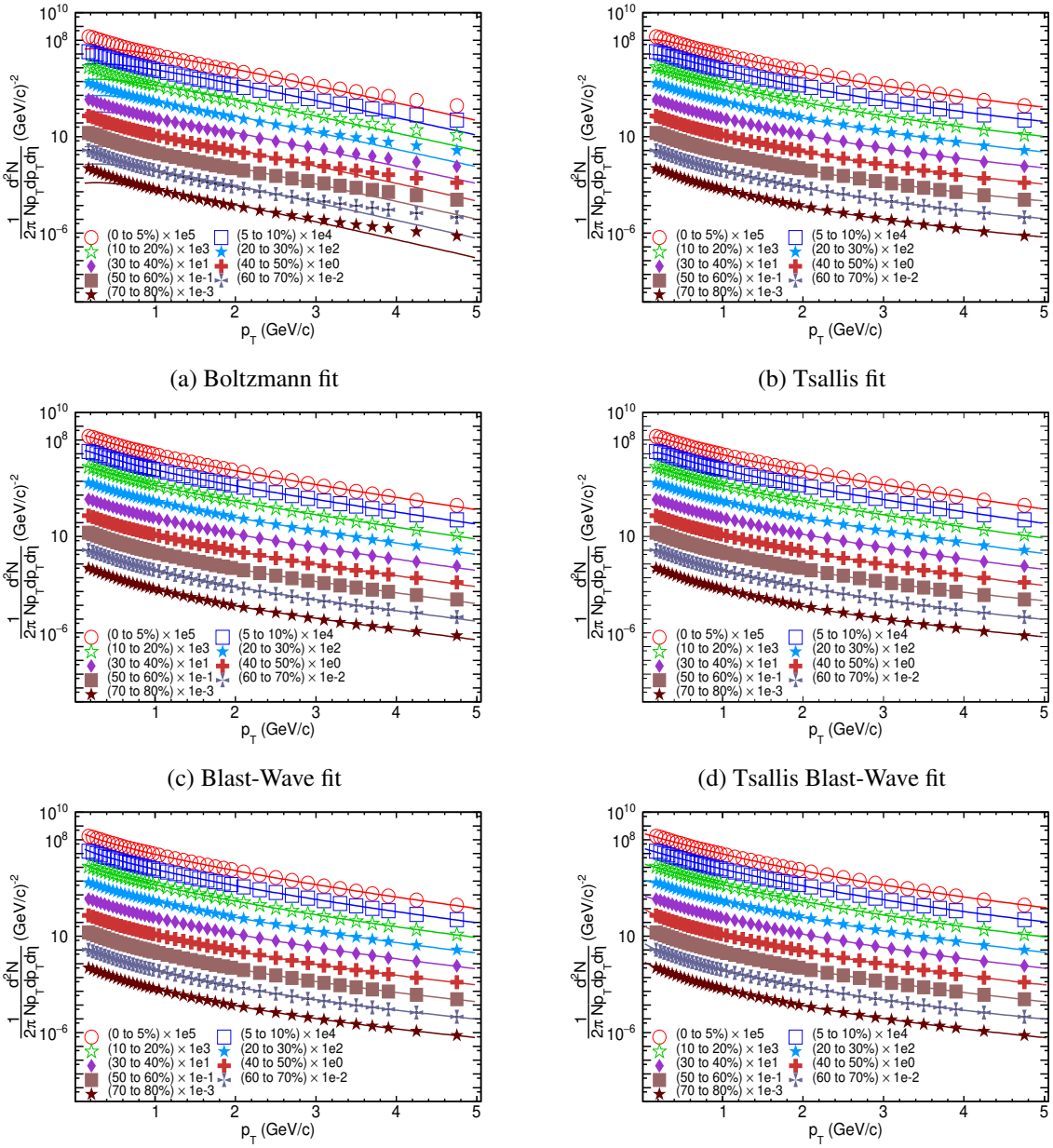

(a) Boltzmann fit

(b) Tsallis fit

(c) Blast-Wave fit

(d) Tsallis Blast-Wave fit

(e) q-Weibull fit

(f) Unified function fit

Figure 5.5: The transverse momentum data of charged hadrons produced at different centralities of $PbPb$ collision at $\sqrt{s_{NN}} = 2.76$ TeV [16] measured by the ALICE experiment fitted with different fitting functions.

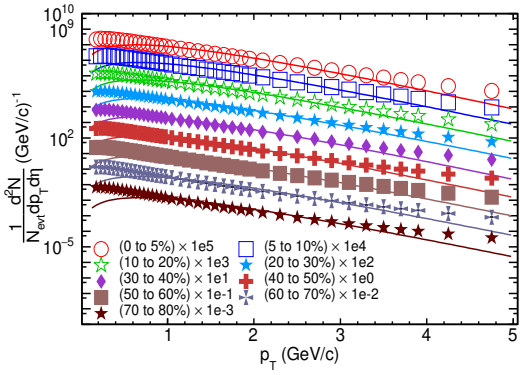

(a) Boltzmann fit

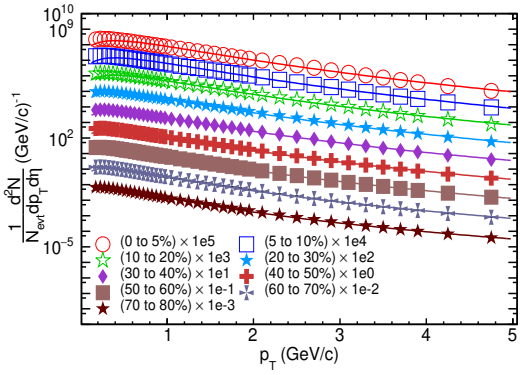

(b) Tsallis fit

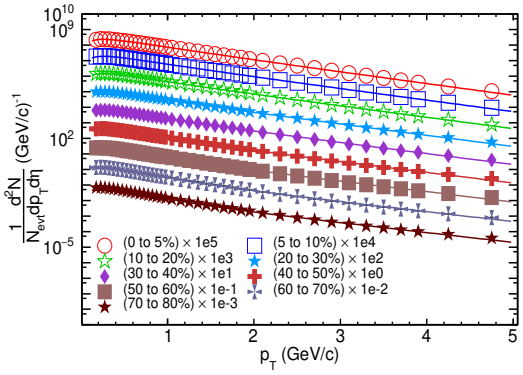

(c) Blast-Wave fit

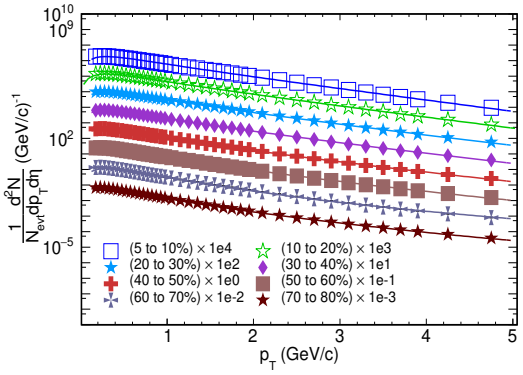

(d) Tsallis Blast-Wave fit

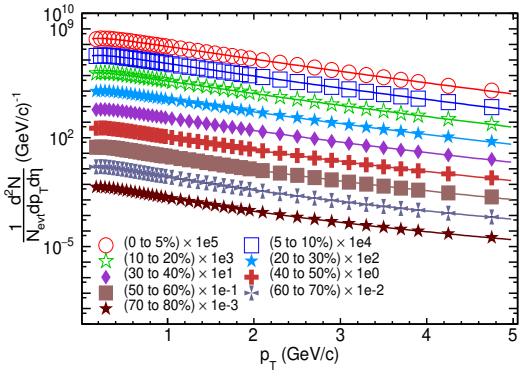

(e) q-Weibull fit

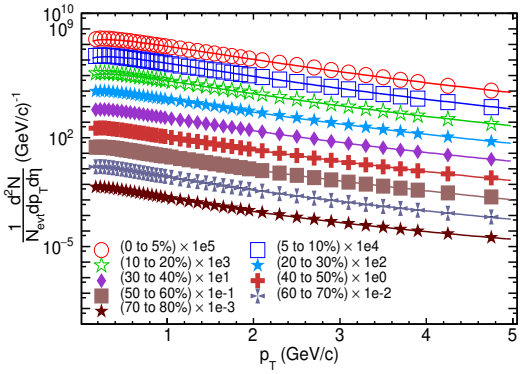

(f) Unified function fit

Figure 5.6: The transverse momentum data of charged hadrons produced at different centralities of $PbPb$ collision at $\sqrt{s_{NN}} = 5.02$ TeV [17] measured by the ALICE experiment fitted with different fitting functions.

Table 5.5: Table of parameter values obtained after fitting charged hadron spectra at 3 different centralities with different functions

Variable	Method	Energy (TeV)	0 to 5%	40 to 50%	70 to 80%
T_{eff}(MeV)	BG	2.76	316.95	316.30	305.23
		5.02	319.75	330.97	338.52
	Tsallis	2.76	163	137.52	111.22
		5.02	176.10	148.43	117.75
	Pearson	2.76	393.54	311.34	296.08
		5.02	407.45	369.10	329.40
T_{kin}(MeV)	BW	2.76	124.25	163.18	157.73
		5.02	113.57	157.64	164.25
	TBW	2.76	76.98	52.01	21.14
		5.02	–	76.29	44.36
q	Tsallis	2.76	1.095	1.119	1.138
		5.02	1.097	1.120	1.142
	TBW	2.76	1.014	1.055	1.097
		5.02	–	1.047	1.086
	$q-weibull$	2.76	1.021	1.061	1.091
		5.02	1.003	1.047	1.085
	Pearson	2.76	1.048	1.094	1.133
		5.02	1.048	1.085	1.131
χ^2/NDF	BG	2.76	25.34	29.82	24.09
		5.02	396.78	735.27	1080.25
	$Tsallis$	2.76	1.99	1.13	0.51
		5.02	34.30	36.37	23.62
	BW	2.76	0.29	0.60	0.53
		5.02	2.09	12.05	20.65
	TBW	2.76	0.67	0.52	0.35
		5.02	–	4.75	1.74
	$q-weibull$	2.76	0.11	0.06	0.02
		5.02	1.42	2.19	1.16
	Pearson	2.76	0.10	0.05	0.02
		5.02	1.71	1.96	1.09

Table 5.6: The best fit value of exponent 'w' and average transverse flow velocity obtained by fitting the charged hadron transverse momentum spectra using BW and TBW models.

Centrality	w (BW)		$\langle\beta_T\rangle$ (BW)		$\langle\beta_T\rangle$ (TBW)	
	2.76 TeV	5.02 TeV	2.76 TeV	5.02 TeV	2.76 TeV	5.02 TeV
0 to 5 %	1.2633 $\pm$0.7737	0.9471 $\pm$0.1236	0.5544 $\pm$0.1442	0.6303 $\pm$0.0291	0.4241 $\pm$0.0048	- -
5 to 10 %	1.3660 $\pm$0.6137	0.9538 $\pm$0.1322	0.534 $\pm$0.1059	0.6316 $\pm$0.0308	0.4244 $\pm$0.0048	0.4181 $\pm$0.0014
10 to 20 %	1.5316 $\pm$1.6441	0.9740 $\pm$0.1465	0.5047 $\pm$0.2528	0.6302 $\pm$0.0334	0.4247 $\pm$0.0052	0.4192 $\pm$0.0013
20 to 30 %	1.8038 $\pm$0.5546	1.1591 $\pm$0.1704	0.4642 $\pm$0.0714	0.5862 $\pm$0.0338	0.4254 $\pm$0.0052	0.4186 $\pm$0.0014
30 to 40 %	2.1756 $\pm$0.4673	1.4738 $\pm$0.2004	0.4199 $\pm$0.0487	0.5225 $\pm$0.0319	0.4263 $\pm$0.0054	0.4199 $\pm$0.0012
40 to 50 %	2.6499 $\pm$0.4699	1.9766 $\pm$0.0814	0.3771 $\pm$0.0389	0.4479 $\pm$0.0095	0.4281 $\pm$0.0048	0.4189 $\pm$0.0014
50 to 60 %	3.1212 $\pm$0.4993	2.4192 $\pm$0.0799	0.3446 $\pm$0.0341	0.4033 $\pm$0.0075	0.4305 $\pm$0.0051	0.4200 $\pm$0.0016
60 to 70 %	3.6574 $\pm$0.5502	3.2153 $\pm$0.0877	0.3149 $\pm$0.0309	0.3424 $\pm$0.0054	0.4330 $\pm$0.0052	0.4209 $\pm$0.0016
70 to 80 %	3.9250 $\pm$0.5907	3.4730 $\pm$0.0797	0.3041 $\pm$0.0305	0.3301 $\pm$0.0048	0.4355 $\pm$0.0083	0.4257 $\pm$0.0013

Table 5.7: The best fit value of parameters k and λ obtained by fitting the charged hadron transverse momentum spectra using q-Weibull model.

Centrality	k		λ	
	2.76 TeV	5.02 TeV	2.76 TeV	5.02 TeV
0 to 5 %	0.8183 ± 0.0481	0.7666 ± 0.0127	0.1953 ± 0.0170	0.1974 ± 0.0049
5 to 10 %	0.8218 ± 0.0493	0.7741 ± 0.0132	0.1949 ± 0.0172	0.1988 ± 0.0049
10 to 20 %	0.8297 ± 0.0503	0.7788 ± 0.0118	0.1940 ± 0.0172	0.1972 ± 0.0044
20 to 30 %	0.8407 ± 0.0520	0.7998 ± 0.0115	0.1910 ± 0.0171	0.1968 ± 0.0040
30 to 40 %	0.8545 ± 0.0546	0.8035 ± 0.0110	0.1865 ± 0.0172	0.1894 ± 0.0037
40 to 50 %	0.8684 ± 0.0574	0.8295 ± 0.0111	0.1791 ± 0.0171	0.1853 ± 0.0035
50 to 60 %	0.8816 ± 0.0621	0.8492 ± 0.0119	0.1703 ± 0.0175	0.1772 ± 0.0035
60 to 70 %	0.8971 ± 0.0690	0.8717 ± 0.0156	0.1611 ± 0.0182	0.1678 ± 0.0032
70 to 80 %	0.8909 ± 0.0783	0.8662 ± 0.0123	0.1489 ± 0.0197	0.1536 ± 0.0033

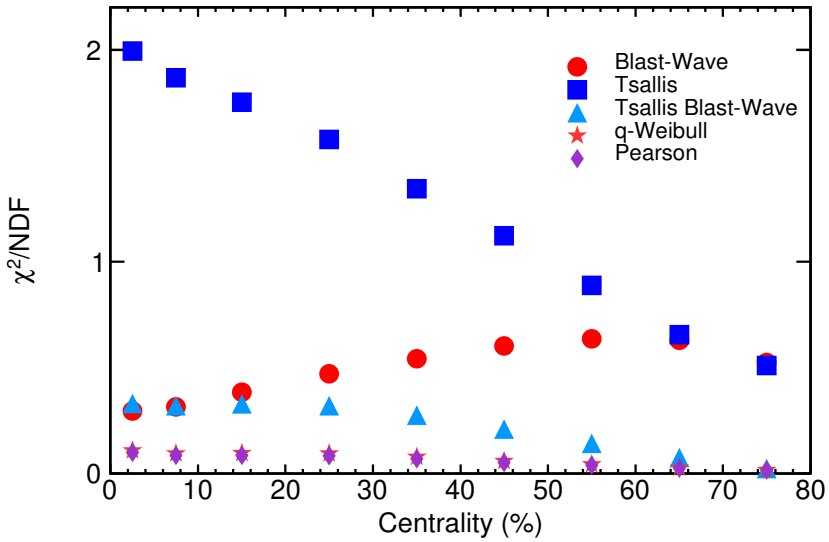

Figure 5.7: Fitted value of χ^2/NDF for different functions fitted with p_{T}-spectra data of particles produced at 2.76 $PbPb$ collision.

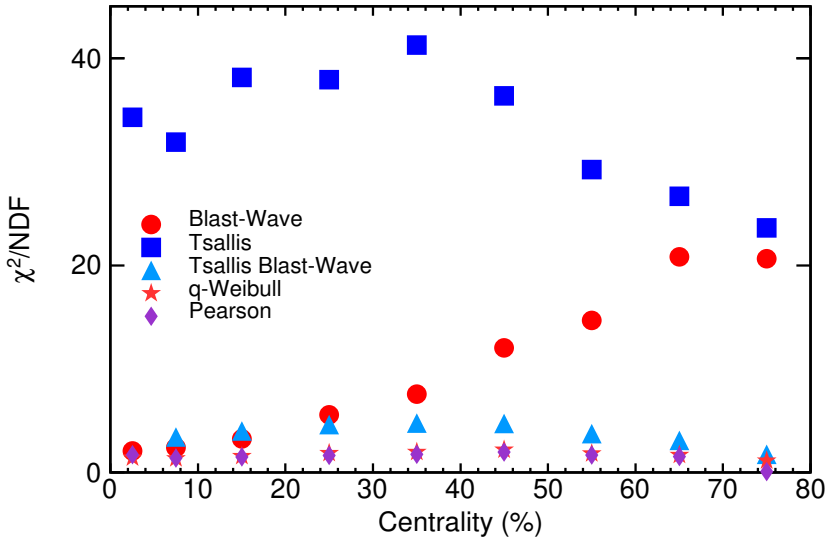

Figure 5.8: Fitted value of χ^2/NDF for different functions fitted with p_{T}-spectra data of particles produced at 5.02 $PbPb$ collision.

The trend in the value of parameter q with centrality can provide us with an insight into the deviation of the system from thermal equilibrium. A value of q close to one indicates a near-equilibrium system and any deviation from $q = 1$ shows how much a system drifts away from equilibrium. In Fig. 5.9 & 5.10, we observe an increasing trend in q value as we move from central to the peripheral collision for four different methods. This indicate a deviation from equilibrium as we move towards peripheral collision. These results are already reported for different energies in the Ref. [163, 162, 24].

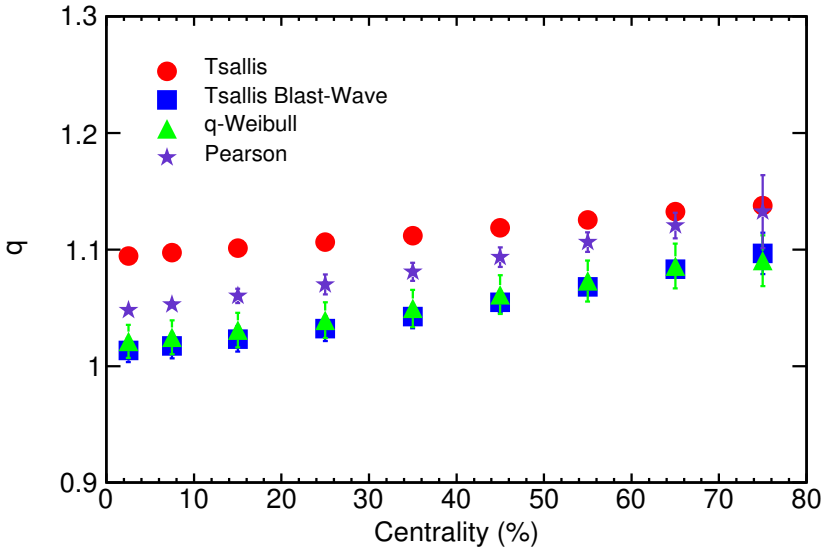

Figure 5.9: Fitted value of non-extensivity parameter 'q' for different fitting functions fitted with p_{T}-spectra data of particles produced at 2.76 TeV $PbPb$ collision.

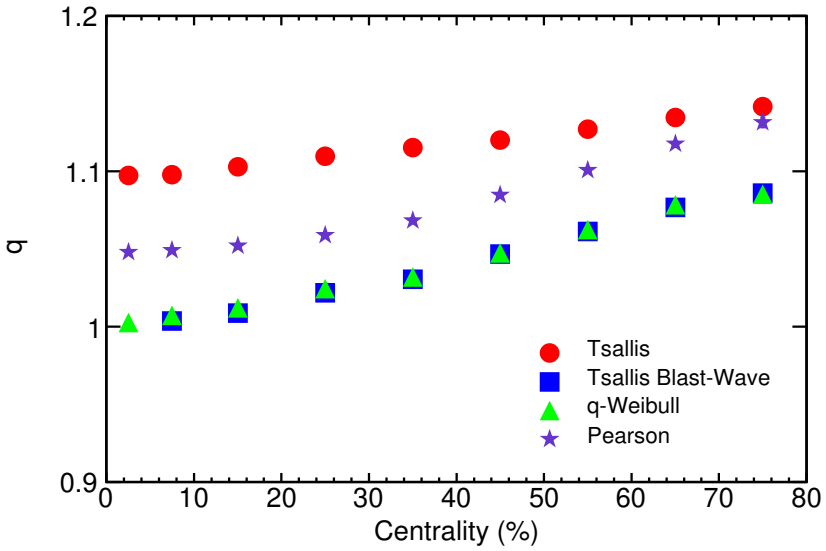

Figure 5.10: Fitted value of non-extensivity parameter 'q' for different fitting functions fitted with p_{T}-spectra data of particles produced at 5.02 TeV $PbPb$ collision.

Studying different phenomenological models on the spectra, we observe that the unified distribution nicely describe the dataset for charged hadrons at two different LHC energies. This observation is also complemented by the low χ^2/NDF values as shown in table 5.5.

5.3 Large Transverse Momentum

As discussed in the chapter 1, presence of the strongly interacting QGP medium leads to the quenching of jets. Due to this effect, there is a suppression in the high-p_{T} region of the p_{T}-spectra as the final state particles coming from the jet primarily populate the high-p_{T} region. From the Fig. 5.11, we clearly observe a suppression in the p_{T}-spectra starting around $4-5$ GeV/c. The suppression in more prominent in the central collisions. We can conclude that the presence of the quenching effect in heavy-ion collision modify the spectra at large p_{T} and hence the application of statistical thermal models is limited upto 5 GeV/c. However, we know that the effect of in-medium energy loss is absent in the spectra of particles produced in pp collision, which requires us to analyze the data of pp collision at different energies using unified formalism to test whether the developed formalism cover a broad range of p_{T} .

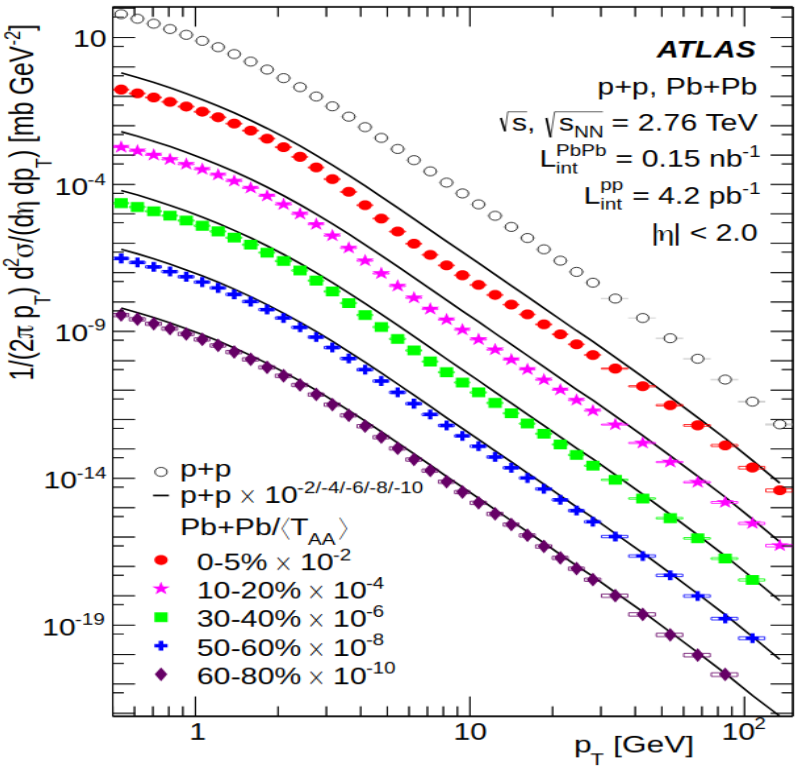

Figure 5.11: Transverse momentum spectra of charged hadron produced in 2.76 TeV $PbPb$ and pp collision. Solid lines represent the scaled pp collision. (Image taken from the Ref. [5].)

Tsallis statistics, in its original form, is not suitable to study the spectra in the broad p_{T} region particularly in the high-p_{T} regions, hence some modifications have been proposed in Ref. [168, 25, 221] to include the effect of hard scattering processes. One such

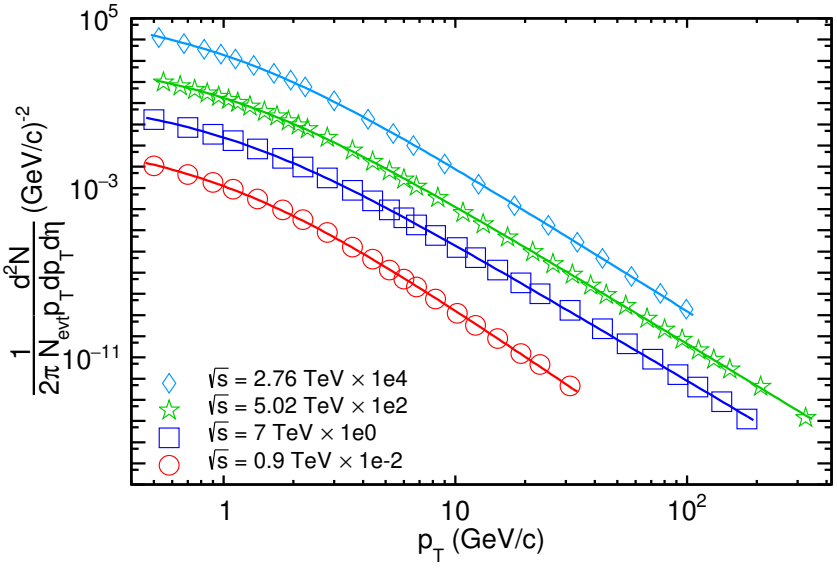

Figure 5.12: The three-component Tsallis function (Eq. 5.1) fit to the transverse momentum data of charged hadrons produced in pp collision at four different energies measured by CMS experiment [26, 27, 28].

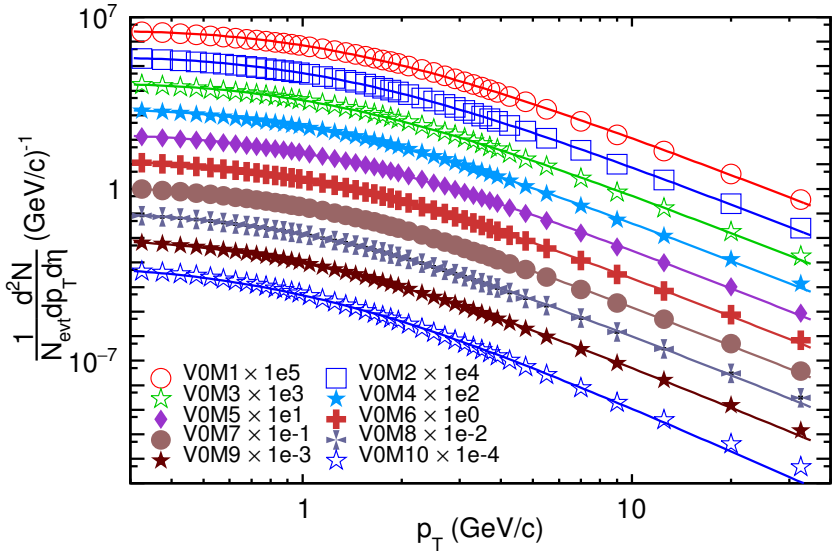

Figure 5.13: The three-component Tsallis function (Eq. 5.1) fit to the transverse momentum data of charged hadrons divided into multiplicity classes produced in pp collision at 7 TeV measured by ALICE experiment [29].

modification is the three-component Tsallis distribution [221], which is introduced to study the p_{T}-spectra of charged hadrons produced in pp collision at 0.9 & 7 TeV and it has been shown that the modified formalism nicely fit the spectra even at very large p_{T} values. The three-component Tsallis formalism considers that the charged hadron spectra consist primarily of pions, kaons and protons, the distribution function for the charged hadrons spectra

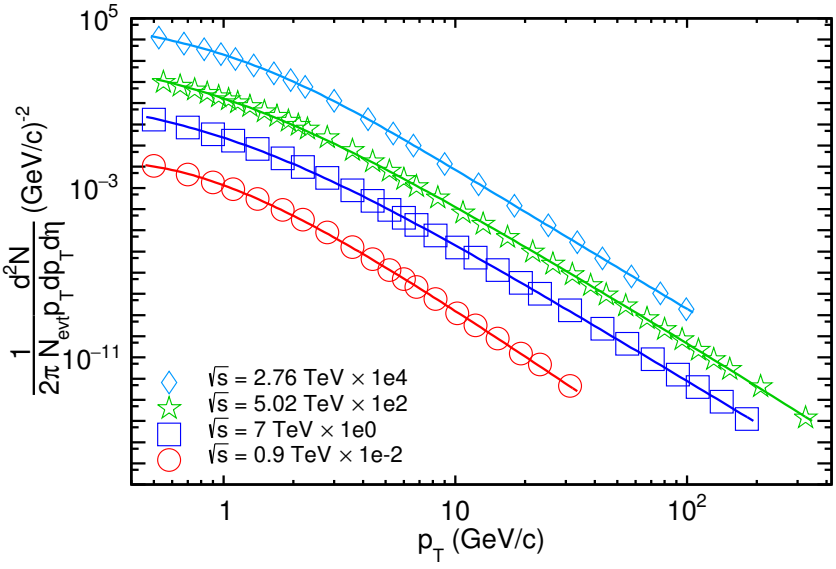

Figure 5.14: The unified function (Eq. 4.34) fit to the transverse momentum data of charged hadrons produced in pp collision at four different energies measured by CMS experiment [26, 27, 28].

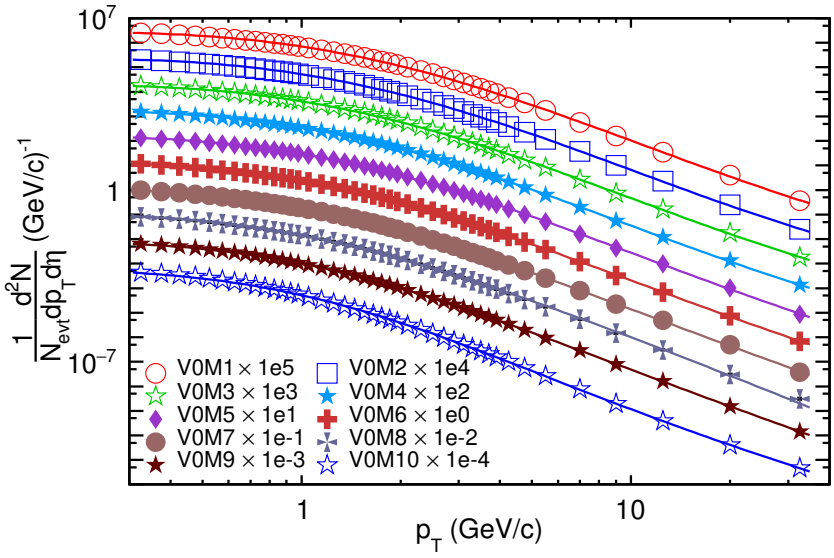

Figure 5.15: The unified function (Eq. 4.34) fit to the transverse momentum data of charged hadrons divided into multiplicity classes produced in pp collision at 7 TeV measured by ALICE experiment [29].

in this formalism is given as:

$$\frac{1}{2\pi p_T}\frac{d^2N}{dp_T dy} = 2\frac{V}{(2\pi)^3}\sum_{i=1}^{3} g_i m_{T,i}\left[1+(q-1)\frac{m_{T,i}}{T}\right]^{-\frac{q}{q-1}} \tag{5.1}$$

Here the summation index i runs over π^+, K^+ and p with the additional factor 2 taking care of the corresponding antiparticles. The degeneracy factor for different mesons are given by

Table 5.8: Multiplicity classes $\langle dN_{ch}/d\eta \rangle$.

Multiplicity class	7 TeV pp collision
V0M I	21.3 ± 0.6
V0M II	16.5 ± 0.5
V0M III	13.5 ± 0.4
V0M IV	11.5 ± 0.3
V0M V	10.1 ± 0.3
V0M VI	8.45 ± 0.25
V0M VII	6.72 ± 0.21
V0M VIII	5.4 ± 0.17
V0M IX	3.9 ± 0.14
V0M X	2.26 ± 0.12

$g_{\pi^+} = g_{K^+} = 1$ and for proton $g_P = 2$.

Although this function fits the data but the number of parameters becomes large. Also the three-component Tsallis model doesn't provide any explanation of the hard process whereas the unified distribution explains both soft and the hard processes. In this section, we test the applicability of unified model over a broad $p_{\rm T}$ range [222], *i.e.*, upto a few hundreds of GeV/c. We have also provided the results for the three-component Tsallis formalism [221] as a reference for comparison.

The dataset considered for this analysis includes the $p_{\rm T}$-spectra of charged hadrons that are produced in pp collision at 900 GeV [26], 2.76 TeV [27], 5.02 TeV [28] and 7 TeV [26] measured by the CMS experiment. The high multiplicity pp collision data at 7 TeV [29] measured recently by the ALICE experiment are also taken. In the ALICE experiment, the event can be divided into separate multiplicity classes depending on the number of charged particles deposited in the V0 detectors in a given pseudorapidity window. This high multiplicity dataset includes the spectra divided into different multiplicity classes as per the ALICE classification as shown in table 5.8. The dataset taken for the analysis has a varied pseudorapidity range. The spectra at 0.9 TeV & 7 TeV belong to $|\eta| < 2.4$ [26] and $|\eta| < 1$ for 2.76 TeV [27] & 5.02 TeV [28] as measured by CMS experiment. The V0M multiplicity class divided data measured by ALICE experiment at 7 TeV [29] correspond to $|\eta| < 0.5$. The fit results from the unified model & three-component Tsallis model are discussed below.

In Fig. 5.12, the three component Tsallis fit to the data is presented for four different collision energy with the maximum $p_{\rm T}$ range upto 400 GeV/c. The similar fit for the multiplicity divided 7 TeV data is provided in the Fig. 5.13. Figure 5.14 & 5.15 depicts the

Table 5.9: Best fit value of the parameters T (GeV), q, p_0 (GeV/c) & n and the χ^2/NDF value obtained by fitting the multiplicity class divided charged hadron spectra produced in pp collision at 7 TeV measured by the ALICE experiment [29] with the unified distribution function Eq. (4.34).

Mult. class	T	q	p_0	n	χ^2/NDF
V0M I	0.221 $\pm$0.011	1.146 $\pm$0.004	73.878 $\pm$11.3	$-$7.282 $\pm$0.367	0.996
V0M II	0.211 $\pm$0.010	1.145 $\pm$0.004	86.114 $\pm$10.817	$-$8.973 $\pm$0.377	0.787
V0M III	0.202 $\pm$0.011	1.142 $\pm$0.005	44.988 $\pm$6.725	$-$5.967 $\pm$0.274	0.639
V0M IV	0.194 $\pm$0.010	1.132 $\pm$0.005	17.558 $\pm$1.945	$-$4.231 $\pm$0.293	0.518
V0M V	0.190 $\pm$0.017	1.136 $\pm$0.009	18.987 $\pm$9.757	$-$3.811 $\pm$0.483	0.518
V0M VI	0.182 $\pm$0.017	1.129 $\pm$0.009	13.101 $\pm$2.540	$-$3.903 $\pm$0.522	0.321
V0M VII	0.166 $\pm$0.003	1.114 $\pm$0.001	7.026 $\pm$1.062	$-$4.336 $\pm$0.151	0.337
V0M VIII	0.167 $\pm$0.005	1.121 $\pm$0.002	11.110 $\pm$1.306	$-$4.583 $\pm$0.433	0.107
V0M IX	0.156 $\pm$0.005	1.135 $\pm$0.003	13.28 $\pm$3.067	$-$3.342 $\pm$0.095	0.377
V0M X	0.126 $\pm$0.005	1.077 $\pm$0.002	6.417 $\pm$0.195	$-$9.693 $\pm$0.557	0.726

Table 5.10: Best fit value of the parameters T (GeV), q, p_0 (GeV/c) & n and the χ^2/NDF value obtained by fitting the charged hadron spectra produced in pp collision at 0.9 TeV [26], 2.76 TeV [27], 5.02 TeV [28] and 7 TeV [26] measured by the CMS experiment with the unified distribution function Eq. (4.34).

Energy	T	q	p_0	n	χ^2/NDF
0.9 TeV	0.078 $\pm$0.009	1.032 $\pm$0.003	3.603 $\pm$0.131	$-$25.58 $\pm$3.119	1.79
2.76 TeV	0.132 $\pm$0.006	1.07 $\pm$0.002	4.014 $\pm$0.231	$-$8.926 $\pm$0.363	0.996
5.02 TeV	0.146 $\pm$0.007	1.122 $\pm$0.001	2.737 $\pm$0.422	$-$2.603 $\pm$0.011	3.119
7 TeV	0.125 $\pm$0.001	1.147 $\pm$0.001	0.849 $\pm$0.046	$-$1.184 $\pm$0.009	4.559

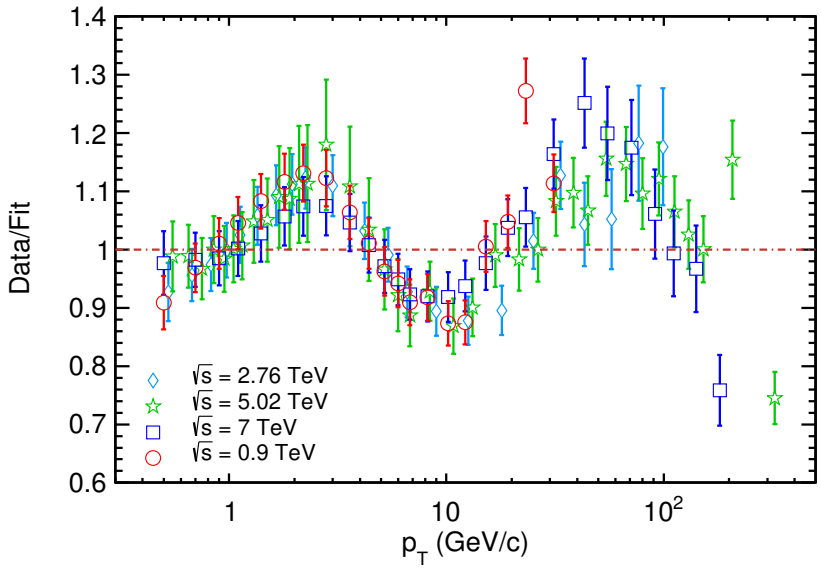

Figure 5.16: The ratio plot for four different energies fitted with the Tsallis distribution Eq. (5.1).

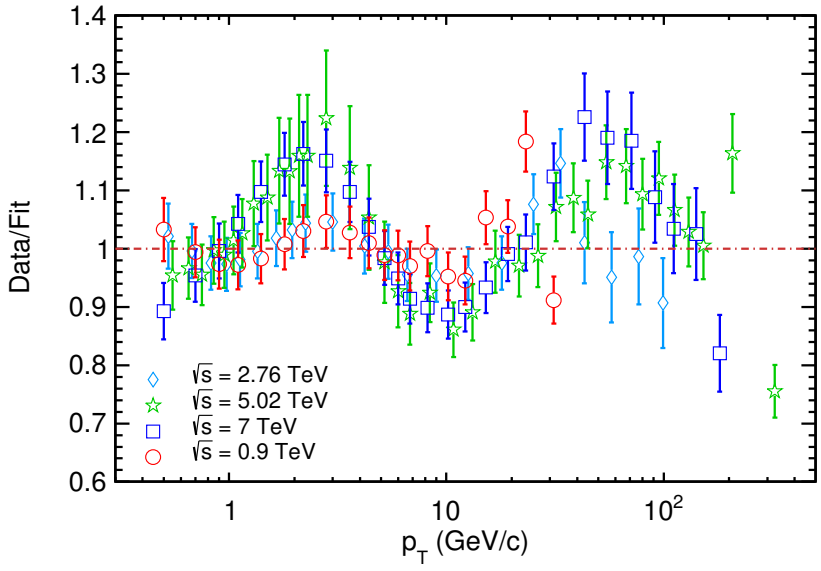

Figure 5.17: The ratio plot for four different energies fitted with the unified distribution Eq. (4.34).

unified function fit to different energies and different multiplicity classes divided 7 TeV data respectively. Although both of the function provide a good explanation to the data, however, the unified model show some improvement in the fit quality compared to the three-component Tsallis model. This improvement can be become more prominent in the ratio plot where we study the ratio of data to the fit function. The ratio plots are presented in the figures 5.16, 5.17, 5.19 & 5.18.

We observe a similar range of variation from the ideal value of one in the different energy

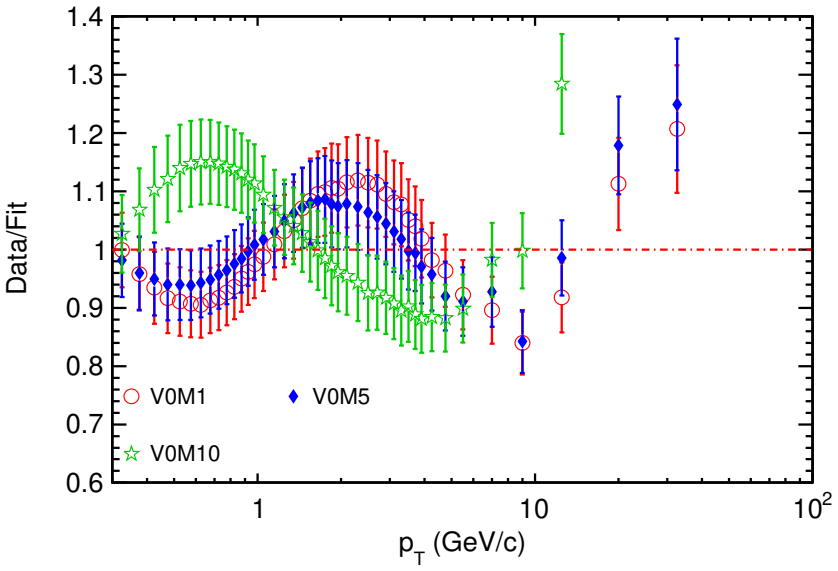

Figure 5.18: Ratio plot for three different multiplicity classes of 7 TeV pp collision data fitted with the Tsallis distribution Eq. (5.1).

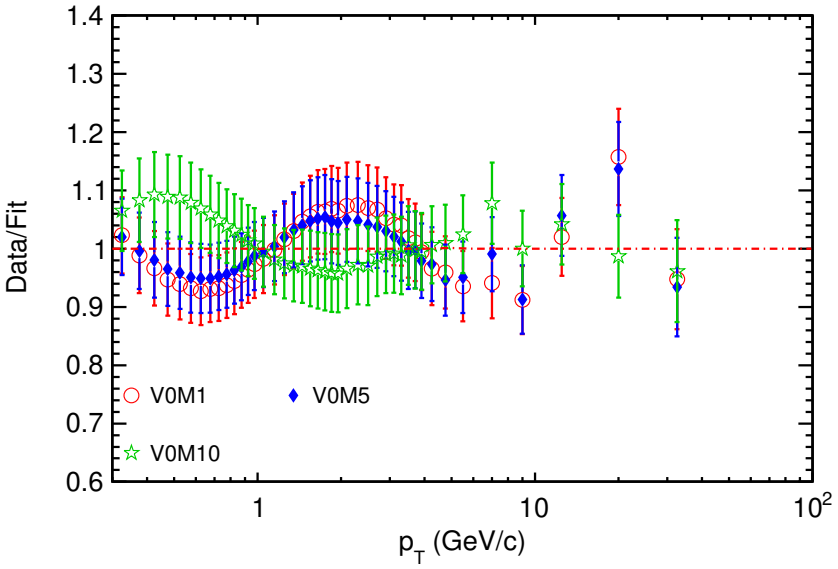

Figure 5.19: Ratio plot for three different multiplicity classes of 7 TeV pp collision data fitted with the unified distribution Eq. (4.34).

ratio plots obtained from Tsallis fit (Fig. 5.16) and unified function fit (Fig. 5.17). However, from the ratio plots for multiplicity divided 7 TeV collision data, we observe a significant improvement in the fit quality from the unified distribution (Fig. 5.19) as compared to the three-component Tsallis distribution (Fig. 5.18). This improvement is more prominent in the high-p_{T} region where the hard scattering processes dominate, stressing that the unified formalism improves the fit in high-p_{T} region.

We observe a log-periodic form of the oscillation pattern in the ratio plots presented

in figures 5.16, 5.17, 5.19 & 5.18 over a broad p_{T} range for both the unified and three-component Tsallis formalism. Similar oscillation pattern was also reported for different datasets in the Ref. [221, 223, 224]. At the same time we observe an interesting trend in the oscillation pattern for different multiplicity classes. We observe a clear reversal in the oscillation pattern as we move from multiplicity class V0M1 to V0M10. We could not find any explanation regarding this strange oscillation pattern. Thus we suspect there may be some interesting phenomena hidden inside this & need a further theoretical explanation which is beyond the scope of this thesis work.

5.4 Summary

In the words of Nobel laureate physicist Richard P. Feynman, *It doesn't matter how beautiful your theory is, it doesn't matter how smart you are. If it doesn't agrees with experiment, it's wrong.* So in this chapter we have tested whether the unified statistical framework discussed in chapter 4 agrees with the experimental data of transverse momentum spectra. In this chapter we aim to test the applicability of unified model over a broad energy range, different centralities and collision systems. We also aim to study whether the unified model provides improvement in the fit quality compared to the existing phenomenological models.

We have fitted the transverse momemtum spectra of charged hadrons and positive pion produced in different energy collision including RHIC energies (19.6, 27, 39, 130 & 200 GeV) and the LHC energies (0.9, 2.76, 5.02, 5.44 & 7 TeV). The datasets belongs to different collision system such as $PbPb$, $AuAu$, $XeXe$ & pp. We have performed the analysis over different centralities to study the variation of different fit parameters with the extent of overlap in the collision. The fit quality of unified model has been compared with the different phenomenological models including the BG, Tsallis, BW, TBW, q-Weibull and three-component Tsallis model.

The result obtained in this study are listed below.

- The study over a broad energy range and different collision system suggests that the unified model provide a good explanation of the p_{T}-spectra.
- A model comparison study shows that the lowest χ^2/NDF values are obtained from the unified model advocating that the unified model provides best explanation of the p_{T}-spectra.

These results suggests that the unified formalism agrees well with the experimental data of transverse momentum spectra. The application of the unified model to estimate different quantities of interest is provided in the next chapter and will also discuss the study of the pseudorapidity distribution within the unified statistical framework.

Chapter 6

Application & Further Discussion

A statistical thermal model, apart from fitting the spectra, can also provide information about the system created in high energy collision. In this direction, we have attempted to utilize the unified statistical framework developed & discussed in the early chapters to investigate some of the quantities of interest that are not directly observed.

A brief description of the quantities that we will discuss in the following sections are provided below.

- The pseudorapidity distribution of the final state particles in heavy-ion collision gives a quantitative description of number of particles produced as a function of velocity of particle, which in turn can give information about the entropy of the system. We will discuss the multiple fireball scenario within the unified statistical framework to study the pseudorapidity distribution of particles created in high energy collision.

- Since the unified distribution is thermally consistent, we will also check the thermal response functions in the unified framework. The thermodynamical response functions such as the isothermal compressibility and the speed of sound are not directly observable, however, they play a crucial role in understanding the nature of the system created in the collision. We will discuss the formalism to estimate these quantities within the framework of unified distribution.

- We will also explore the relation between the parameter of the unified distribution and the second order flow coefficient.

6.1 The Rapidity and Pseudorapidity Distribution

As discussed in Appendix B, the rapidity variable is defined as

$$y = \frac{1}{2} ln \frac{E + p_z}{E - p_z} \tag{6.1}$$

where E is the energy and p_z longitudinal momentum of the final state particles. The estimation of y requires the precise measurement of E & p_z, i.e. we need the information about 'mass' of each particles. In experiments, sometimes we lack the information of mass of the particles, so the pseudorapidity is measured instead of the rapidity and it is given as

$$\eta = -ln(tan(\theta/2) \tag{6.2}$$

Pseudorapidity (η) is defined only in term of the angle θ at which a particle is emitted with respect to the beam axis.

The distribution of the pseudorapidity of the final state charged particle provides us with the information crucial to understand the mechanism of particle production and the initial energy density of the system created in high energy collision. The study of the centrality and the collision system dependence of the primary charged particle pseudorapidity density $(dN_{ch}/d\eta)$ over a broad η range also gives us an insight into the relative contribution of hard and soft processes in the production of final state particles [225].

In an experiment, the geometry of the detectors systems is traditionally in the form of a cylinder and hence it covers primarily the central rapidity region. Due to difficulties in setting up the detector at forward rapidities, most of the experiments measure the kinematic observable such as η and p_{T} primarily in the mid-rapidity region. Hence the study of particle distribution over a wide η range requires a theoretical model that could extrapolate the data with good precision & is equally important to understand the η dependence of particle production.

Several theoretical models [226, 227, 228] with varied underlying physics have been proposed. A multi-source thermal model with four sources along with its Tsallis generalization is discussed in Ref. [226, 229]. Another model considering a three source scenario within the framework is the non-equilibrium statistical relativistic diffusion model and it is discussed in the Ref. [227]. This model considers that the charged hadrons produced

in the gluon-gluon interaction belong to the midrapidity source. And the remaining two sources at large rapidities correspond to the quark-gluon interaction. Hence, a large portion of the produced charged hadrons belong to the mid-rapidity source and the size of the mid-rapidity dip is controlled by their relative particle content. The mid-rapidity dip is mainly a mathematical artifact of particle production at $\theta = 90^o$. Another three source model, where the Landau hydrodynamics model describes the central source is discussed in Ref. [228].

In Ref. [230, 231], a model with a large number of fireballs along with the BG distribution is used to explain the pseudorapidity distribution of particles produced in high energy collision and its Tsallis generalization is discussed in Ref. [232, 233, 234]. This multiple fireball scenario assumes two cluster of fireballs and a q-Gaussian function is used to explain the rapidity distribution of these fireballs.

As discussed in the previous chapter, the energy distribution of the particles within the unified formalism is given as:

$$E\frac{d^3N}{dp^3} = B'\left(1+\frac{E}{p_0}\right)^{-n}\left(1+(q-1)\frac{(E-\mu)}{T}\right)^{-\frac{q}{q-1}} \tag{6.3}$$

We can replace E with $m_T cosh(y)$ and μ to zero for LHC energies, so the above equation modifies to:

$$\begin{aligned}\frac{1}{2\pi p_T}\frac{d^2N}{dp_T dy} = B'&\left(1+\frac{m_T cosh(y)}{p_0}\right)^{-n}\\ &\left(1+(q-1)\frac{m_T cosh(y)}{T}\right)^{-\frac{q}{q-1}}\end{aligned} \tag{6.4}$$

By integrating the above equation over p_{T}, we obtain the rapidity distribution of the secondaries produced from the decay of a fireball moving in the laboratory frame with the rapidity y_f.

$$\begin{aligned}\frac{dN}{dy} = A\int_0^\infty dp_T p_T&\left(1+\frac{m_T cosh(y-y_f)}{p_0}\right)^{-n}\\ &\left(1+(q-1)\frac{m_T cosh(y-y_f)}{T}\right)^{-\frac{q}{q-1}}\end{aligned} \tag{6.5}$$

In multiple fireball scenario, we consider a large number of such fireballs. The rapidity distribution of fireball $\nu(y_f)$ given in term of a double q-Gaussian function:

$$\nu\left(y_f\right) = G(y_0,\sigma;y_f) + G(-y_0,\sigma;y_f) \tag{6.6}$$

Here $G(y_0, \sigma; y_f)$ is the q-Gaussian given as:

$$G(y_0, \sigma; y_f) = \frac{1}{\sqrt{2\pi}\sigma} e_q \left(-\frac{(y_f - y_0)^2}{2\sigma^2} \right) \tag{6.7}$$

and the q-exponential $e_q(x)$ [165] is defined as:

$$e_q(x) \equiv [1 - (q-1)x]^{-\frac{1}{q-1}} \tag{6.8}$$

On substituting q-exponential and q-Gaussian in Eq. (6.6) we get:

$$\begin{aligned} \nu\left(y_f\right) =& \frac{1}{\sqrt{2\pi}\sigma} \left[1 + (q-1) \frac{\left(y_f - y_0\right)^2}{2\sigma^2} \right]^{-\frac{1}{q-1}} \\ &+ \frac{1}{\sqrt{2\pi}\sigma} \left[1 + (q-1) \frac{\left(y_f + y_0\right)^2}{2\sigma^2} \right]^{-\frac{1}{q-1}} \end{aligned} \tag{6.9}$$

in Eq. (6.9) y_0 represents the peak position and σ is the width of q-Gaussian.

As already discussed, we do not have always the information about the mass of individual particle, hence we measure the pseudorapidity of particle instead of rapidity. We use the Jacobian transformation from rapidity space to pseudorapidity space given as:

$$\frac{dy}{d\eta} = \sqrt{1 - \frac{m_0^2}{m_T^2 cosh(y)}} \tag{6.10}$$

Further, the relation between y and η will be of the form:

$$y = \frac{1}{2} \ln \left[\frac{\sqrt{p_T^2 \cosh^2(\eta) + m_0^2} + p_T \sinh \eta}{\sqrt{p_T^2 \cosh^2(\eta) + m_0^2} - p_T \sinh \eta} \right] \tag{6.11}$$

Finally, one can obtain the distribution of charged hadrons pseudorapidity by integrating over p_{T} and y_f in the equation:

$$\begin{aligned} \frac{dN}{d\eta} =& A \int_{-\infty}^{\infty} dy_f \int_0^{\infty} dp_T p_T \sqrt{1 - \frac{m_0^2}{m_T^2 \cosh^2(y)}} \\ &\times \nu\left(y_f\right) \left(1 + \frac{m_T cosh(y - y_f)}{p_0} \right)^{-n} \\ &\times \left[1 + (q-1) \frac{m_T \cosh\left(y - y_f\right)}{T} \right]^{-\frac{q}{q-1}} \end{aligned} \tag{6.12}$$

with the distribution of the fireball as in Eq. (6.9). The rapidity y can be replaced by Eq. (6.11). The numerical integration is performed to solve the integral equation Eq. (6.12). The experimental data of pseudorapidity distribution are fitted with the Eq. (6.12) considering y_0 and σ as the free parameters that needs to be tuned to obtain the best fit. As we have shown earlier, the numerical value of parameters q, T, p_0 & n that appears in the Eq. (6.12), are obtained by fitting transverse momentum spectra using the Eq. (4.34).

Discussion

We have tested the applicability of unified framework based pseudorapidity distribution function [235] by analysing the experimental $dN_{ch}/d\eta$ distribution of charged hadron produced in 2.76 TeV $PbPb$ [30, 31] and 5.44 TeV $XeXe$ [32] collision. To extract the

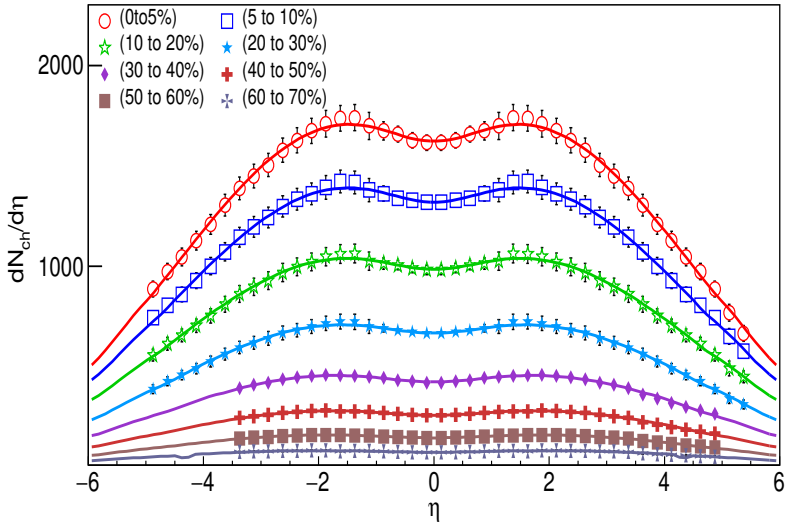

Figure 6.1: The unified pseudorapidity function fit (Eq. 6.12)over the range $-6 \leq \eta \leq 6$ for the pseudorapidity distribution of charged hardon produced in $\sqrt{s_{NN}} = 2.76$ TeV $PbPb$ collision [30, 31].

numerical value of the thermodynamical parameters q, T, p_0 and n, we have fitted the transverse momentum spectra of charged hadrons produced in 2.76 TeV $PbPb$ [16] and 5.44 TeV $XeXe$ [6] collision with the unified distribution function Eq. (4.34). The goodness of fit is tested in term of the χ^2/NDF values and the corresponding best fit data is provided in table 6.1.

The Fig. 6.1 & 6.3, depict the unified function (Eq. 6.12) fit to the pseudorapidity distribution data of charged hadrons at two different energies. These figures shows that the

Table 6.1: The χ^2/NDF values for the pseudorapidity data at 2.76 TeV and 5.44 TeV fitted with the distribution function Eq. (6.12).

Centrality	χ^2/NDF	
	2.76 TeV	5.44 TeV
0 to 5 %	$3.99/39$	-
5 to 10 %	$3.135/39$	-
10 to 20 %	$2.757/39$	$3.671/53$
20 to 30 %	$1.988/39$	$3.366/53$
30 to 40 %	$1.611/31$	$2.831/53$
40 to 50 %	$1.407/31$	$3.5/53$
50 to 60 %	$1.269/31$	$5.112/53$
60 to 70 %	$4.557/31$	$4.849/53$
70 to 80 %	-	$4.382/53$

Table 6.2: Numerical values of $dN_{ch}/d\eta$ obtained from the fit function Eq. (6.12) along with the experimentally measured values for $PbPb$ collision at 2.76 TeV and the ratio (data/fit) for two different centralities.

η	**Centrality 0 to 5 %**			**Centrality 60 to 70 %**		
	Data	Fit	Ratio	Data	Fit	Ratio
-3.375	1388	1387.43	1.00	76.10	74.94	1.01
-2.875	1504	1526.06	0.98	80.00	79.77	1.00
-2.375	1627	1629.76	1.00	83.10	82.58	1.01
-1.875	1709	1691.15	1.01	84.30	83.24	1.01
-1.375	1739	1705.59	1.02	81.90	81.81	1.00
-0.875	1674	1678.64	1.00	78.90	78.82	1.00
-0.375	1627	1635.87	0.99	75.80	75.76	1.00
0.375	1627	1635.87	0.99	75.80	75.76	1.00
0.875	1674	1678.64	1.00	78.90	78.82	1.00
1.375	1739	1705.59	1.02	81.90	81.81	1.00
1.875	1709	1691.15	1.01	84.30	83.24	1.01
2.375	1627	1629.76	1.00	83.10	82.58	1.00
2.875	1504	1526.06	0.98	80.00	79.77	1.00
3.375	1388	1387.43	1.00	76.10	74.94	1.02
3.875	1209	1223.56	0.99	66.00	68.38	0.96
4.375	1046	1045.42	1.00	59.10	60.55	0.98
4.875	888	864.677	1.03	53.60	52.08	1.03

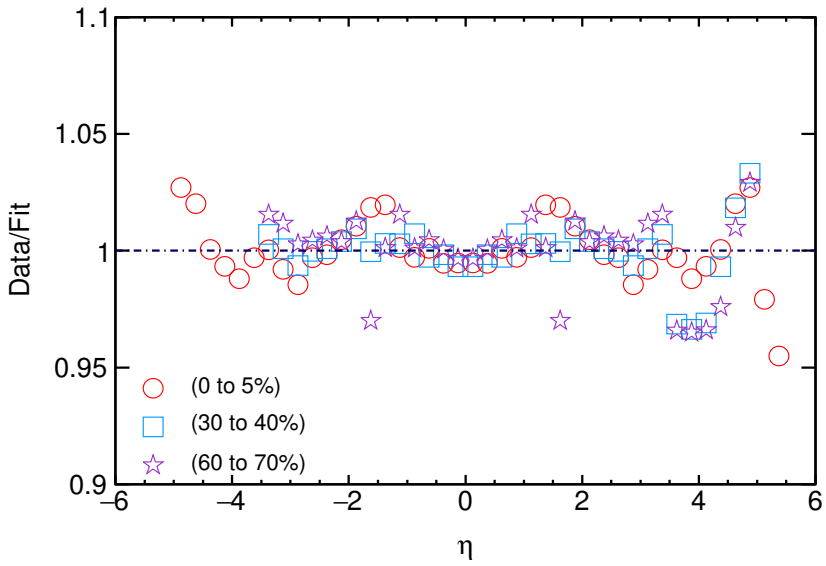

Figure 6.2: Ratio of data to the fit function for three different centralities $PbPb$ collision data at 2.76 TeV.

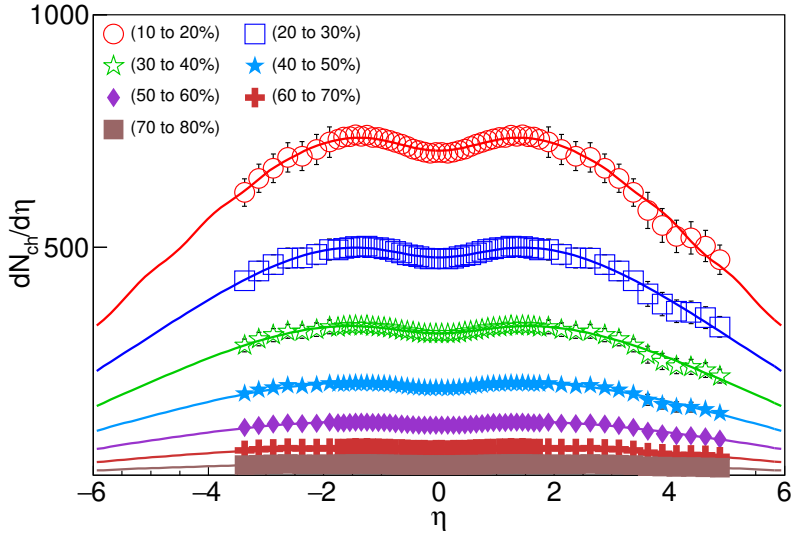

Figure 6.3: The unified pseudorapidity function fit (Eq. 6.12) over the range $-6 \leq \eta \leq 6$ for the pseudorapidity distribution of charged hardon produced in $\sqrt{s_{NN}} = 5.44$ TeV $XeXe$ collision [32].

function provided in Eq. (6.12) nicely explains the experimental data for different centralities and energy. The ratio of the value obtained from the data and the fit function plotted with respect to η in Fig. 6.2 & 6.4 also complement the above observation.

The rapidity of the two clusters that are considered to be moving toward each other in the multiple fireball scenario is presented in Fig. 6.5. And the distribution of the fireball rapidity within a cluster represented by the width of the q-Gaussian function is presented in

Table 6.3: Numerical values of $dN_{ch}/d\eta$ obtained from the fit function Eq. (6.12) along with the experimentally measured values for $XeXe$ collision at 5.44 TeV and the ratio (data/fit) for two different centralities.

η	**Centrality 10 to 20 %**			**Centrality 70 to 80 %**		
	Data	Fit	Ratio	Data	Fit	Ratio
-3.375	617.80	621.20	0.99	31.70	31.35	1.01
-2.875	669.90	670.69	1.00	33.50	32.76	1.02
-2.375	696.10	704.72	0.99	33.40	33.74	0.99
-1.75	732.20	731.57	1.00	33.60	34.22	0.98
-1.25	741.30	735.22	1.00	34.00	33.84	1.00
-0.75	725.50	724.08	1.00	33.00	32.89	1.00
-0.25	704.90	709.88	0.99	31.90	31.99	1.00
0.25	704.90	709.88	0.99	31.90	31.99	1.00
0.75	725.50	724.08	1.00	33.00	32.89	1.00
1.25	741.30	735.22	1.00	34.00	33.84	1.00
1.75	732.20	731.57	1.00	33.60	34.22	0.98
2.375	696.10	704.72	0.99	33.40	33.74	0.99
2.875	669.90	670.69	1.00	33.50	32.76	1.02
3.375	617.80	621.20	0.99	31.70	31.35	1.01
3.875	547.10	576.31	0.95	28.20	29.63	0.95
4.375	520.10	512.91	1.01	27.60	27.64	1.00
4.875	473.30	459.63	1.03	25.80	25.58	1.01

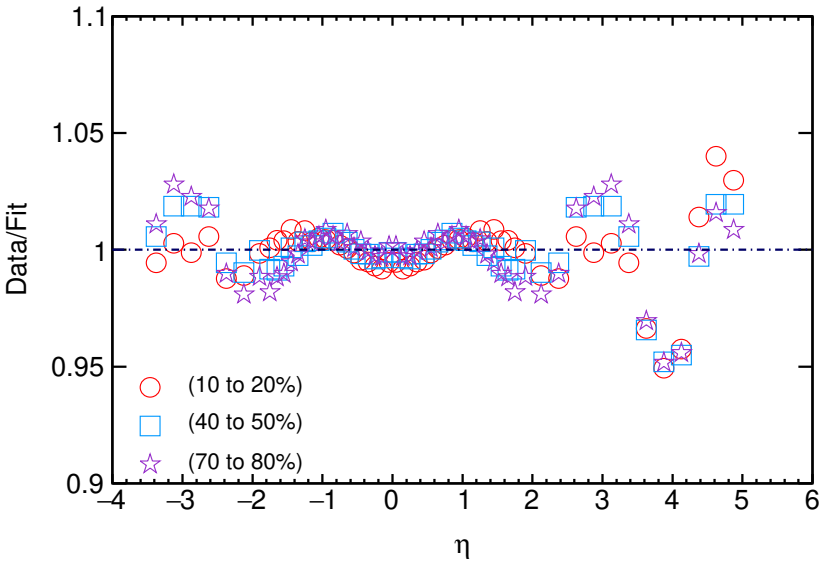

Figure 6.4: Ratio of data to the fit function obtained for three different centralities $XeXe$ collision data at 5.44 TeV.

Fig. 6.6.

From above results it can be concluded that the formalism developed considering the multiple fireball scenario within the unified statistical framework is in good agreement with the experimental data. Hence, this formalism can be utilized to study the pseudorapidity

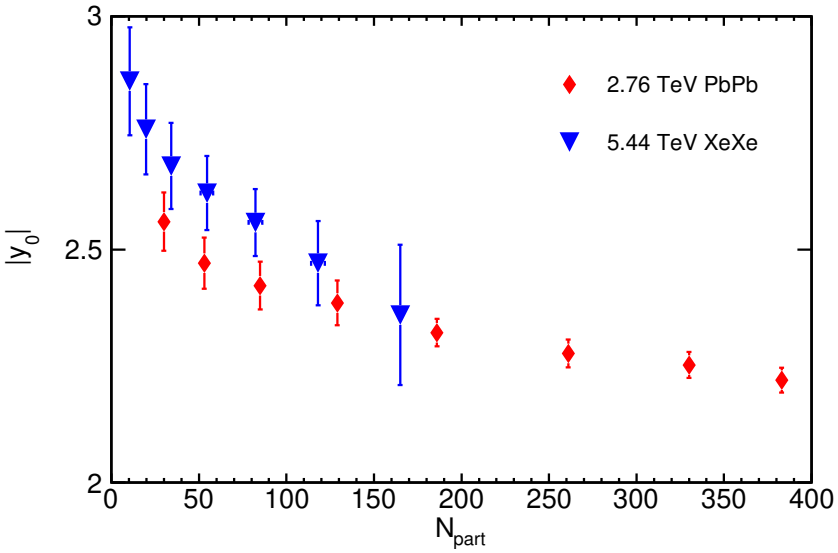

Figure 6.5: Variation of parameter $|y_0|$ with charged particle multiplicity for two different energies.

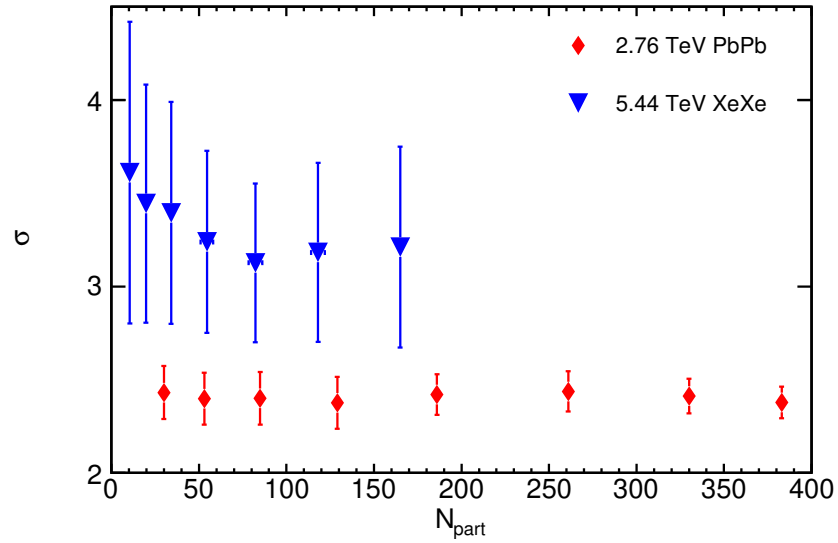

Figure 6.6: Variation of parameter σ with charged particle multiplicity for two different energies.

distribution over large η beyond the detector acceptance with good accuracy.

6.2 Thermodynamical Response Function

The response functions quantify the response of a system to the change in external parameters such as temperature, pressure etc. Some of the response functions that are of interest in high energy physics include the isothermal compressibility (κ_T), speed of sound (c_s)

and specific heat (C_V) [236, 237, 238]. These response functions play a crucial role in understanding the equation of state and the nature of the medium created in high energy collision.

Since the response functions are not directly observable, they can be extracted by studying the distribution of the transverse momentum as it is related to the energy distribution of the system. We have developed the formalism to study the isothermal compressibility and speed of sound within the unified statistical framework [239]. The section below discusses the mathematical formulation along with the result obtained for κ_T and c_s^2 using the experimental data of charged hadron spectra from the $PbPb$ collision at $\sqrt{s_{NN}}$ = 2.76 TeV [16], 5.02 TeV [240], and $XeXe$ collision at 5.44 TeV [32].

6.2.1 Isothermal Compressibility

The isothermal compressibility (κ_T) quantifies the change in volume of a system on the application of pressure at a fixed temperature and is important in studying the nearness of a system to a perfect fluid. The perfect fluids are ideal fluids that do not conduct heat and do not possess shear stress. The κ_T value for a perfect fluid is zero, which signifies that the fluid is incompressible. The perfect fluid does not exist, however, the value of κ_T close to zero as discussed in Ref. [241], suggests a near-perfect behaviour of the medium created in high energy collision. Other observations related to the shear viscosity to entropy density (η/s) ratio also points toward the near-perfect behaviour of medium [242, 243, 244].

In mathematical terms, the κ_T is given as:

$$\kappa_T = -\frac{1}{V}\left(\frac{\partial V}{\partial P}\right)_T \tag{6.13}$$

Further, κ_T is also related to the multiplicity fluctuation and the average number of particles [245] and the relation is given as:

$$\left\langle (N - < N >)^2 \right\rangle = var(N) = \frac{T < N >^2}{V}\kappa_T \tag{6.14}$$

The variance of particle multiplicity N is related to derivative of number density with re-

spect to chemical potential as:

$$\left\langle (N- < N >)^2 \right\rangle = VT\frac{\partial n'}{\partial \mu} \tag{6.15}$$

From above two equations, we can deduce the functional form of κ_T [236]:

$$\kappa_T = \frac{\partial n'/\partial \mu}{n^2} \tag{6.16}$$

where n', in case of unified formalism, is of the form:

$$n' = \int \frac{d^3p}{(2\pi)^3} \times \frac{B}{E}\left(1+\frac{E}{p_0}\right)^{-n}\left[1+(q-1)\frac{(E-\mu)}{T}\right]^{\frac{-q}{q-1}} \tag{6.17}$$

and,

$$\frac{\partial n'}{\partial \mu} = \int \frac{d^3p}{(2\pi)^3} \times \frac{q}{T} \times \frac{B}{E}\left(1+\frac{E}{p_0}\right)^{-n}\left[1+(q-1)\frac{(E-\mu)}{T}\right]^{\frac{1-2q}{q-1}} \tag{6.18}$$

Using the equations 6.16, 6.17 & 6.18, we have estimated the isothermal compressibility of the system created in heavy-ion collision at three different energies.

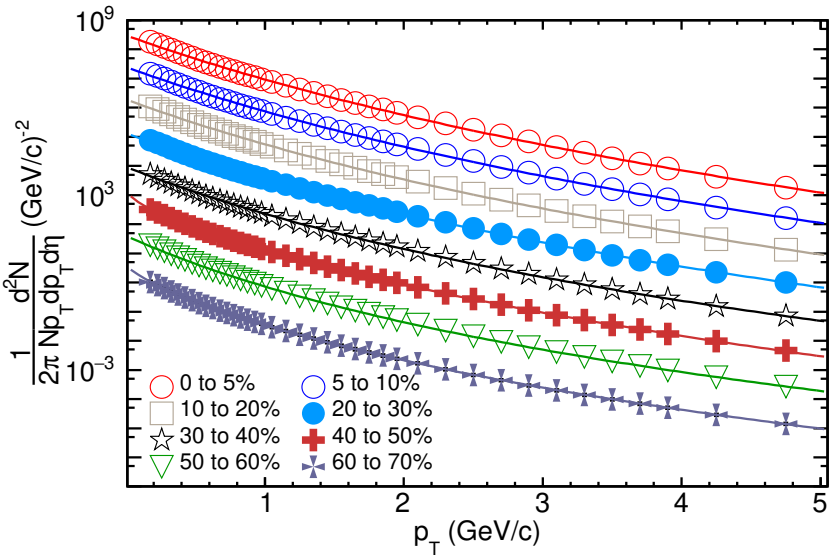

Figure 6.7: Unified function fit to the transverse momentum spectra of charged hadrons produced in 2.76 TeV $PbPb$ collision [16].

The estimation of κ_T requires information about the parameters T, q, p_0 & n. To obtain the numerical values analysis is performed using the p_{T}-spectra of charged hadrons produced in $PbPb$ collision at 2.76 [16] & 5.02 TeV [17] and $XeXe$ collision at 5.44 TeV [6].

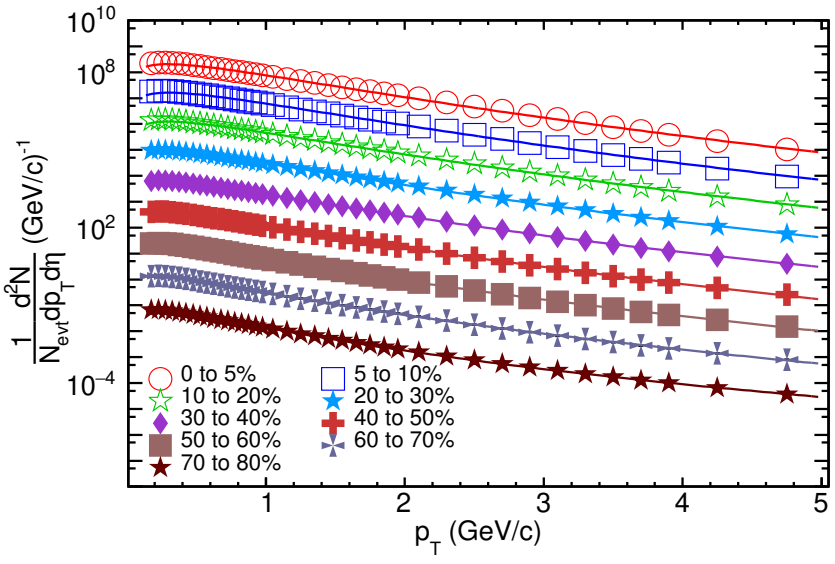

Figure 6.8: Unified function fit to the transverse momentum spectra of charged hadrons produced in 5.02 TeV $PbPb$ collision [16].

Table 6.4: The χ^2/NDF values for the p_{T}-spectra data at three different energies fitted with the unified distribution function Eq. (4.34).

Centrality	χ^2/NDF		
	2.76 TeV	5.02 TeV	5.44 TeV
0 to 5 %	3.43404/34	58.1109/34	-
5 to 10 %	2.90539/34	47.8639/34	-
10 to 20 %	2.92695/34	51.5548/34	11.4889/34
20 to 30 %	2.86397/34	56.5746/34	9.54121/34
30 to 40 %	2.37782/34	60.2901/34	9.9481/34
40 to 50 %	1.75793/34	66.8039/34	6.34837/34
50 to 60 %	1.32635/34	56.914/34	6.85773/34
60 to 70 %	0.873108/34	52.6224/34	7.97269/34
70 to 80 %	-	36.9991/34	8.75661/34

Since we are trying to study the bulk properties, so we have restricted the p_{T} range to $p_{\mathrm{T}} < 5$ GeV/c because the large p_{T} particles are primarily produced in hard processes.

The p_{T}-spectra of charged hadron produced in heavy-ion collision at 2.76 TeV, 5.02 TeV & 5.44 TeV is analyzed and the corresponding fit at different centralities are provided in the figures 6.7, 6.8 and 6.9 respectively. The χ^2/NDF value, which represent the goodness of fit is presented in the table 6.4. In tables 6.5, 6.6 and 6.7, the numerical value of the fit parameters $T,\ q,\ p_0$ & n that best describe the data is provided for different energies. These values have been used in the formalism discussed in the previous section to calculate the value of κ_T/V. The estimated values of isothermal compressibility is presented as a function of the charge particle multiplicity. At a particular centrality, the corresponding

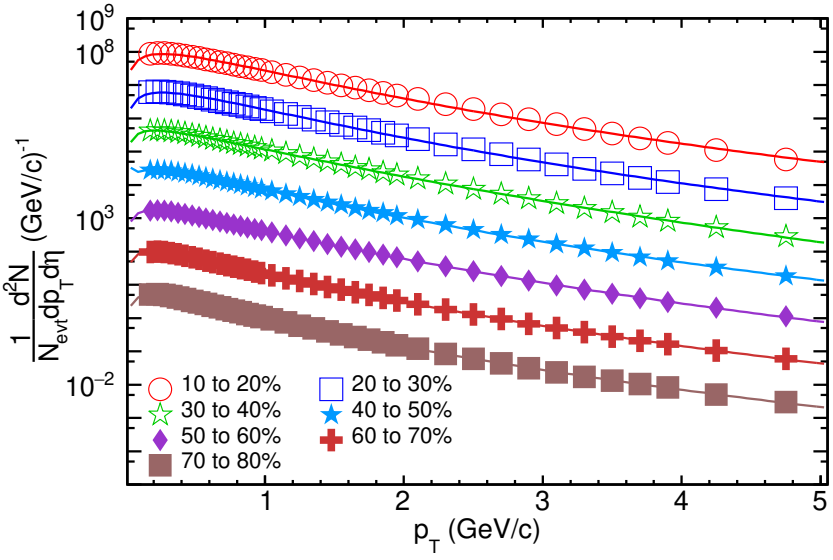

Figure 6.9: Unified function fit to the transverse momentum spectra of charged hadrons produced in 5.44 TeV $XeXe$ collision [6].

value of charged particle multiplicity $\left\langle \frac{dN_{ch}}{d\eta} \right\rangle$ is obtained from the Ref. [20, 246, 32].

Figure 6.10 depicts the isothermal compressibility over volume, κ_T/V, calculated using the equation (6.16), (6.17) & (6.18). We observe a decline in the value of κ_T/V with an increase in the charged particle multiplicity and at higher multiplicity the value approaches closer to the ideal behaviour. The trend observed in the Fig. 6.10 is within the expectation. This may be because the presence of a larger number of particles makes it difficult to compress at a higher multiplicity. Further, we observe similar values of κ_T/V at different energies which suggest similar dynamics of the medium produced in such collision. In the present analysis, the values calculated for κ_T/V using the unified formalism is in the range of $10^{-3} - 10^{-5}\ GeV^{-1}$.

Next missing part of this estimation is the correct evaluation of volume of the system. This is because calculating the numerical value of k_T (fm^3/GeV) require a proper estimation of volume. In this direction, several efforts have been made to extract the volume parameter using wide range of datasets [247, 191, 248, 249, 250, 221, 251, 252]. Different models give a different estimates of the volume, however, most of them lies in the range of $10^3 - 10^4\ fm^3$. So, considering the range of values for the volume parameter, the estimated value of k_T using unified formalism is in the order of $1 - 10\ fm^3/GeV$. Such low values of k_T indicate the near-ideal behaviour of the system created in the heavy-ion collision. Since the estimation of volume parameter is still an ongoing field of research, so, instead

Table 6.5: Numerical values of the fit parameters obtained by fitting the 2.76 TeV $PbPb$ collision experimental data of charged hadron p_{T}-spectra fitted with the unified formalism Eq. (4.34).

Centrality	T	q	p_0	n
0 to 5 %	0.393 ± 0.045	1.048 ± 0.004	0.105 ± 0.213	0.749 ± 0.356
5 to 10 %	0.386 ± 0.041	1.053 ± 0.004	0.088 ± 0.191	0.700 ± 0.319
10 to 20 %	0.370 ± 0.069	1.060 ± 0.006	0.060 ± 0.179	0.619 ± 0.302
20 to 30 %	0.351 ± 0.079	1.070 ± 0.008	0.038 ± 0.179	0.548 ± 0.302
30 to 40 %	0.331 ± 0.071	1.081 ± 0.008	0.026 ± 0.197	0.489 ± 0.343
40 to 50 %	0.311 ± 0.077	1.093 ± 0.008	0.034 ± 0.248	0.474 ± 0.461
50 to 60 %	0.292 ± 0.079	1.106 ± 0.008	0.046 ± 0.317	0.468 ± 0.608
60 to 70 %	0.273 ± 0.108	1.121 ± 0.012	0.075 ± 0.487	0.487 ± 1.034

Table 6.6: Numerical values of the fit parameters obtained by fitting the 5.02 TeV $PbPb$ collision experimental data of charged hadron p_{T}-spectra fitted with the unified formalism Eq. (4.34).

Centrality	T	q	p_0	n
0 to 5 %	0.407 ± 0.003	1.048 ± 0.001	0.002 ± 0.030	0.562 ± 0.045
5 to 10 %	0.415 ± 0.004	1.049 ± 0.001	0.017 ± 0.033	0.604 ± 0.050
10 to 20 %	0.422 ± 0.004	1.052 ± 0.001	0.039 ± 0.033	0.659 ± 0.055
20 to 30 %	0.424 ± 0.012	1.059 ± 0.001	0.081 ± 0.042	0.744 ± 0.072
30 to 40 %	0.412 ± 0.013	1.068 ± 0.001	0.082 ± 0.038	0.749 ± 0.070
40 to 50 %	0.369 ± 0.018	1.085 ± 0.002	0.050 ± 0.042	0.614 ± 0.084
50 to 60 %	0.340 ± 0.023	1.101 ± 0.002	0.053 ± 0.051	0.578 ± 0.114
60 to 70 %	0.311 ± 0.025	1.118 ± 0.002	0.066 ± 0.071	0.557 ± 0.169
70 to 80 %	0.329 ± 0.034	1.131 ± 0.003	0.156 ± 0.094	0.855 ± 0.293

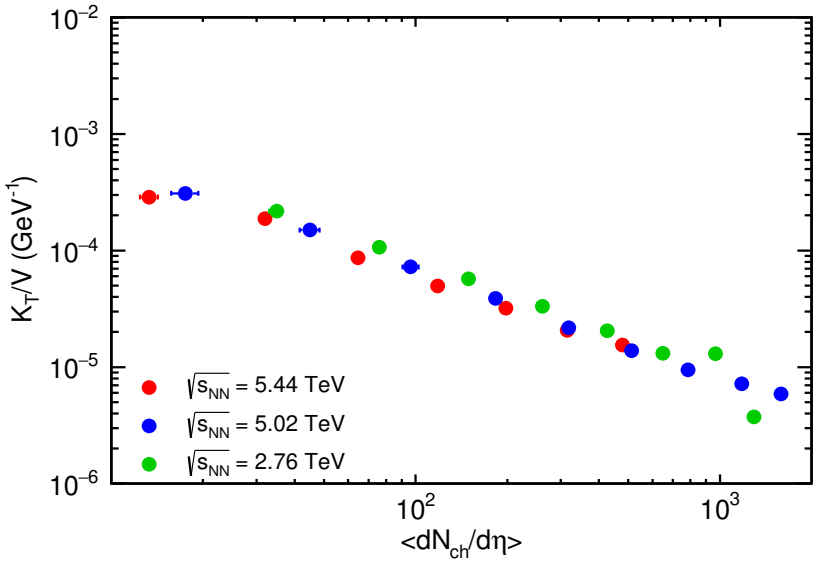

Figure 6.10: Isothermal compressibility over volume as a function of average charged particle multiplicity for $XeXe$ collision at $\sqrt{s_{NN}}$ = 5.44 TeV, $PbPb$ collision at $\sqrt{s_{NN}}$ = 5.02 TeV and $PbPb$ collisions at $\sqrt{s_{NN}}$ = 2.76 TeV using Unified formalism.

of selecting a particular model, we have presented the result in terms of k_T/V.

6.2.2 Speed of Sound

The speed of sound is pivotal in understanding the hydrodynamical evolution of the system produced in heavy-ion collisions [253]. It also provides information regarding the equation of state, which relates the energy density (ϵ) and the pressure (P). The value of the squared speed of sound c_s^2 is $1/3$ for a non-interacting massless ideal gas [254], hence, the comparison of c_s^2 value with the ideal gas can reveal the nature of the medium [255].

The squared speed of sound, c_s^2, is defined as the rate of change of pressure with the energy density at constant volume.

$$c_s^2 = \left(\frac{\partial P}{\partial \epsilon}\right)_V \tag{6.19}$$

In the above equation, P is pressure and ϵ is energy density of the system. The Eq. (6.19) can be further reduced to:

$$c_s^2 = \frac{\frac{\partial P}{\partial T}}{\frac{\partial \epsilon}{\partial T}} \tag{6.20}$$

In standard statistical mechanics, pressure can be presented in terms of the distribution

Table 6.7: Numerical values of the fit parameters obtained by fitting the 5.44 TeV $XeXe$ collision experimental data of charged hadron p_{T}-spectra fitted with the unified formalism Eq. (4.34).

Centrality	T	q	p_0	n
10 to 20 %	0.409 ± 0.012	1.072 ± 0.001	0.098 ± 0.075	0.720 ± 0.148
20 to 30 %	0.460 ± 0.032	1.067 ± 0.003	0.225 ± 0.106	1.101 ± 0.237
30 to 40 %	0.447 ± 0.037	1.079 ± 0.004	0.229 ± 0.097	1.112 ± 0.235
40 to 50 %	0.455 ± 0.050	1.091 ± 0.005	0.288 ± 0.127	1.306 ± 0.360
50 to 60 %	0.434 ± 0.084	1.108 ± 0.008	0.290 ± 0.152	1.317 ± 0.512
60 to 70 %	0.357 ± 0.070	1.123 ± 0.006	0.198 ± 0.170	0.943 ± 0.533
70 to 80 %	0.338 ± 0.094	1.139 ± 0.011	0.206 ± 0.257	0.974 ± 0.873

function of energy as:

$$P = \int \frac{d^3p}{(2\pi)^3}\frac{p^2}{3E} \times f(E) \tag{6.21}$$

Considering the Tsallis prescription of replacing $f(E)$ with $f^q(E)$ and then replacing $f(E)$ with the unified distribution of energy, we get:

$$P = \int \frac{d^3p}{(2\pi)^3} \times B \times \frac{p^2}{3E^2}\left(1+\frac{E}{p_0}\right)^{-n}\left[1+(q-1)\frac{E}{T}\right]^{\frac{-q}{q-1}} \tag{6.22}$$

and,

$$\epsilon = \int \frac{d^3p}{(2\pi)^3} \times B\left(1+\frac{E}{p_0}\right)^{-n}\left[1+(q-1)\frac{E}{T}\right]^{\frac{-q}{q-1}} \tag{6.23}$$

By using the above equations, the squared speed of sound c_s^2,

$$c_s^2 = \frac{\int \frac{p^2d^3p}{3E^2}\left(1+\frac{E}{p_0}\right)^{-n}\left[\frac{T}{q-1}+E\right]^{\frac{1-2q}{q-1}}}{\int d^3p\left(1+\frac{E}{p_0}\right)^{-n}\left[\frac{T}{q-1}+E\right]^{\frac{1-2q}{q-1}}} \tag{6.24}$$

For a deeper understanding of the system produced in the heavy-ion collision, the squared speed of sound is estimated for different energies. This quantity helps in understanding the equation of state, which in turn is crucial to study the hydro-dynamical properties of

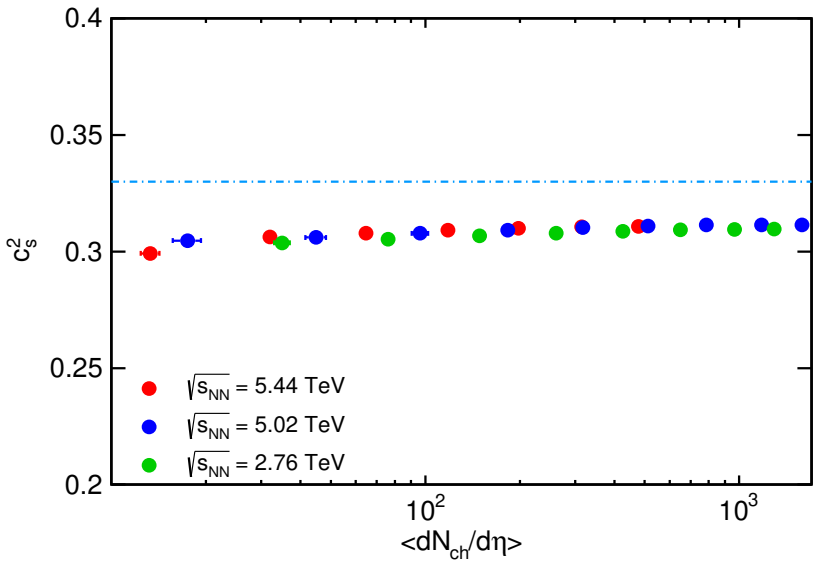

Figure 6.11: Squared speed of sound as a function of average charged particle multiplicity for $XeXe$ collision at $\sqrt{s_{NN}}$ = 5.44 TeV, $PbPb$ collision at $\sqrt{s_{NN}}$ = 5.02 TeV and $PbPb$ collisions at $\sqrt{s_{NN}}$ = 2.76 TeV using Unified formalism. The dotted line represents the theoretical value for ideal gas system.

the medium. The insight into the nature of the medium created in high energy collision can be gained by comparing with the ideal gas values of c_s^2. The squared speed of sound values obtained for three different energies calculated using the Eq. (6.24) are presented in Fig. 6.11. The theoretical value for the ideal gas is represented using the blue dotted line in the same figure. From the result obtained for 2.76, 5.02 and 5.44 TeV, we observe that the value of c_s^2 is close to the ideal gas value of $1/3$. Further, the values increase slightly with the increase in the charged particle multiplicity, suggesting the formation of a near ideal system at higher multiplicity. This observation complements the near-ideal behaviour already indicated from the measurement of isothermal compressibility in the previous section.

In conclusion, we have made an attempt to study some thermodynamic response functions such as isothermal compressibility and speed of sound using the unified statistical framework. The values of κ_T/V and c_s^2 estimated using the unified formalism point toward the near-ideal behaviour of the system created in the heavy-ion collision.

6.3 Discussion on the Geometrical Effect

Geometry effect in the non-zero impact parameter relativistic heavy-ion collision gives rise to non-sphericity in the system. The quantity used to quantify the departure from sphericity in the system is known as anisotropic flow. This initial geometry effect, via multiple collisions, results in momentum anisotropy in the final state particles Thus, the transverse momentum distribution of final state particles must have some imprint of azimuthal anisotropy produced due to flow. A precise understanding of anisotropic flow is crucial in order to understand the evolution dynamics of the QGP state.

Flow parameter can be characterized by doing the Fourier series expansion in azimuthal

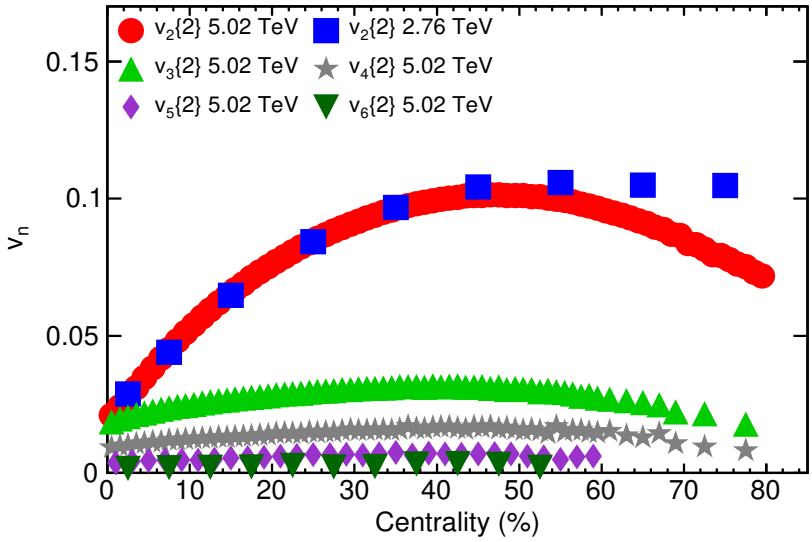

Figure 6.12: Variation of anisotropic flow coefficients v_n as a function of centrality of charged particles for 5.02 TeV with p_{T} range $0.2 < p_{\mathrm{T}} < 3$ GeV/c [33] and 2.76 TeV with p_{T} range $0.2 < p_{\mathrm{T}} < 5$ GeV/c [34] measured by ALICE experiment ($|\eta| < 0.8$) . Here, $\{2\}$ represent that v_n is calculated using two-particle cumulant method.

angle ϕ of particle yield spectra given as:

$$E\frac{d^3N}{dp^3} = \frac{1}{p_T}\frac{d^2N}{dp_T dy} \times \frac{N}{2\pi}[1 + 2\sum_h v_h cos\,\{h(\phi - \psi)\}] \tag{6.25}$$

where p is the momentum of particle, E the energy, p_{T} the transverse momentum, ϕ the azimuthal angle, y the rapidity, ψ the reaction plane angle, and v_h represent h^{th} order flow coefficient [82, 256]. Due to the presence of reflection symmetry with respect to the reaction plane, we do not have any sine term in the Fourier expansion [257].

Flow coefficient of h^{th} order (v_h) can be calculated using following equation:

$$v_h = \langle cos[h(\phi - \psi)] \rangle = \frac{\int d\phi \frac{dN}{d\phi} cos[h(\phi - \psi)]}{\int d\phi \frac{dN}{d\phi}} \tag{6.26}$$

with angle bracket representing average over all particles in all events.

The differential flow coefficient depends on the transverse momentum and the emission angle of particle with respect to collision axis. Integrated flow represents flow coefficient integrated over p_{T} and y as in Eq. (6.26). On the other hand, the differential flow coefficient is given as [2]:

$$v_h = \langle cos[h(\phi - \psi)] \rangle = \frac{\int d\phi \frac{d^3N}{p_T dp_T d\phi dy} cos[h(\phi - \psi)]}{\int d\phi \frac{d^3N}{p_T dp_T d\phi dy}} \tag{6.27}$$

The standard nomenclature for the naming of each of these coefficient are, v_1 is known as directed flow, v_2 the elliptic flow, v_3 the triangular flow and so on. During heavy-ion

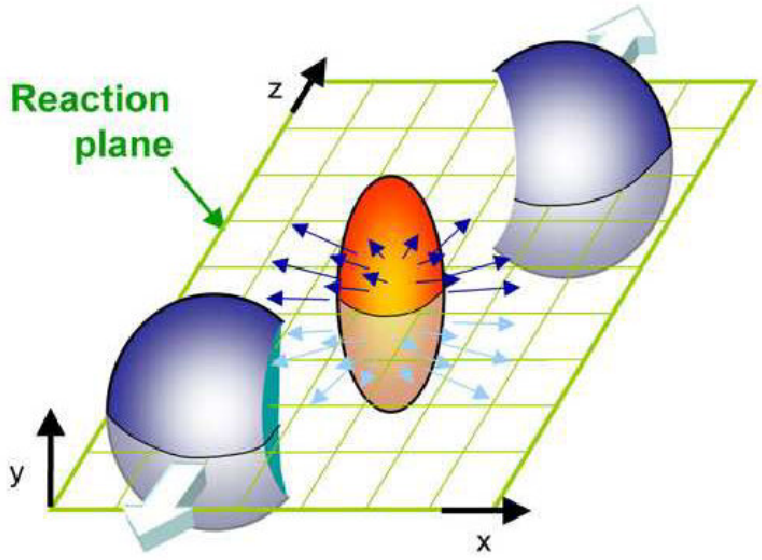

Figure 6.13: Elliptic flow in heavy-ion collision. (Image taken from Ref. [35])

collision with non-zero impact parameter, the overlapping area between colliding nuclei is dominantly ellipsoidal, as shown in the Fig. 6.13. Because of this ellipsoidal dominance in the collision geometry, major contribution in anisotropic flow comes from second-order flow coefficient v_2, whereas initial state fluctuation generates higher-order harmonics, as can be verified from Fig 6.12. Search for flow coefficient has been carried out in different heavy-ion collider experiments and large values observed at RHIC and LHC make it a key

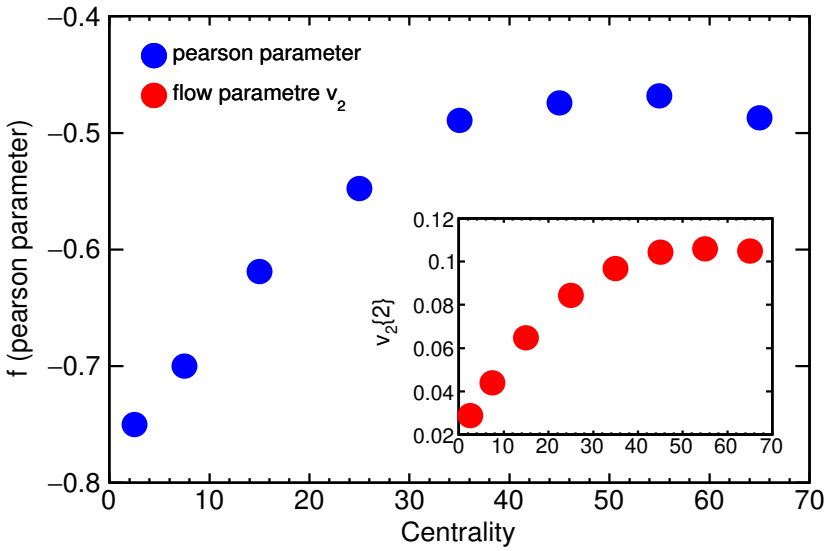

Figure 6.14: Unified function parameter f versus centrality (%) for charged hadrons at 2.76 TeV and inlay shows the $v_2\{2\}$ at same energy.

experimental finding from these experiments [33, 34, 51, 72, 73, 75, 243, 258, 259, 260, 261, 262, 263, 264].

6.3.1 Elliptic Flow and Unified Function Parameter

Since the flow coefficients are related to the azimuthal anisotropy in the distribution of transverse momentum, an imprint of flow might be present in the $p_{\rm T}$-spectra of final state particles. In this direction, we have explored the relation of the flow coefficient and the unified function parameters obtained by fitting the transverse momentum spectra.

In order to examine the correlation between fit parameter and the flow coefficient, we have investigated the elliptic flow coefficient ($v_2\{2\}$ extracted using the two particle cumulant method) of charged hadrons produced in $PbPb$ collision at 2.76 TeV measured by ALICE experiment [34]. We have considered the $p_{\rm T}$ integrated flow coefficient with $p_{\rm T}$ range from 0.2 to 5 GeV/c measured within the pseudorapidity interval of $|\eta| < 0.8$. The corresponding value of the unified function parameter is obtained by fitting the $p_{\rm T}$-spectra of charged hadrons produced in 2.76 TeV $PbPb$ collision [16] in same $p_{\rm T}$ and η interval for different centralities. In Fig. 6.14, we have provided the variation of the unified function fit parameter f and the elliptic flow coefficient with centrality. We observe that the variation of both the quantities with centrality is similar in nature. Another interesting

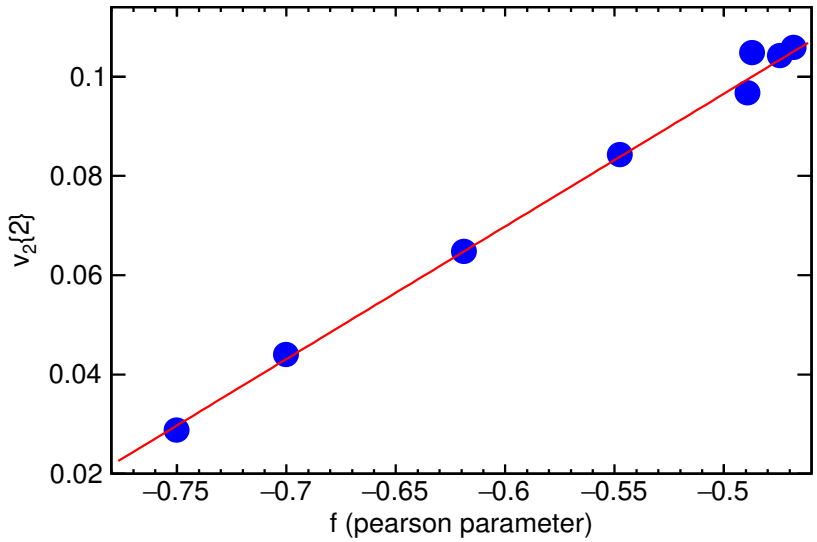

Figure 6.15: Elliptic flow coefficient versus unified function parameter f at 2.76 TeV $PbPb$ collision and the curve is fitted with a linear equation.

observation is that both flow coefficient and the unified function parameter peaks in the $50-60\%$ centrality bin. A linear relation between the two quantities is obtained by fitting the data points in Fig. 6.15 with the linear equation $v_2 = 0.267426f + 0.230294$. The Pearson correlation coefficient obtained for these two data is 0.9976, which shows that the unified function parameter f is linearly related to the elliptic flow coefficient.

The result discussed above shows that it is possible to obtain the flow coefficient v_2 directly from the transverse momentum spectra instead of the conventional flow analysis.

At this stage the evaluation of theoretical connection is beyond the scope of this thesis work. However a detailed study can be performed to find out the relationship of unified model to the flow coefficient.

6.4 Summary

It is important to explore the other avenues whether a statistical thermal model can be applied to gain more insight into the system created during the heavy-ion collision. So, in this chapter we have given few important applications of the unified statistical framework.

- We have discussed the multiple fireball scenario within the unified framework to study the pseudorapidity distribution and it is shown that this formalism nicely explains the pseudorapidity distribution of charged hadrons produced in 2.76 TeV $PbPb$ and

5.44 TeV $XeXe$ collision.

- The theoretical formalism to estimate some of the thermodynamical quantities such as the isothermal compressibility and the speed of sound using the unified framework is provided in the chapter. Using the developed formalism, we have also estimated the thermodynamical response functions for the medium created in heavy-ion collision at 2.76 TeV, 5.02 TeV and 5.44 TeV.

- We have also explored the connection between the unified function fit parameter and the second-order flow coefficient and we observed a linear relation for the charged hadron produced in $PbPb$ collision at 2.76 TeV.

Chapter 7

Summary and Outlook

A significant portion of research going on in heavy-ion collision is focused on studying the QGP state, which is believed to be formed a few microseconds after the Big Bang. Although it is not possible to directly detect this state in experiments, some indirect signatures such as jet quenching, J/ψ suppression and strangeness enhancement point toward the formation of QGP in experiments at RHIC and LHC.

The temperature that is sufficient to support the formation of QGP droplet is known as the transition temperature and at this point, the phase transition from hadronic state to QGP occurs. Therefore, estimating the value of the transition temperature, determining the QCD critical point and understanding the type of phase transition are some of the important milestones in the study of this deconfined state of quarks and gluons. An essential step toward estimating these quantities is the study of the QCD phase diagram, which is a plot of temperature (T) versus baryon chemical potential (μ_B). The temperature is extracted from the transverse momentum $(p_{\rm T})$ spectra, whereas the particle ratio is used to calculate the baryon chemical potential. Hence, in order to extract the temperature, which is a crucial ingredient of the QCD phase diagram, a proper parametrization of the form of transverse momentum spectra is necessary.

In this direction, several phenomenological models with varied physics inputs have been developed to study the transverse momentum spectra of final state particles produced in high energy collisions. This includes the statistical thermal models, hydrodynamical models and some multi-component models. Boltzmann-Gibbs distribution, Tsallis statistics, Blast-Wave model, Tsallis Blast-Wave model, q-Weibull distribution $\&$ modified Tsallis distribution are some of the models used to study different aspects of the $p_{\rm T}$-spectra. Most

of these models nicely explains the spectra in the low-p_{T} region, however, they start to deviate in the high-p_{T} part of the spectra. In high energy collision, particle production can be broadly classified into two distinct classes. The soft processes dominate the particle produced in the low-p_{T} region, whereas the majority of high-p_{T} particles belong to the hard scattering processes. The statistical thermal and hydrodynamical models nicely explain the bulk part of the spectra and we have a well defined QCD inspired power law form of the distribution function to explain the hard part of the spectra. Since there is no fine line separating the soft and hard part of the spectra hence, a formalism to describe both region in a unified manner is required to obtain the ultimate benefit from the spectra.

In this thesis, we have discussed a unified statistical framework based on the Pearson probability distribution function to study different aspect of particle production in high energy collision. Some of the important features of this unified model are:

- This framework nicely explains the transverse momentum spectra including both soft and hard part.

- The applicability of this formalism over different collision energies, centralities and collision system has been tested in the thesis and the result shows excellent agreement with the experimental data.

- The unified formalism discussed in this thesis has been proved to be thermodynamically consistent following the laws of thermodynamics.

- The formalism is also proved to be backward compatible with the Tsallis statistics within the limit on its parameters.

- Some of the results also suggest that the unified formalism can be used to estimate the second order flow coefficient.

- We have discussed a multiple fireball scenario within the unified statistical framework to study the pseudorapidity distribution of charged hadrons produced in $PbPb$ and $XeXe$ collision.

- Unified statistical framework can also be used to estimate the some of the response functions such as the isothermal compressibility and speed of sound.

In conclusion, this thesis presents a unified formalism to study the soft and hard part of the transverse momentum spectra in a consistent manner. Application of this formalism to study the pseudorapidity distribution and to extract the isothermal compressibility $\&$ the speed of sound is also discussed in the thesis.

7.1 Future Direction

The formalism discussed in the thesis motivates the study of plenty of other thermodynamical and hydrodynamical quantities of interest. Some of these quantities such as the isothermal compressibility and speed of sound has been discussed in the thesis. The study of several other quantities such as mean free path, thermal pressure, isobaric expansivity etc., can be carried out within the unified framework in the future to enhance our understanding of the system created in the high energy collision. The unified formalism can also be extended to study the multiplicity distribution of the particles. The effect of jet quenching on the transverse momentum spectra is significant beyond a certain $p_{\rm T}$ range in the heavy-ion collision. Hence, a parameterization scheme to include the quenching effect along with the unified formalism is important to study full $p_{\rm T}$ range in the heavy-ion collision.

Appendix A

Dynamics of HI Collision and Space-time evolution of QGP

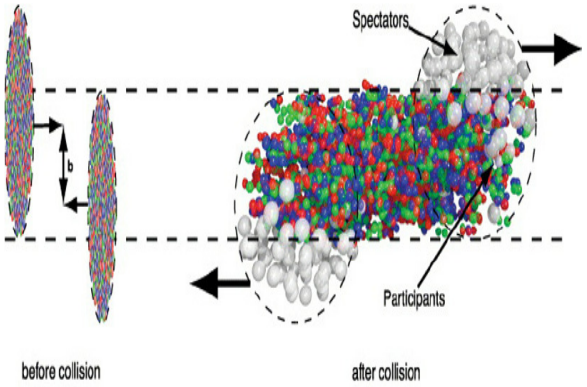

Figure A.1: Heavy ion collision.

Figure A.1 depicts a schematic diagram of heavy-ion collision. Two Lorentz contracted nuclei approach each other in the beam direction. These nucleons are categorised into two categories, viz.- participants and spectators. The participant nucleons undergo collision, whereas spectators move unaffected due to collision geometry, which is determined by length of overlap region called "impact parameter-b" [265, 266]. The least values of impact parameter correspond to more central collisions and deposit highest energy density and temperature [267]. The collision is defined as peripheral collision for high values of impact parameter. Impact parameter can take maximum value equals the sum of two radii of participating nuclei. The colliding nuclei deposit energy density equivalent to a temperature of about 300 MeV, which is sufficient to form QGP. It produces a fireball of extremely hot and dense matter [268]. The fireball of hot and dense matter produced in such collision

evolves with time over the extended region of space – termed as space-time evolution of fireball. A comprehensive understanding of heavy-ion collision dynamics can be achieved through space-time evolution of matter produced at the collision point. The system expansion is governed by the initial stage pressure gradient and collective flow velocity in hadronic phase [269, 44, 270]. The schematic space-time evolution is shown in Figure A.2. The beam axis is along $z-$ direction and collision occurs at point $z = 0$ and $t = 0$. The space-time evolution of fireball occurs in various phases pre-equilibrium phase, expansion phase, hadronisation phase and finally freeze-out phase [271]. In the pre-equilibrium

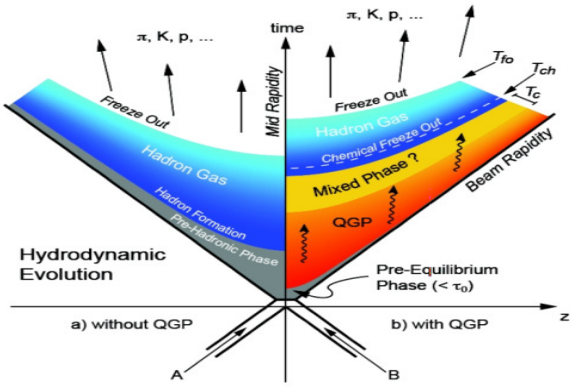

Figure A.2: Spacetime evolution of heavy-ion collision process.

phase, the two colliding nuclei overlap with each other in a finite region of space. The parton-parton hard scattering processes predominate in overlap region and deposit a large amount of energy. This produces a fireball that is not in equilibrium and its dynamics can be studied by perturbative QCD models. The constituents of fireball keep on colliding to establish the local equilibrium of the system – which is known as thermalisation. Comparison of experimental results with hydrodynamic models deduced that thermalisation time is of the order of $0.5 - 1 fm/c$ [272, 273, 274].

The thermal pressure of the system acts against the vacuum, the system starts expanding and the matter cools down. At this point of evolution of fireball, QGP is formed. Here parton-parton and string-string interactions achieve an equilibrium state. On reaching a temperature of 150-200 MeV, the system rapidly expands that decreases its temperature and energy density.

A mixed-phase of QGP and hadronic resonance gas can co-exist if the phase transition is 1st order. This will not happen if the transition is 2nd order or cross-over. In this phase, the quarks and gluons confine into hadrons at a critical temperature of T_c. In the mixed-phase,

fast expansion is prevented and leads to an enhanced lifetime $>$ 10 fm/c [275, 276]. During the transition period, the collective flow does not grow much and eventually, partonic matter converts to a hadronic bound state of the matter until the freeze-out phase. This is called the hadronic phase of evolution. At this point, inelastic collisions cease and hadron abundance does not change, which is referred as chemical freeze-out. However, the hadrons will continue to collide to maintain local thermodynamic equilibrium due to elastic collisions and results in expansion and cooling of the fireball until the mean distance between hadrons exceeds the range of strong interactions. This is referred as kinetic freeze-out where particle decouples from each other. At this point, hadrons pop out as free non-interacting particles [277].

Appendix B

Kinematic Observables in Experiment

Kinematic variables that are used to study the dynamics of heavy-ion collision primarily include transverse momentum spectra (p_{T}), rapidity variable (y), pseudo-rapidity (η) and transverse mass (m_{T}) of the emitted particles [2].

Transverse momenta, as the name suggest, represents the component of momenta in the direction perpendicular to the beam axis. In standard convention, beam direction is considered to be the z-axis and the x-y plane represent transverse plane as shown in Fig. B.1. As per the conservation of p_{T}, the sum of all p_{T} turns to be zero, *i.e.*, the vector sum of the p_{T} of all particles will give net value zero since we had zero transverse momenta in the beam before the collision. The benefit of studying transverse momenta over longitudinal momenta is that we have a huge background of beam particles in the longitudinal direction. Transverse mass m_{T} is given in term of the mass of particle under investigation and transverse momenta as:

$$m_T = \sqrt{m^2 + p_T^2} \tag{B.1}$$

The rapidity (y) can be considered as a relativistic analogue of non-relativistic velocity. The main benefit of using rapidity instead of relativistic velocity is that the rapidity is additive under a longitudinal boost. This means that if a particle's rapidity is y_1 in a particular inertial frame, it simply transforms to $y_1 + y_2$ in a frame that moves with a rapidity y_2. It is expressed in terms of energy and longitudinal component of momentum (p_z) as:

$$y = \frac{1}{2} ln \frac{E + p_z}{E - p_z} \tag{B.2}$$

Pseudorapidity variable (η) is another variant of rapidity that finds its usage in the analysis

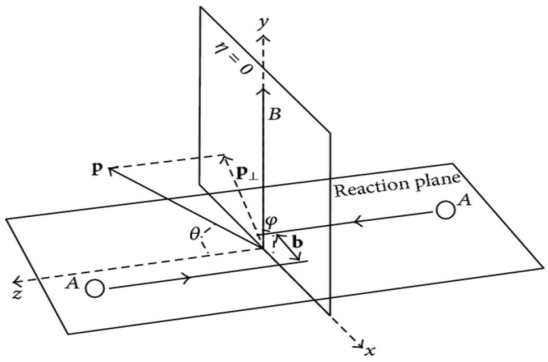

Figure B.1: Geometry of a heavy-ion collision

where we do not have information about mass and momentum etc. of particle and just the emission angle θ is known. Also, in high energy collider experiments, particles are emitted with large momenta as compared to their mass and hence the pseudorapidity is more widely used compared to the rapidity. Another benefit of using η is that its estimation requires only one observable θ whereas y depend on the observables E, p & θ and hence evaluating y involve larger uncertainties compared to the η. We can write $E = \sqrt{m^2 + p^2}$ and $p_z = p\ cos(\theta)$, putting it in the Eq. (B.2) we get:

$$y = \frac{1}{2} ln \frac{\sqrt{m^2 + p^2} + p\ cos(\theta)}{\sqrt{m^2 + p^2} - p\ cos(\theta)} \tag{B.3}$$

And in the high energy limit, where we can consider the approximation $p >> m$, above equation reduces to

$$y = -ln\ (tan(\theta/2)) \equiv \eta \tag{B.4}$$

In term of transverse mass and rapidity variable, we can write particle four-momenta as:

$$p^{\mu} = (E,\ p_x,\ p_y,\ p_z) = (m_T\ cosh(y),\ p_x,\ p_y,\ m_T\ sinh(y)) \tag{B.5}$$

The quantities discussed above has been extensively used in the experiments to characterize the final state particles. The kinematic variables has been used to formulate the indirect signatures that can tell us about the presence of a strongly interacting medium.

Appendix C

Explanation of χ^2 Estimation

The chi-square analysis is a technique to compare the experimental data with a theoretical model and to estimate the value of free parameters in the model. It has long been used to study the goodness of fit and the estimation of the best fit value of the parameters in the theory. The χ^2 is defined as:

$$\chi^2 = \sum_{i=1}^{N} \frac{(x_i - x_{ti})^2}{\sigma_i^2} \tag{C.1}$$

In the equation above, x_i represent the experimental value of i^{th} data point and the corresponding standard deviation is represented by σ_i, total number of data points is given by N and x_{ti} is the theoretical value for the i^{th} point.

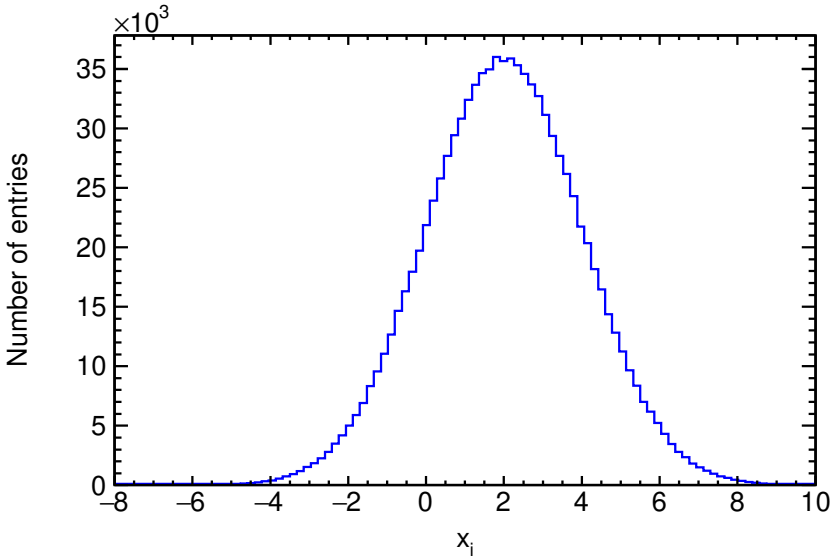

Figure C.1: A toy model representing the distribution of an particular experimental data obtained by repeating the experiment one million times.

If we repeat the experiment n number of times, for any point i we obtain a distribution of experimental value x_i. The distribution will be of Gaussian form with the mean μ_i and the standard deviation σ_i. In Fig. C.1, we have provided a randomly generated Gaussian distribution mimicking i^{th} experimental value x_i for one million trials. The mean value for the above distribution is $\mu_i = 2$ and the standard deviation is $\sigma_i = 2$.

Assuming the theoretical model correctly represent the data, the theoretical prediction x_{ti} will be equal to the mean (μ_i) of the experimental data. So, for a particular trial j $(0 < j \leq n)$, the value of i^{th} $(0 < i \leq N)$ term in the Eq. (C.1) is given as:

$$R_{i,j} = \frac{(x_{i,j} - \mu_i)^2}{\sigma_i^2} \tag{C.2}$$

From the Fig. C.2, we conclude that, statistically, each term in the Eq. (C.1) will contribute

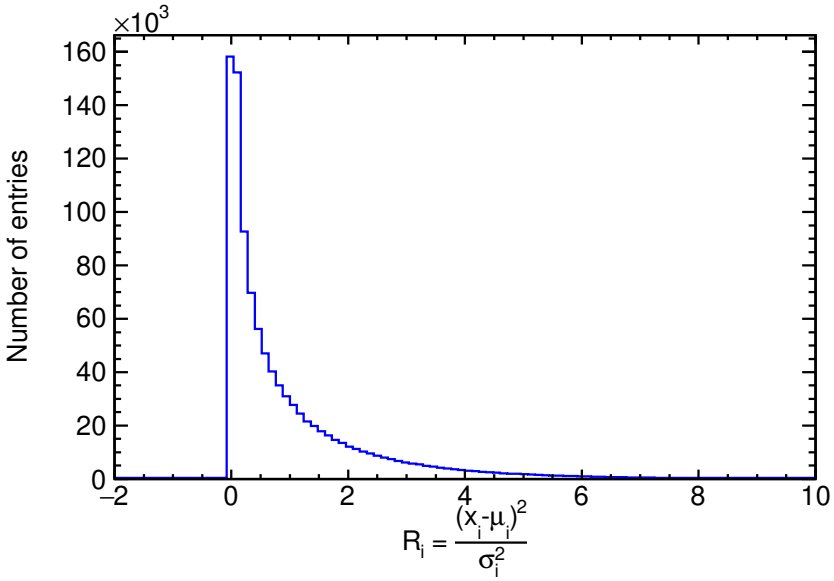

Figure C.2: The distribution of $R_{i,j}$ for one million trials with the corresponding $x_{i,j}$ presented in Fig. C.1.

a value close to unity. So, the probability distribution of χ^2/NDF peaks around unity.

In high energy physics experiments, the data of the distribution of p_{T} and η is also provided in term of $x_i \pm \sigma_i$ however, the x_i in this case does not belong to a random trial j but the mean value of distribution of i_{th} data point taken for large number of events. So, while considering the p_{T}-spectra, the formula for χ^2 will be:

$$\chi^2 = \sum_{i=1}^{N} \frac{(\mu_i - x_{ti})^2}{\sigma_i^2} \tag{C.3}$$

If the theoretical model correctly represents the data, x_{ti} will also be equal to μ_i, hence, each term in the summation will contribute a value close to zero and not unity. So, a model which best describe the data will have the χ^2 value closest to zero.

Bibliography

[1] C. Patrignani et al. Review of Particle Physics. *Chin. Phys. C*, 40(10):100001, 2016.

[2] A. K. Chaudhuri. *A short course on Relativistic Heavy Ion Collisions*. IOPP, 2014.

[3] Szabolcs Borsanyi, Gergely Endrodi, Zoltan Fodor, Antal Jakovac, Sandor D. Katz, Stefan Krieg, Claudia Ratti, and Kalman K. Szabo. The QCD equation of state with dynamical quarks. *JHEP*, 11:077, 2010.

[4] Szabolcs Borsanyi, Gergely Endrodi, Zoltan Fodor, Christian Hoelbling, Sandor Katz, Stefan Krieg, Claudia Ratti, and Kalman K. Szabo. Transition temperature and the equation of state from lattice QCD, Wuppertal-Budapest results. *J. Phys. Conf. Ser.*, 316:012020, 2011.

[5] Georges Aad et al. Measurement of charged-particle spectra in Pb+Pb collisions at $\sqrt{s_{\mathsf{NN}}} = 2.76$ TeV with the ATLAS detector at the LHC. *JHEP*, 09:050, 2015.

[6] Shreyasi Acharya et al. Transverse momentum spectra and nuclear modification factors of charged particles in Xe-Xe collisions at $\sqrt{s_{\mathrm{NN}}}$ = 5.44 TeV. *Phys. Lett.*, B788:166–179, 2019.

[7] G. Agakishiev et al. Strangeness Enhancement in Cu+Cu and Au+Au Collisions at $\sqrt{s_{NN}} = 200$ GeV. *Phys. Rev. Lett.*, 108:072301, 2012.

[8] A. Adare et al. J/ψ Production vs Centrality, Transverse Momentum, and Rapidity in Au+Au Collisions at $\sqrt{s_{NN}} = 200$ GeV. *Phys. Rev. Lett.*, 98:232301, 2007.

[9] L. Adamczyk et al. Bulk Properties of the Medium Produced in Relativistic Heavy-Ion Collisions from the Beam Energy Scan Program. *Phys. Rev.*, C96(4):044904, 2017.

[10] K. Adcox et al. Centrality dependence of pi+ / pi-, K+ / K-, p and anti-p production from s(NN)**(1/2) = 13-=GeV Au+Au collisions at RHIC. *Phys. Rev. Lett.*, 88:242301, 2002.

[11] S. S. Adler et al. Identified charged particle spectra and yields in Au+Au collisions at S(NN)**1/2 = 200-GeV. *Phys. Rev.*, C69:034909, 2004.

[12] Jaroslav Adam et al. Bulk properties of the system formed in $Au + Au$ collisions at $\sqrt{s_{\rm NN}}$ =14.5 GeV at the BNL STAR detector. *Phys. Rev. C*, 101(2):024905, 2020.

[13] B. I. Abelev et al. Energy dependence of pi+-, p and anti-p transverse momentum spectra for Au+Au collisions at s(NN)**(1/2) = 62.4 and 200-GeV. *Phys. Lett.*, B655:104–113, 2007.

[14] B. B. Back et al. Identified hadron transverse momentum spectra in Au+Au collisions at s(NN)**(1/2) = 62.4-GeV. *Phys. Rev.*, C75:024910, 2007.

[15] J. Adams et al. Transverse momentum and collision energy dependence of high p(T) hadron suppression in Au+Au collisions at ultrarelativistic energies. *Phys. Rev. Lett.*, 91:172302, 2003.

[16] Betty Abelev et al. Centrality Dependence of Charged Particle Production at Large Transverse Momentum in Pb–Pb Collisions at $\sqrt{s_{\rm NN}} = 2.76$ TeV. *Phys. Lett.*, B720:52–62, 2013.

[17] S. Acharya et al. Transverse momentum spectra and nuclear modification factors of charged particles in pp, p-Pb and Pb-Pb collisions at the LHC. *JHEP*, 11:013, 2018.

[18] Mikhail Tokarev. Self-similarity of negative particle production from the Beam Energy Scan Program at STAR. *Int. J. Mod. Phys. Conf. Ser.*, 39:1560103, 2015.

[19] Jaroslav Adam et al. Production of light nuclei and anti-nuclei in pp and Pb-Pb collisions at energies available at the CERN Large Hadron Collider. *Phys. Rev.*, C93(2):024917, 2016.

[20] Betty Abelev et al. Centrality dependence of π, K, p production in Pb-Pb collisions at $\sqrt{s_{NN}}$ = 2.76 TeV. *Phys. Rev.*, C88:044910, 2013.

[21] Abdel Nasser Tawfik. Out-Of-Equilibrium Transverse Momentum Spectra of Pions at LHC Energies. *Adv. High Energy Phys.*, 2019:4604608, 2019.

[22] Djamel Ouerdane. Rapidity dependence of charged particle yields for Au+Au at s(NN)**(1/2) = 200-GeV. *Nucl. Phys. A*, 715:478–481, 2003.

[23] Anna Baran, Wojciech Broniowski, and Wojciech Florkowski. Description of the particle ratios and transverse momentum spectra for various centralities at RHIC in a single freezeout model. *Acta Phys. Polon.*, B35:779–798, 2004.

[24] Sadhana Dash and D. P. Mahapatra. p_T spectra in pp and AA collisions at RHIC and LHC energies using the Tsallis-Weibull approach. *Eur. Phys. J.*, A54(4):55, 2018.

[25] Kapil Saraswat, Prashant Shukla, and Venktesh Singh. Transverse momentum spectra of hadrons in high energy pp and heavy ion collisions. *J. Phys. Comm.*, 2(3):035003, 2018.

[26] Serguei Chatrchyan et al. Charged particle transverse momentum spectra in pp collisions at $\sqrt{s} = 0.9$ and 7 TeV. *JHEP*, 08:086, 2011.

[27] Serguei Chatrchyan et al. Study of high-pT charged particle suppression in PbPb compared to pp collisions at $\sqrt{s_{NN}} = 2.76$ TeV. *Eur. Phys. J.*, C72:1945, 2012.

[28] Vardan Khachatryan et al. Charged-particle nuclear modification factors in PbPb and pPb collisions at $\sqrt{s_{\mathrm{N\,N}}} = 5.02$ TeV. *JHEP*, 04:039, 2017.

[29] Shreyasi Acharya et al. Multiplicity dependence of light-flavor hadron production in pp collisions at $\sqrt{s}$ = 7 TeV. *Phys. Rev. C*, 99(2):024906, 2019.

[30] Ehab Abbas et al. Centrality dependence of the pseudorapidity density distribution for charged particles in Pb-Pb collisions at $\sqrt{s_{\mathrm{NN}}}$ = 2.76 TeV. *Phys. Lett. B*, 726:610–622, 2013.

[31] Jaroslav Adam et al. Centrality evolution of the charged-particle pseudorapidity density over a broad pseudorapidity range in Pb-Pb collisions at $\sqrt{s_{\mathrm{NN}}} = 2.76$ TeV. *Phys. Lett. B*, 754:373–385, 2016.

[32] Shreyasi Acharya et al. Centrality and pseudorapidity dependence of the charged-particle multiplicity density in Xe–Xe collisions at $\sqrt{s_{\rm NN}}$ =5.44TeV. *Phys. Lett. B*, 790:35–48, 2019.

[33] S. Acharya et al. Energy dependence and fluctuations of anisotropic flow in Pb-Pb collisions at $\sqrt{s_{\rm NN}} = 5.02$ and 2.76 TeV. *JHEP*, 07:103, 2018.

[34] K Aamodt et al. Elliptic flow of charged particles in Pb-Pb collisions at 2.76 TeV. *Phys. Rev. Lett.*, 105:252302, 2010.

[35] Rickard Lydahl. Elliptic flow studies using event shape engineering in pb-pb collisions at alice. 2017.

[36] M. Gell-Mann. A schematic model of baryons and mesons. *Physics Letters*, 8(3):214–215, 1964.

[37] G. Zweig. An SU(3) model for strong interaction symmetry and its breaking. Version 1. 1 1964.

[38] G. Zweig. *An SU(3) model for strong interaction symmetry and its breaking. Version 2*, pages 22–101. 2 1964.

[39] Martin Breidenbach, Jerome I. Friedman, Henry W. Kendall, Elliott D. Bloom, D. H. Coward, H. C. DeStaebler, J. Drees, Luke W. Mo, and Richard E. Taylor. Observed behavior of highly inelastic electron-proton scattering. *Phys. Rev. Lett.*, 23:935–939, 1969.

[40] Kenneth G. Wilson. Confinement of Quarks. pages 45–59, 2 1974.

[41] Szabolcs Borsanyi, Zoltan Fodor, Christian Hoelbling, Sandor D Katz, Stefan Krieg, Claudia Ratti, and Kalman K. Szabo. Is there still any T_c mystery in lattice QCD? Results with physical masses in the continuum limit III. *JHEP*, 09:073, 2010.

[42] Gergely Endrődi. QCD phase diagram: overview of recent lattice results. *J. Phys. Conf. Ser.*, 503:012009, 2014.

[43] Frithjof Karsch. Lattice results on QCD thermodynamics. *Nucl. Phys. A*, 698:199–208, 2002.

[44] Michael Kliemant, Raghunath Sahoo, Tim Schuster, and Reinhard Stock. *Global Properties of Nucleus-Nucleus Collisions*, volume 785, pages 23–103. 2010.

[45] G. F. Chapline, M. H. Johnson, E. Teller, and M. S. Weiss. Highly excited nuclear matter. *Phys. Rev. D*, 8:4302–4308, 1973.

[46] John C. Collins and M. J. Perry. Superdense Matter: Neutrons Or Asymptotically Free Quarks? *Phys. Rev. Lett.*, 34:1353, 1975.

[47] David J Gross and Frank Wilczek. Ultraviolet behavior of non-abelian gauge theories. *Physical Review Letters*, 30(26):1343, 1973.

[48] H David Politzer. Reliable perturbative results for strong interactions? *Physical Review Letters*, 30(26):1346, 1973.

[49] Larry McLerran. The physics of the quark-gluon plasma. *Reviews of Modern Physics*, 58(4):1021, 1986.

[50] Edward V Shuryak. Quark-gluon plasma and hadronic production of leptons, photons and psions. *Physics Letters B*, 78(1):150–153, 1978.

[51] John Adams et al. Experimental and theoretical challenges in the search for the quark gluon plasma: The STAR Collaboration's critical assessment of the evidence from RHIC collisions. *Nucl. Phys.*, A757:102–183, 2005.

[52] Niels Doble, Lau Gatignon, Kurt Hübner, and Edmund Wilson. The Super Proton Synchrotron (SPS): A Tale of Two Lives. *Adv. Ser. Direct. High Energy Phys.*, 27:135–177, 2017.

[53] M. Harrison, T. Ludlam, and S. Ozaki. RHIC project overview. *Nucl. Instrum. Meth. A*, 499:235–244, 2003.

[54] LHC Machine. *JINST*, 3:S08001, 2008.

[55] Ulrich W. Heinz and Anthony Kuhlman. Anisotropic flow and jet quenching in ultrarelativistic U + U collisions. *Phys. Rev. Lett.*, 94:132301, 2005.

[56] Tetsufumi Hirano, Pasi Huovinen, and Yasushi Nara. Elliptic flow in U+U collisions at $\sqrt{s_{NN}} = 200$ GeV and in Pb+Pb collisions at $\sqrt{s_{NN}} = 2.76$ TeV: Prediction from a hybrid approach. *Phys. Rev. C*, 83:021902, 2011.

[57] Md. Rihan Haque, Zi-Wei Lin, and Bedangadas Mohanty. Multiplicity, average transverse momentum and azimuthal anisotropy in U+U collisions at $\sqrt{s_{NN}}$ = 200 GeV using AMPT model. *Phys. Rev. C*, 85:034905, 2012.

[58] Bjoern Schenke, Prithwish Tribedy, and Raju Venugopalan. Initial-state geometry and fluctuations in Au + Au, Cu + Au, and U + U collisions at energies available at the BNL Relativistic Heavy Ion Collider. *Phys. Rev. C*, 89(6):064908, 2014.

[59] P. N. Bogolubov. On a Model of quasiindependent quarks. *Ann. Inst. H. Poincare Phys. Theor.*, 8:163–190, 1968.

[60] E J Squires. The bag model of hadrons. *Reports on Progress in Physics*, 42(7):1187–1242, jul 1979.

[61] C. Y. Wong. On the schrödinger equation in fluid-dynamical form. *Journal of Mathematical Physics*, 17(6):1008–1010, 1976.

[62] C. Y. Wong. *Introduction to high-energy heavy ion collisions*. 1995.

[63] W. C. Haxton and L. Heller. The Heavy Quark - Anti-quark Potential in the MIT Bag Model. *Phys. Rev. D*, 22:1198, 1980.

[64] P. Hasenfratz, R. R. Horgan, J. Kuti, and J. M. Richard. The Effects of Colored Glue in the QCD Motivated Bag of Heavy Quark - anti-Quark Systems. *Phys. Lett. B*, 95:299–305, 1980.

[65] Eleftherios Papantonopoulos. *From Gravity to Thermal Gauge Theories: The AdS/CFT Correspondence*, volume 828. 2011.

[66] R. Hagedorn and J. Ranft. Statistical thermodynamics of strong interactions at high-energies. 2. Momentum spectra of particles produced in pp-collisions. *Nuovo Cim. Suppl.*, 6:169–354, 1968.

[67] Dirk H Rischke. The quark–gluon plasma in equilibrium. *Progress in Particle and Nuclear Physics*, 52(1):197–296, 2004.

[68] BI Abelev, MM Aggarwal, Z Ahammed, BD Anderson, D Arkhipkin, GS Averichev, Y Bai, J Balewski, O Barannikova, LS Barnby, et al. Systematic measurements of

identified particle spectra in pp, d+ au, and au+ au collisions at the star detector. *Physical Review C*, 79(3):034909, 2009.

[69] BI Abelev, MM Aggarwal, Z Ahammed, AV Alakhverdyants, BD Anderson, D Arkhipkin, GS Averichev, J Balewski, O Barannikova, LS Barnby, et al. Identified particle production, azimuthal anisotropy, and interferometry measurements in au+ au collisions at s nn= 9. 2 gev. *Physical Review C*, 81(2):024911, 2010.

[70] J Adam, L Adamczyk, JR Adams, JK Adkins, G Agakishiev, MM Aggarwal, Z Ahammed, I Alekseev, DM Anderson, R Aoyama, et al. Star collaboration. *Nuclear Physics A*, 982:1063–1066, 2019.

[71] Li-Na Gao, Fu-Hu Liu, and Bao-Chun Li. Rapidity dependent transverse momentum spectra of heavy quarkonia produced in small collision systems at the LHC. *Adv. High Energy Phys.*, 2019:6739315, 2019.

[72] I. Arsene et al. Quark gluon plasma and color glass condensate at RHIC? The Perspective from the BRAHMS experiment. *Nucl. Phys.*, A757:1–27, 2005.

[73] B. B. Back et al. The PHOBOS perspective on discoveries at RHIC. *Nucl. Phys.*, A757:28–101, 2005.

[74] John Adams, MM Aggarwal, Z Ahammed, J Amonett, BD Anderson, D Arkhipkin, GS Averichev, SK Badyal, Y Bai, J Balewski, et al. Experimental and theoretical challenges in the search for the quark–gluon plasma: The star collaboration's critical assessment of the evidence from rhic collisions. *Nuclear Physics A*, 757(1-2):102–183, 2005.

[75] K. Adcox et al. Formation of dense partonic matter in relativistic nucleus-nucleus collisions at RHIC: Experimental evaluation by the PHENIX collaboration. *Nucl. Phys. A*, 757:184–283, 2005.

[76] Georges Aad, B Abbott, J Abdallah, AA Abdelalim, A Abdesselam, O Abdinov, B Abi, M Abolins, H Abramowicz, H Abreu, et al. Observation of a centrality-dependent dijet asymmetry in lead-lead collisions at s nn= 2.76 tev with the atlas detector at the lhc. *Physical review letters*, 105(25):252303, 2010.

[77] K Aamodt, A Abrahantes Quintana, D Adamová, AM Adare, MM Aggarwal, G Aglieri Rinella, AG Agocs, S Aguilar Salazar, Z Ahammed, N Ahmad, et al. Suppression of charged particle production at large transverse momentum in central pb–pb collisions at snn= 2.76 tev. *Physics Letters B*, 696(1-2):30–39, 2011.

[78] Serguei Chatrchyan, V Khachatryan, AM Sirunyan, A Tumasyan, W Adam, T Bergauer, M Dragicevic, J Erö, C Fabjan, M Friedl, et al. Observation and studies of jet quenching in pbpb collisions at s n n= 2.76 tev. *Physical Review C*, 84(2):024906, 2011.

[79] László P Csernai. *Introduction to relativistic heavy ion collisions*. Wiley New York, 1994.

[80] Xin-Nian Wang. Xn wang and m. gyulassy, phys. rev. lett. 68, 1480 (1992). *Phys. Rev. Lett.*, 68:1480, 1992.

[81] M. M. Aggarwal et al. Transverse mass distributions of neutral pions from Pb-208 induced reactions at 158-A-GeV. *Eur. Phys. J.*, C23:225–236, 2002.

[82] S. Voloshin and Y. Zhang. Flow study in relativistic nuclear collisions by Fourier expansion of Azimuthal particle distributions. *Z. Phys.*, C70:665–672, 1996.

[83] R Hagedorn and J Rafelski. From hadron gas to quark matter, instatistical mechanics of quarks and hadrons, edited by h. satz, 1981.

[84] P Koch, Berndt Müller, and Johann Rafelski. Strangeness in relativistic heavy ion collisions. *Physics Reports*, 142(4):167–262, 1986.

[85] P Koch, Johann Rafelski, and W Greiner. Strange hadrons in hot nuclear matter. *Physics Letters B*, 123(3-4):151–154, 1983.

[86] Johann Rafelski. Formation and Observables of the Quark-Gluon Plasma. *Phys. Rept.*, 88:331, 1982.

[87] Johann Rafelski and Berndt Müller. Erratum: Strangeness production in the quark-gluon plasma [phys. rev. lett. 48, 1066 (1982)]. *Physical Review Letters*, 56:2334, 1986.

[88] F Antinori, PA Bacon, A Badala, R Barbera, A Belogianni, A Bhasin, IJ Bloodworth, M Bombara, GE Bruno, SA Bull, et al. Energy dependence of hyperon production in nucleus–nucleus collisions at sps. *Physics Letters B*, 595(1-4):68–74, 2004.

[89] BI Abelev, MM Aggarwal, Z Ahammed, BD Anderson, D Arkhipkin, GS Averichev, Y Bai, J Balewski, O Barannikova, LS Barnby, et al. Enhanced strange baryon production in au+ au collisions compared to p+ p at s nn= 200 gev. *Physical Review C*, 77(4):044908, 2008.

[90] B Abelev, J Adam, D Adamová, AM Adare, MM Aggarwal, G Aglieri Rinella, M Agnello, AG Agocs, A Agostinelli, Z Ahammed, et al. Multi-strange baryon production at mid-rapidity in pb–pb collisions at snn= 2.76 tev. *Physics Letters B*, 728:216–227, 2014.

[91] JH Chen, STAR collaboration, et al. System size and energy dependence of ϕ meson production at rhic. *Journal of Physics G: Nuclear and Particle Physics*, 35(10):104053, 2008.

[92] BI Abelev. Bi abelev et al.(star collaboration), phys. rev. lett. 99, 112301 (2007). *Phys. Rev. Lett.*, 99:112301, 2007.

[93] Salah Hamieh, Krzysztof Redlich, and Ahmed Tounsi. Canonical description of strangeness enhancement from p–a to pb–pb collisions. *Physics Letters B*, 486(1-2):61–66, 2000.

[94] Ahmed Tounsi and Krzysztof Redlich. Canonical constraints on particle production. *Journal of Physics G: Nuclear and Particle Physics*, 28(7):2095, 2002.

[95] A Tounsi, A Mischke, and Krzysztof Redlich. Canonical aspects of strangeness enhancement. *Nuclear Physics A*, 715:565c–568c, 2003.

[96] Rupa Chatterjee, Lusaka Bhattacharya, and Dinesh K. Srivastava. Electromagnetic probes. *Lect. Notes Phys.*, 785:219–264, 2010.

[97] T Matsui and Helmut Satz. J/ψ suppression by quark-gluon plasma formation. *Physics Letters B*, 178(4):416–422, 1986.

[98] MC Abreu, B Alessandro, C Alexa, R Arnaldi, J Astruc, M Atayan, C Baglin, A Baldit, M Bedjidian, F Bellaiche, et al. Observation of a threshold effect in the anomalous j/ψ suppression. *Physics Letters B*, 450(4):456–466, 1999.

[99] Andrew Adare, S Afanasiev, C Aidala, NN Ajitanand, Y Akiba, H Al-Bataineh, J Alexander, K Aoki, Y Aramaki, ET Atomssa, et al. J/ψ suppression at forward rapidity in au+ au collisions at s n n= 200 gev. *Physical Review C*, 84(5):054912, 2011.

[100] Berndt Müller, Jürgen Schukraft, and Bolesław Wysłouch. First results from pb+ pb collisions at the lhc. *Annual Review of Nuclear and Particle Science*, 62:361–386, 2012.

[101] Prashant Shukla et al. Overview of quarkonia and heavy flavour measurements by cms. *arXiv preprint arXiv:1405.3810*, 2014.

[102] M. A. Stephanov. Non-Gaussian fluctuations near the QCD critical point. *Phys. Rev. Lett.*, 102:032301, 2009.

[103] M. M. Aggarwal et al. Higher Moments of Net-proton Multiplicity Distributions at RHIC. *Phys. Rev. Lett.*, 105:022302, 2010.

[104] Sourendu Gupta, Xiaofeng Luo, Bedangadas Mohanty, Hans Georg Ritter, and Nu Xu. Scale for the Phase Diagram of Quantum Chromodynamics. *Science*, 332:1525–1528, 2011.

[105] M. Cheng et al. Baryon Number, Strangeness and Electric Charge Fluctuations in QCD at High Temperature. *Phys. Rev. D*, 79:074505, 2009.

[106] B. Stokic, B. Friman, and K. Redlich. Kurtosis and compressibility near the chiral phase transition. *Phys. Lett. B*, 673:192–196, 2009.

[107] Masayuki Asakawa, Shinji Ejiri, and Masakiyo Kitazawa. Third moments of conserved charges as probes of QCD phase structure. *Phys. Rev. Lett.*, 103:262301, 2009.

[108] S. Jeon and V. Koch. Fluctuations of particle ratios and the abundance of hadronic resonances. *Phys. Rev. Lett.*, 83:5435–5438, 1999.

[109] S. Jeon and V. Koch. Charged particle ratio fluctuation as a signal for QGP. *Phys. Rev. Lett.*, 85:2076–2079, 2000.

[110] Masayuki Asakawa, Ulrich W. Heinz, and Berndt Muller. Fluctuation probes of quark deconfinement. *Phys. Rev. Lett.*, 85:2072–2075, 2000.

[111] R. A. Beth and C. Lasky. The brookhaven alternating gradient synchrotron. *Science*, 128(3336):1393–1401, 1958.

[112] B. B. Back et al. Production of phi mesons in Au+Au collisions at 11.7-A-GeV/c. *Phys. Rev.*, C69:054901, 2004.

[113] B. B. Back et al. Anti-lambda production in Au+Au collisions at 11.7-AGeV/c. *Phys. Rev. Lett.*, 87:242301, 2001.

[114] L. Ahle et al. Proton and deuteron production in Au + Au reactions at 11.6/A-GeV/c. *Phys. Rev.*, C60:064901, 1999.

[115] J. Barrette et al. Proton and pion production in Au + Au collisions at 10.8A-GeV/c. *Phys. Rev.*, C62:024901, 2000.

[116] B. B. Back et al. Baryon rapidity loss in relativistic Au+Au collisions. *Phys. Rev. Lett.*, 86:1970–1973, 2001.

[117] J. L. Klay et al. Charged pion production in 2 to 8 agev central au+au collisions. *Phys. Rev.*, C68:054905, 2003.

[118] L Ahle et al. An Excitation function of $K-$ and $K+$ production in Au $+$ Au reactions at the AGS. *Phys. Lett. B*, 490:53–60, 2000.

[119] J. L. Klay et al. Longitudinal flow from 2-A-GeV to 8-A-GeV Au+Au collisions at the Brookhaven AGS. *Phys. Rev. Lett.*, 88:102301, 2002.

[120] L. Ahle et al. Excitation function of K+ and pi+ production in Au + Au reactions at 2/A-GeV to 10/A-GeV. *Phys. Lett. B*, 476:1–8, 2000.

[121] Roger Lacasse et al. Hadron yields and spectra in Au + Au collisions at the AGS. *Nucl. Phys.*, A610:153C–164C, 1996.

[122] S. V. Afanasiev et al. Energy dependence of pion and kaon production in central Pb + Pb collisions. *Phys. Rev.*, C66:054902, 2002.

[123] T. Alber et al. Charged particle production in proton, deuteron, oxygen and sulphur nucleus collisions at 200-GeV per nucleon. *Eur. Phys. J.*, C2:643–659, 1998.

[124] H. Appelshauser et al. Baryon stopping and charged particle distributions in central Pb + Pb collisions at 158-GeV per nucleon. *Phys. Rev. Lett.*, 82:2471–2475, 1999.

[125] I. G. Bearden et al. Collective expansion in high-energy heavy ion collisions. *Phys. Rev. Lett.*, 78:2080–2083, 1997.

[126] I. G. Bearden et al. Anti-deuteron production in 158-A-GeV/c Pb + Pb collisions. *Phys. Rev. Lett.*, 85:2681–2684, 2000.

[127] I. Bearden et al. Strange meson enhancement in Pb Pb collisions. *Phys. Lett.*, B471:6–12, 1999.

[128] H. Boggild et al. Charged kaon and pion production at mid-rapidity in proton nucleus and sulphur nucleus collisions. *Phys. Rev.*, C59:328–335, 1999.

[129] I. G. Bearden et al. Particle production in central Pb + Pb collisions at 158-A-GeV/c. *Phys. Rev.*, C66:044907, 2002.

[130] C. Alt et al. Energy dependence of phi meson production in central Pb+Pb collisions at s(NN)**(1/2) = 6 to 17 GeV. *Phys. Rev.*, C78:044907, 2008.

[131] C. Alt et al. Energy dependence of Lambda and Xi production in central Pb+Pb collisions at A-20, A-30, A-40, A-80, and A-158 GeV measured at the CERN Super Proton Synchrotron. *Phys. Rev.*, C78:034918, 2008.

[132] C. Alt et al. Energy and centrality dependence of antiproton and proton production in relativistic Pb + Pb collisions at the CERN SPS. 12 2005.

[133] C. Alt et al. Pion and kaon production in central Pb + Pb collisions at 20-A and 30-A-GeV: Evidence for the onset of deconfinement. *Phys. Rev.*, C77:024903, 2008.

[134] Grazyna Odyniec. The RHIC Beam Energy Scan program in STAR and what's next ... *J. Phys. Conf. Ser.*, 455:012037, 2013.

[135] Evan Sangaline. R_{CP} and R_{AA} measurements of identified and unidentified charged particles at high p_T in Au + Au Collisions at $\sqrt{s_{NN}}$ =7.7, 11.5, 19.6, 27, 39,and 62.4 GeV in STAR. *Nucl. Phys.*, A904-905:771c–774c, 2013.

[136] G. Aad et al. Charged-particle multiplicities in pp interactions measured with the ATLAS detector at the LHC. *New J. Phys.*, 13:053033, 2011.

[137] A. Adare et al. Measurement of neutral mesons in p+p collisions at $\sqrt{s}$= 200 GeV and scaling properties of hadron production. *Phys. Rev. D*, 83:052004, 2011.

[138] A. Adare et al. Heavy Quark Production in $p+p$ and Energy Loss and Flow of Heavy Quarks in Au+Au Collisions at $\sqrt{s_{NN}} = 200$ GeV. *Phys. Rev. C*, 84:044905, 2011.

[139] C. Aidala et al. Measurements of $\mu\mu$ pairs from open heavy flavor and Drell-Yan in $p + p$ collisions at $\sqrt{s} = 200$ GeV. *Phys. Rev. D*, 99(7):072003, 2019.

[140] A. Adare et al. Direct-Photon Production in $p + p$ Collisions at $\sqrt{s} = 200$ GeV at Midrapidity. *Phys. Rev. D*, 86:072008, 2012.

[141] Betty Bezverkhny Abelev et al. Production of charged pions, kaons and protons at large transverse momenta in pp and Pb–Pb collisions at $\sqrt{s_{\rm NN}}$ =2.76 TeV. *Phys. Lett. B*, 736:196–207, 2014.

[142] Shreyasi Acharya et al. Production of the $\rho(770)^0$ meson in pp and Pb-Pb collisions at $\sqrt{s_{\rm NN}}$ = 2.76 TeV. *Phys. Rev. C*, 99(6):064901, 2019.

[143] Shreyasi Acharya et al. Production of π^0 and η mesons up to high transverse momentum in pp collisions at 2.76 TeV. *Eur. Phys. J. C*, 77(5):339, 2017.

[144] Jaroslav Adam et al. $K^*(892)^0$ and $\phi(1020)$ meson production at high transverse momentum in pp and Pb-Pb collisions at $\sqrt{s_{\rm NN}}$ = 2.76 TeV. *Phys. Rev. C*, 95(6):064606, 2017.

[145] B. Abelev et al. Inclusive J/ψ production in pp collisions at $\sqrt{s} = 2.76$ TeV. *Phys. Lett. B*, 718:295–306, 2012. [Erratum: Phys.Lett.B 748, 472–473 (2015)].

[146] Shreyasi Acharya et al. Direct photon production at low transverse momentum in proton-proton collisions at $\sqrt{\rm s} = \mathbf{2.76}$ and 8 TeV. *Phys. Rev. C*, 99(2):024912, 2019.

[147] Albert M Sirunyan et al. Measurement of charged pion, kaon, and proton production in proton-proton collisions at $\sqrt{s} = 13$ TeV. *Phys. Rev. D*, 96(11):112003, 2017.

[148] Roel Aaij et al. Measurement of $\psi(2S)$ production cross-sections in proton-proton collisions at $\sqrt{s}$ = 7 and 13 TeV. *Eur. Phys. J. C*, 80(3):185, 2020.

[149] Roel Aaij et al. Measurement of forward J/ψ production cross-sections in pp collisions at $\sqrt{s} = 13$ TeV. *JHEP*, 10:172, 2015. [Erratum: JHEP 05, 063 (2017)].

[150] Roel Aaij et al. Measurements of prompt charm production cross-sections in pp collisions at $\sqrt{s} = 13$ TeV. *JHEP*, 03:159, 2016. [Erratum: JHEP 09, 013 (2016), Erratum: JHEP 05, 074 (2017)].

[151] Shreyasi Acharya et al. Charged-particle production as a function of multiplicity and transverse spherocity in pp collisions at $\sqrt{s} = 5.02$ and 13 TeV. *Eur. Phys. J. C*, 79(10):857, 2019.

[152] Jaroslav Adam et al. Enhanced production of multi-strange hadrons in high-multiplicity proton-proton collisions. *Nature Phys.*, 13:535–539, 2017.

[153] J. W. Cronin, Henry J. Frisch, M. J. Shochet, J. P. Boymond, R. Mermod, P. A. Piroue, and Richard L. Sumner. Production of hadrons with large transverse momentum at 200, 300, and 400 GeV. *Phys. Rev. D*, 11:3105–3123, 1975.

[154] L. A. Linden Levy. What do we really know about cold nuclear matter effects? *Eur. Phys. J. C*, 62:99–102, 2009.

[155] Eliane Epple. Cold nuclear matter effects on jet suppression in heavy-ion collisions. *J. Phys. Conf. Ser.*, 832(1):012006, 2017.

[156] R. Vogt. Cold Nuclear Matter Effects on Open and Hidden Heavy Flavor Production at the LHC. In *7th International Workshop on Charm Physics*, 8 2015.

[157] Grzegorz Wilk and Z Włodarczyk. Interpretation of the nonextensivity parameter q in some applications of tsallis statistics and lévy distributions. *Physical Review Letters*, 84(13):2770, 2000.

[158] John Adams, MM Aggarwal, Z Ahammed, J Amonett, BD Anderson, D Arkhipkin, GS Averichev, SK Badyal, Y Bai, J Balewski, et al. K (892)* resonance production

in au+ au and p+ p collisions at s nn= 200 gev. *Physical Review C*, 71(6):064902, 2005.

[159] Constantino Tsallis. Possible generalization of boltzmann-gibbs statistics. *Journal of statistical physics*, 52(1-2):479–487, 1988.

[160] Constantino Tsallis. Nonadditive entropy and nonextensive statistical mechanics-an overview after 20 years. *Brazilian Journal of Physics*, 39(2A):337–356, 2009.

[161] Grzegorz Wilk and Zbigniew Włodarczyk. Multiplicity fluctuations due to the temperature fluctuations in high-energy nuclear collisions. *Physical Review C*, 79(5):054903, 2009.

[162] O. Ristea, A. Jipa, C. Ristea, T. Esanu, M. Calin, A. Barzu, A. Scurtu, and I. Abu-Quoad. Study of the freeze-out process in heavy ion collisions at relativistic energies. *J. Phys. Conf. Ser.*, 420:012041, 2013.

[163] Zebo Tang, Yichun Xu, Lijuan Ruan, Gene van Buren, Fuqiang Wang, and Zhangbu Xu. Spectra and radial flow at RHIC with Tsallis statistics in a Blast-Wave description. *Phys. Rev.*, C79:051901, 2009.

[164] Ekkard Schnedermann, Josef Sollfrank, and Ulrich W. Heinz. Thermal phenomenology of hadrons from 200-A/GeV S+S collisions. *Phys. Rev.*, C48:2462–2475, 1993.

[165] Constantino Tsallis. Possible Generalization of Boltzmann-Gibbs Statistics. *J. Statist. Phys.*, 52:479–487, 1988.

[166] Tamas S. Biro, Gabor Purcsel, and Karoly Urmossy. Non-Extensive Approach to Quark Matter. *Eur. Phys. J. A*, 40:325–340, 2009.

[167] A. S. Parvan. Comparison of Tsallis statistics with the Tsallis-factorized statistics in the ultrarelativistic pp collisions. *Eur. Phys. J.*, A52(12):355, 2016.

[168] Cheuk-Yin Wong and Grzegorz Wilk. Tsallis fits to p_T spectra and multiple hard scattering in pp collisions at the LHC. *Phys. Rev. D*, 87(11):114007, 2013.

[169] A. S. Parvan. Non-extensive statistics effects in transverse momentum spectra of hadrons. *PoS*, BaldinISHEPPXXII:077, 2015.

[170] Heinz Koppe. Meson yield from bombarding light nuclei with alpha particles. *Zeitschrift für Naturforschung A*, 69(1-2):104–105, 2014.

[171] Heinz Koppe. Koppe's Work of 1948: A fundamental for non-equilibrium rate of particle production. *Z. Naturforschg.*, 3 a:251–252, 1948.

[172] Abdel Nasser Tawfik. Koppe's Work of 1948: A fundamental for non-equilibrium rate of particle production. *Z. Naturforsch. A*, 69:106–107, 2014.

[173] Enrico Fermi. High energy nuclear events. *Progress of Theoretical Physics*, 5(4):570–583, 1950.

[174] R. Hagedorn. Statistical thermodynamics of strong interactions at high-energies. *Nuovo Cim. Suppl.*, 3:147–186, 1965.

[175] F. Karsch, K. Redlich, and A. Tawfik. Thermodynamics at nonzero baryon number density: A Comparison of lattice and hadron resonance gas model calculations. *Phys. Lett. B*, 571:67–74, 2003.

[176] F. Karsch, K. Redlich, and A. Tawfik. Hadron resonance mass spectrum and lattice QCD thermodynamics. *Eur. Phys. J. C*, 29:549–556, 2003.

[177] Leo Stodolsky. Temperature fluctuations in multiparticle production. *Phys. Rev. Lett.*, 75:1044–1045, 1995.

[178] Enrico Fermi. Angular Distribution of the Pions Produced in High Energy Nuclear Collisions. *Phys. Rev.*, 81:683–687, 1951.

[179] Abdel Nasser Tawfik. Equilibrium statistical-thermal models in high-energy physics. *Int. J. Mod. Phys. A*, 29(17):1430021, 2014.

[180] Szymon Pulawski. Recent results from the strong interactions program of NA61/SHINE. *EPJ Web Conf.*, 164:07033, 2017.

[181] Sumit Basu, Rupa Chatterjee, Bastanta K. Nandi, and Tapan K. Nayak. Characterization of relativistic heavy-ion collisions at the Large Hadron Collider through temperature fluctuations. 2015.

[182] Ulrich Heinz and Raimond Snellings. Collective flow and viscosity in relativistic heavy-ion collisions. *Ann. Rev. Nucl. Part. Sci.*, 63:123–151, 2013.

[183] Nasser Demir and Steffen A. Bass. Shear-Viscosity to Entropy-Density Ratio of a Relativistic Hadron Gas. *Phys. Rev. Lett.*, 102:172302, 2009.

[184] Muhammad Waqas and Bao-Chun Li. Kinetic freeze-out temperature and transverse flow velocity in Au-Au collisions at RHIC-BES energies. 2019.

[185] S. A. Bass et al. Microscopic models for ultrarelativistic heavy ion collisions. *Prog. Part. Nucl. Phys.*, 41:255–369, 1998.

[186] Jajati K. Nayak and Jan-e Alam. Measuring radial flow of partonic and hadronic phases in relativistic heavy ion collision. *Phys. Rev.*, C80:064906, 2009.

[187] G. Wilk and Z. Wlodarczyk. On the interpretation of nonextensive parameter q in Tsallis statistics and Levy distributions. *Phys. Rev. Lett.*, 84:2770, 2000.

[188] Grzegorz Wilk and Zbigniew Wlodarczyk. Consequences of temperature fluctuations in observables measured in high energy collisions. *Eur. Phys. J.*, A48:161, 2012.

[189] Constantino Tsallis. *Introduction to Nonextensive Statistical Mechanics*. Springer, 10 January 2009.

[190] Murray Gell-Mann and Constantino Tsallis. *Nonextensive Entropy-Interdisciplinary Application*. Oxford University Press, 10 January 2004.

[191] J. Cleymans and D. Worku. Relativistic Thermodynamics: Transverse Momentum Distributions in High-Energy Physics. *Eur. Phys. J.*, A48:160, 2012.

[192] Arvind Khuntia, Sushanta Tripathy, Raghunath Sahoo, and Jean Cleymans. Multiplicity Dependence of Non-extensive Parameters for Strange and Multi-Strange Particles in Proton-Proton Collisions at $\sqrt{s} = 7$ TeV at the LHC. *Eur. Phys. J.*, A53(5):103, 2017.

[193] Oana Ristea, Alexandru Jipa, Catalin Ristea, Calin Besliu, Ionel Lazanu, Marius Calin, Tiberiu Esanu, and Vanea Covlea. Study of the particle transverse momentum

spectra in relativistic heavy ion collisions using the Tsallis statistics. *EPJ Web Conf.*, 66:04025, 2014.

[194] J. Cleymans and D. Worku. The Tsallis Distribution in Proton-Proton Collisions at $\sqrt{s}$ = 0.9 TeV at the LHC. *J. Phys.*, G39:025006, 2012.

[195] G. Wilk and Z. Wlodarczyk. Application of nonextensive statistics to particle and nuclear physics. *Physica*, A305:227–233, 2002.

[196] G. Wilk and Z. Wlodarczyk. The Imprints of nonextensive statistical mechanics in high-energy collisions. *Chaos Solitons Fractals*, 13:581–594, 2002.

[197] Grzegorz Wilk and Zbigniew Wlodarczyk. Power laws in elementary and heavy-ion collisions: A Story of fluctuations and nonextensivity? *Eur. Phys. J. A*, 40:299–312, 2009.

[198] T.S. Biro and G. Purcsel. Non-extensive Boltzmann equation and hadronization. *Phys. Rev. Lett.*, 95:162302, 2005.

[199] Rui-Fang Si, Hui-Ling Li, and Fu-Hu Liu. Comparing standard distribution and its Tsallis form of transverse momenta in high energy collisions. *Adv. High Energy Phys.*, 2018:7895967, 2018.

[200] M. Kataja and P. V. Ruuskanen. Nonzero Chemical Potential and the Shape of the p_T Distribution of Hadrons in Heavy Ion Collisions. *Phys. Lett.*, B243:181–184, 1990.

[201] Wojciech Broniowski and Wojciech Florkowski. Explanation of the RHIC p(T) spectra in a thermal model with expansion. *Phys. Rev. Lett.*, 87:272302, 2001.

[202] Wojciech Broniowski and Wojciech Florkowski. Strange particle production at RHIC in a single freezeout model. *Phys. Rev.*, C65:064905, 2002.

[203] Wojciech Broniowski and Wojciech Florkowski. Thermal model at RHIC: particle ratios and transverse momentum spectra. In *Ultrarelativistic heavy-ion collisions. Proceedings, 30th International Workshop on Gross Properties of Nuclei and Nuclear Excitations, Hirschegg, Austria, January 13-19, 2002*, pages 146–151, 2002.

[204] Wilbur K Brown and Kenneth H Wohletz. Derivation of the weibull distribution based on physical principles and its connection to the rosin–rammler and lognormal distributions. *Journal of Applied Physics*, 78(4):2758–2763, 1995.

[205] Wilbur K Brown. A theory of sequential fragmentation and its astronomical applications. *Journal of Astrophysics and Astronomy*, 10(4):89–112, 1989.

[206] A. A. Bylinkin and A. A. Rostovtsev. Parametrization of the shape of hadron-production spectra in high-energy particle interactions. *Phys. Atom. Nucl.*, 75:999–1005, 2012. [Yad. Fiz.75,1060(2012)].

[207] Alexander Bylinkin, Nadezda S. Chernyavskaya, and Andrei A. Rostovtsev. Predictions on the transverse momentum spectra for charged particle production at LHC-energies from a two component model. *Eur. Phys. J.*, C75(4):166, 2015.

[208] G. Arnison et al. Transverse Momentum Spectra for Charged Particles at the CERN Proton anti-Proton Collider. *Phys. Lett. B*, 118:167–172, 1982.

[209] Cheuk-Yin Wong and Grzegorz Wilk. Tsallis Fits to p_t Spectra for pp Collisions at LHC. *Acta Phys. Polon. B*, 43:2047–2054, 2012.

[210] Minoru Biyajima, Takuya Mizoguchi, and Naomichi Suzuki. Analyses of whole transverse momentum distributions in $p\bar{p}$ and pp collisions by using a modified version of Hagedorn's formula. *Int. J. Mod. Phys. A*, 32(11):1750057, 2017.

[211] Christopher Michael and L. Vanryckeghem. Consequences of Momentum Conservation for Particle Production at Large Transverse Momentum. *J. Phys. G*, 3:L151, 1977.

[212] Christopher Michael. Large Transverse Momentum and Large Mass Production in Hadronic Interactions. *Prog. Part. Nucl. Phys.*, 2:1, 1979.

[213] Karl Pearson. X. contributions to the mathematical theory of evolution.—ii. skew variation in homogeneous material. *Philosophical Transactions of the Royal Society of London A: Mathematical, Physical and Engineering Sciences*, 186:343–414, 1895.

[214] J. H. Pollard. *A Handbook of Numerical and Statistical Techniques: With Examples Mainly from the Life Sciences*. Cambridge University Press, 1977.

[215] O. Podladchikova, B. Lefebvre, V. Krasnoselskikh, and V. Podladchikov. Classification of probability densities on the basis of Pearson's curves with application to coronal heating simulations. *Nonlinear Processes in Geophysics, European Geosciences Union (EGU)*, 10(4/5):323–333, 2003.

[216] W P Elderton. Frequency curves and correlation. *J. Inst. Actuar.*, pages 1–172, 1907.

[217] Lahcene Bachioua. On pearson families of distributions and its applications. *African Journal of Mathematics and Computer Science Research*, 6:108–117, 01 2013.

[218] Rene Brun and Fons Rademakers. Root — an object oriented data analysis framework. *Nuclear Instruments and Methods in Physics Research Section A: Accelerators, Spectrometers, Detectors and Associated Equipment*, 389(1):81–86, 1997. New Computing Techniques in Physics Research V.

[219] F. James and M. Roos. Minuit: A System for Function Minimization and Analysis of the Parameter Errors and Correlations. *Comput. Phys. Commun.*, 10:343–367, 1975.

[220] Rohit Gupta and Satyajit Jena. Model comparison of the transverse momentum spectra of charged hadrons produced in $PbPb$ collision at $\sqrt{s_{NN}} = 5.02$ TeV. *Adv. High Energy Phys.*, 2022:5482034, 2022.

[221] M. D. Azmi and J. Cleymans. The Tsallis Distribution at Large Transverse Momenta. *Eur. Phys. J. C*, 75(9):430, 2015.

[222] Rohit Gupta, Shubhangi Jain, and Satyajit Jena. A unified statistical approach to explain the transverse momentum spectra in hadron-hadron collision. 3 2021.

[223] G. Wilk and Z. Włodarczyk. Tsallis distribution with complex nonextensivity parameter q. *Physica*, A413:53–58, 2014.

[224] Grzegorz Wilk and Zbigniew Wlodarczyk. Log-periodic oscillations of transverse momentum distributions. 2014.

[225] Jaroslav Adam et al. Centrality dependence of the pseudorapidity density distribution for charged particles in Pb-Pb collisions at $\sqrt{s_{\rm NN}} = 5.02$ TeV. *Phys. Lett. B*, 772:567–577, 2017.

[226] Jian-Xin Sun, Cai-Xing Tian, Er-Qin Wang, and Fu-Hu Liu. Dependence of charged particle pseudorapidity distributions on centrality in Pb-Pb collisions at $\sqrt{s_{NN}}$ = 2.76-TeV. *Chin. Phys. Lett.*, 30:022501, 2013.

[227] G. Wolschin. Pseudorapidity distributions of produced charged hadrons in pp collisions at RHIC and LHC energies. *EPL*, 95(6):61001, 2011.

[228] Li-Na Gao and Fu-Hu Liu. On Pseudorapidity Distribution and Speed of Sound in High Energy Heavy Ion Collisions Based on a New Revised Landau Hydrodynamic Model. *Adv. High Energy Phys.*, 2015:184713, 2015.

[229] Bao-Chun Li, Ya-Zhou Wang, Fu-Hu Liu, Xin-Jian Wen, and You-Er Dong. Particle production in relativistic $pp(\overline{p})$ and AA collisions at RHIC and LHC energies with Tsallis statistics using the two-cylindrical multisource thermal model. *Phys. Rev. D*, 89(5):054014, 2014.

[230] J. Cleymans. Rapidity and energy dependence of thermal parameters. *J. Phys. G*, 35:044017, 2008.

[231] F. Becattini and J. Cleymans. Chemical Equilibrium in Heavy Ion Collisions: Rapidity Dependence. *J. Phys. G*, 34:S959–964, 2007.

[232] L. Marques, J. Cleymans, and A. Deppman. Description of High-Energy pp Collisions Using Tsallis Thermodynamics: Transverse Momentum and Rapidity Distributions. *Phys. Rev. D*, 91:054025, 2015.

[233] Y. Gao, H. Zheng, L. L. Zhu, and A. Bonasera. Description of Charged Particle Pseudorapidity Distributions in Pb+Pb Collisions with Tsallis Thermodynamics. *Eur. Phys. J. A*, 53(10):197, 2017.

[234] J. Q. Tao, M. Wang, H. Zheng, W. C. Zhang, L. L. Zhu, and A. Bonasera. Pseudorapidity distributions of charged particles in pp($\overline{\rm p}$), p(d)A and AA collisions using Tsallis thermodynamics. 11 2020.

[235] Rohit Gupta, Aman Singh Katariya, and Satyajit Jena. A unified formalism to study the pseudorapidity spectra in heavy-ion collision. *Eur. Phys. J. A*, 57(7):224, 2021.

[236] Dushmanta Sahu, Sushanta Tripathy, Raghunath Sahoo, and Archita Rani Dash. Multiplicity dependence of shear viscosity, isothermal compressibility and speed of sound in pp collisions at $\sqrt{s}$ = 7 TeV. *Eur. Phys. J. A*, 56(7):187, 2020.

[237] Sumit Basu, Sandeep Chatterjee, Rupa Chatterjee, Tapan K. Nayak, and Basanta K. Nandi. Specific Heat of Matter Formed in Relativistic Nuclear Collisions. *Phys. Rev. C*, 94(4):044901, 2016.

[238] Arvind Khuntia, Pragati Sahoo, Prakhar Garg, Raghunath Sahoo, and Jean Cleymans. Speed of sound in hadronic matter using non-extensive Tsallis statistics. *Eur. Phys. J. A*, 52(9):292, 2016.

[239] Shubhangi Jain, Rohit Gupta, and Satyajit Jena. Study of isothermal compressibility and speed of sound in matter formed in heavy-ion collision using unified formalism. 3 2021.

[240] Shreyasi Acharya et al. Multiplicity dependence of light (anti-)nuclei production in p-Pb collisions at $\sqrt{s_{\rm NN}}$ = 5.02 TeV. *Phys. Lett. B*, 800:135043, 2020.

[241] Dushmanta Sahu, Sushanta Tripathy, Raghunath Sahoo, and Swatantra Kumar Tiwari. Formation of a Perfect Fluid in pp, p-Pb, Xe-Xe and Pb-Pb Collisions at the Large Hadron Collider Energies. 1 2020.

[242] P. Kovtun, Dan T. Son, and Andrei O. Starinets. Viscosity in strongly interacting quantum field theories from black hole physics. *Phys. Rev. Lett.*, 94:111601, 2005.

[243] K. Aamodt et al. Higher harmonic anisotropic flow measurements of charged particles in Pb-Pb collisions at $\sqrt{s_{NN}}$=2.76 TeV. *Phys. Rev. Lett.*, 107:032301, 2011.

[244] Matthew Luzum and Paul Romatschke. Conformal Relativistic Viscous Hydrodynamics: Applications to RHIC results at s(NN)**(1/2) = 200-GeV. *Phys. Rev.*, C78:034915, 2008. [Erratum: Phys. Rev.C79,039903(2009)].

[245] Stanislaw Mrowczynski. Hadronic matter compressibility from event by event analysis of heavy ion collisions. *Phys. Lett. B*, 430:9–14, 1998.

[246] Shreyasi Acharya et al. Production of charged pions, kaons, and (anti-)protons in Pb-Pb and inelastic pp collisions at $\sqrt{s_{NN}}$ = 5.02 TeV. *Phys. Rev. C*, 101(4):044907, 2020.

[247] Peter Braun-Munzinger, Alexander Kalweit, Krzysztof Redlich, and Johanna Stachel. Confronting fluctuations of conserved charges in central nuclear collisions at the LHC with predictions from Lattice QCD. *Phys. Lett. B*, 747:292–298, 2015.

[248] Betty Bezverkhny Abelev et al. Freeze-out radii extracted from three-pion cumulants in pp, p–Pb and Pb–Pb collisions at the LHC. *Phys. Lett. B*, 739:139–151, 2014.

[249] Abdel Nasser Tawfik, Hayam Yassin, and Eman R. Abo Elyazeed. Extensive/nonextensive statistics for p_T distributions of various charged particles produced in p+p and A+A collisions in a wide range of energies. 5 2019.

[250] Fernando G. Gardim, Giuliano Giacalone, Matthew Luzum, and Jean-Yves Ollitrault. Effects of initial state fluctuations on the mean transverse momentum. *Nucl. Phys. A*, 1005:121999, 2021.

[251] Sandeep Chatterjee, Sabita Das, Lokesh Kumar, D. Mishra, Bedangadas Mohanty, Raghunath Sahoo, and Natasha Sharma. Freeze-Out Parameters in Heavy-Ion Collisions at AGS, SPS, RHIC, and LHC Energies. *Adv. High Energy Phys.*, 2015:349013, 2015.

[252] P. Braun-Munzinger, J. Stachel, and Christof Wetterich. Chemical freezeout and the QCD phase transition temperature. *Phys. Lett. B*, 596:61–69, 2004.

[253] J. D. Bjorken. Highly Relativistic Nucleus-Nucleus Collisions: The Central Rapidity Region. *Phys. Rev. D*, 27:140–151, 1983.

[254] T. J. Hallman, D. E. Kharzeev, J. T. Mitchell, and T. S. Ullrich, editors. *Quark matter 2001. Proceedings, 15th International Conference on Ultrarelativistic nucleus nucleus collisions, QM 2001, Stony Brook, USA, January 15-20, 2001*, volume 698, 2002.

[255] Suman Deb, Golam Sarwar, Raghunath Sahoo, and Jan-e Alam. Study of QCD dynamics using small systems. 9 2019.

[256] Arthur M. Poskanzer and S. A. Voloshin. Methods for analyzing anisotropic flow in relativistic nuclear collisions. *Phys. Rev.*, C58:1671–1678, 1998.

[257] Raimond Snellings. Elliptic Flow: A Brief Review. *New J. Phys.*, 13:055008, 2011.

[258] A. Adare et al. Measurements of Higher-Order Flow Harmonics in Au+Au Collisions at $\sqrt{s_{NN}} = 200$ GeV. *Phys. Rev. Lett.*, 107:252301, 2011.

[259] B. Abelev et al. D meson elliptic flow in non-central Pb-Pb collisions at $\sqrt{s_{\rm NN}}$ = 2.76TeV. *Phys. Rev. Lett.*, 111:102301, 2013.

[260] Ehab Abbas et al. J/Psi Elliptic Flow in Pb-Pb Collisions at $\sqrt{s_{\rm NN}}$ = 2.76 TeV. *Phys. Rev. Lett.*, 111:162301, 2013.

[261] Betty Abelev et al. Directed Flow of Charged Particles at Midrapidity Relative to the Spectator Plane in Pb-Pb Collisions at $\sqrt{s_{NN}}$=2.76 TeV. *Phys. Rev. Lett.*, 111(23):232302, 2013.

[262] Matthew Luzum and Jean-Yves Ollitrault. Directed flow at midrapidity in heavy-ion collisions. *Phys. Rev. Lett.*, 106:102301, 2011.

[263] Shreyasi Acharya et al. Measurement of deuteron spectra and elliptic flow in Pb–Pb collisions at $\sqrt{s_{\rm NN}}$ = 2.76 TeV at the LHC. *Eur. Phys. J.*, C77(10):658, 2017.

[264] K. H. Ackermann et al. Elliptic flow in Au + Au collisions at (S(NN))**(1/2) = 130 GeV. *Phys. Rev. Lett.*, 86:402–407, 2001.

[265] A. Bialas, M. Bleszynski, and W. Czyz. Multiplicity Distributions in Nucleus-Nucleus Collisions at High-Energies. *Nucl. Phys. B*, 111:461–476, 1976.

[266] C Oppedisano, Alice Collaboration, et al. p–pb collisions: Particle production and centrality determination in alice. *Nuclear Physics A*, 932:399–403, 2014.

[267] Betty Abelev, J Adam, D Adamová, AM Adare, MM Aggarwal, G Aglieri Rinella, M Agnello, AG Agocs, A Agostinelli, Z Ahammed, et al. Centrality determination of pb-pb collisions at s n n= 2.76 tev with alice. *Physical Review C*, 88(4):044909, 2013.

[268] Stanislaw Mrowczynski. Quark-gluon plasma. *arXiv preprint nucl-th/9905005*, 1999.

[269] Asis Kumar Chaudhuri. *A short course on relativistic heavy ion collisions*. IOP Publishing, 2014.

[270] Jean Letessier and Johann Rafelski. *Hadrons and quark–gluon plasma*, volume 18. Cambridge University Press, 2002.

[271] Michael Patrick McCumber. *Measurement of fast parton interactions with hot dense nuclear matter via two-particle correlations at PHENIX*. PhD thesis, SUNY, Stony Brook, 2009.

[272] Pasi Huovinen, Peter F Kolb, Ulrich Heinz, PV Ruuskanen, and Sergei A Voloshin. Radial and elliptic flow at rhic: Further predictions. *Physics Letters B*, 503(1-2):58–64, 2001.

[273] Tetsufumi Hirano and Keiichi Tsuda. Collective flow and two-pion correlations from a relativistic hydrodynamic model with early chemical freeze-out. *Physical Review C*, 66(5):054905, 2002.

[274] Peter F Kolb and Ulrich Heinz. Hydrodynamic description of ultrarelativistic heavy-ion collisions. In *Quark–Gluon Plasma 3*, pages 634–714. World Scientific, 2004.

[275] Ulrich W Heinz. Concepts of heavy-ion physics. *arXiv preprint hep-ph/0407360*, 2004.

[276] Ulrich Heinz, Kang S Lee, and Ekkard Schnedermann. Hadronization of a quark-gluon plasma. In *Quark-Gluon Plasma*, pages 471–517. World Scientific, 1990.

[277] Rainer J Fries, B Müller, C Nonaka, and SA Bass. Hadron production in heavy ion collisions: Fragmentation and recombination from a dense parton phase. *Physical Review C*, 68(4):044902, 2003.